Simulation of the SP-STM induced magnetization switching of nanowires and nanoislands

Dissertation
zur Erlangung des Doktorgrades
des Fachbereichs Physik
der Universität Hamburg

vorgelegt von
Thim Stapelfeldt
aus
Bad Oldesloe

Hamburg
2014

Gutachter der Dissertation:
Prof. Dr. R. Wiesendanger
Prof. Dr. M. Potthoff

Gutachter der Disputation:
Prof. Dr. R. Wiesendanger
Prof. Dr. H. P. Oepen

Datum der Disputation:
21.03.2014

Vorsitzender des Prüfungsausschusses:
Prof. Dr. M. Thorwart

Vorsitzender des Promotionsausschusses:
Prof. Dr. D. Pfannkuche

Dekan der MIN-Fakultät:
Prof. Dr. H. Graener

Abstract

Kryder's law predicts a doubling of the capacity of commodity hard drive devices every 13 months. However, the capacity did not increase as expected in the past three years. Perhaps today's hard drive technology does reach its limits?

The present work shall support the development of future storage devices with increased storage capacity. In order to do so the magnetization switching of ferromagnetic particles of only a few nanometer in size has been investigated in the framework of Monte Carlo simulations. A focus of the present work lies on the question if a narrow domain wall could be moved through a hard magnetic nanowire by means of a spin-polarized tunneling current. By controlling the position of the domain wall one can precisely control the magnetization of the particle. In the simulations the current is induced into the nanowire by the magnetic tip of a scanning tunneling microscope (STM). The tunneling electrons of the polarized current exert a torque on the magnetization of the atoms underneath the tip, which can lead to a displacement of the domain wall. Additional simulations focus on the superparamagnetic properties of nanoparticles. The influence of the temperature on the magnetization switching of particles with ever decreasing size is investigated. In particular the impact of the shape of the islands on the magnetization switching is addressed.

A classical Monte Carlo simulation is used, which is based on a single spin update Metropolis algorithm. The studied nanoparticles are arranged in a monolayer with open boundary conditions and consist of 50-1600 atoms. The magnetic moments, thus, the spins of the atoms are described by the Heisenberg model. The atoms interact with each other via the exchange interaction up to third nearest neighbors and exhibit a strong uni-axial magnetic anisotropy lying in-plane.

The simulations reveal that it possible to address and move a single domain wall in a nanowire by means of a spin-polarized tunneling current. Furthermore, it is shown, that magnetic defects present in the wire impede or even prevent a propagation of the domain wall. The defects are described as atoms with altered magnetic properties, which can lead to a pinning of the domain wall. Temperature dependent simulations of the spin-spin correlation function of the atoms allowed to study the particle's superparamagnetic properties. From the analysis of the correlation function the critical temperatures have been defined; hence, the temperatures at which the particle changes it's magnetic properties. A study of the magnetization dynamics of Fe/W(110) nanoislands of different size and shape at different temperatures in the superparamagnetic regime confirmed experimental results, which found the magnetization dynamics to be strongly dependent on the shape of the islands. This shape dependency is a result of an anisotropic exchange interaction and the underlying switching mechanism.

The simulations presented permit a deeper insight into the switching process of ferromagnetic nanoparticles. The results obtained are helpful for the development of future magnetic storage devices and also for the development of tailored nanostructures, which hinder or favor magnetization reversal.

Zusammenfassung

Das "Kryder Gesetz" sagt eine Verdopplung der Speicherkapazität von konventionellen Festplatten alle 13 Monate voraus. In den letzten drei Jahren hat die Speicherkapazität jedoch nicht wie erwartet zugenommen. Vielleicht stößt die gängige Festplattentechnik inzwischen an ihre Grenzen?

Die vorliegende Arbeit soll dazu beitragen, den Anstieg der Speicherkapazität in Zukunft wieder zu erhöhen. Um das zu erreichen, werden mit Hilfe von Monte Carlo Simulationen das Schaltverhalten von ferromagnetischen Teilchen einer Größe von nur wenigen Nanometern untersucht. Insbesondere befasst sich die Arbeit mit der Frage, ob sich eine schmale Domänenwand mit Hilfe eines polarisierten Tunnelstroms durch einen hart-magnetischen Nanodraht bewegen lässt. Der Tunnelstrom wird dabei durch die magnetische Spitze eines Rastertunnelmikroskops (RTM) in den Nanodraht induziert. Die Tunnel-Elektronen des polarisierten Stromes üben ein Drehmoment auf die Magnetisierung der Atome direkt unterhalb der RTM-Spitze aus und führen dadurch zu einer Verschiebung der Domänenwand. Darüber hinaus werden die superparamagnetischen Eigenschaften, also der Einfluss der Temperatur auf das Schalten von immer kleiner werdenden hart-magnetischen Nanoteilchen ermittelt. Insbesondere wird untersucht, wie die Geometrie der Teilchen das Schalten beeinflusst.

Es wird eine klassische Monte Carlo Simulation verwendet, die auf einem Einzel-Spin-Update Metropolis Algorithmus basiert. Die untersuchten Nanoteilchen sind in einer Monolage mit offenen Randbedingungen angeordnet und bestehen aus 50-1600 Atomen. Die magnetischen Momente der Atome werden durch das Heisenberg Modell beschrieben. Die Atome treten miteinander über einen ferromagnetischen Austausch bis zum drittnächsten Nachbarn in Wechselwirkung und besitzen eine starke magnetische Anisotropie, die zu einer Magnetisierungsausrichtung entlang einer Achse in der Ebene führt.

Die Simulationen zeigen, dass es möglich ist, eine einzelne Domänenwand in einem Nanodraht mit Hilfe eines lokal eingespeisten Stromes gezielt zu verschieben. Es wird aber auch gezeigt, dass magnetische Defekte, beschrieben durch Gitterpunkte mit veränderten magnetischen Eigenschaften, eine erfolgreiche Manipulation der Domänenwand durch Pinning an den Defekten erschweren oder sogar verhindern können. Temperaturabhängige Simulationen ergeben, dass man durch die Auswertung der Korrelationen zwischen den magnetischen Momenten der Atome die superparamagnetischen Eigenschaften der Teilchen genau definieren kann. Aus den Simulationen lassen sich die kritischen Temperaturen bestimmen, bei denen sich die magnetischen Eigenschaften des Teilchens verändern. Eine Untersuchung der Magnetisierungsdynamik von Fe/W(110) Nanoinseln weist, wie bereits experimentell vorhergesagt, eine deutliche Abhängigkeit von der Geometrie der Inseln auf. Der Grund hierfür liegt in dem anisotropen Austausch sowie in dem Mechanismus der Magnetisierungsumkehr.

Die vorgestellten Simulationen geben einen tieferen Einblick in die Schaltprozesse von ferromagnetischen Nanoteilchen. Die daraus gewonnenen Erkennt-

nisse sind hilfreich für die Entwicklung von zukünftigen magnetischen Speichermedien oder für die Entwicklung maßgeschneiderter Nanostrukturen, in denen eine Magnetisierungsumkehr gezielt erschwert oder erleichtert werden soll.

Contents

1 Introduction

The present thesis investigates in the framework of a Monte Carlo simulation the theoretical proposal to manipulate an individual domain wall in a hard-magnetic nanowire by means of a tunneling current. A scanning tunneling microscope (STM) thereby serves as instrument to induce a spin-polarized tunneling current. Beyond that, the superparamagnetic properties of a hard-magnetic nanoisland consisting of 50-400 atoms are investigated. This study of the size, shape, and temperature dependent properties follows the road of minimizing the size of magnetic bits in future storage devices and to design new logic devices on the nanoscale.

The so-called *Kryder's law* [1] describes the increase of the areal storage density of a commodity hard drive device (HDD) and finds the annual increase of the capacity lying at 40% in the last three decades. It predicts the maximum capacity for a 3.5-inch hard drive reaching 12 TB by the year of 2014 [2]. There is not much time left and still some way to go to reach that goal, as today's commodity HDD have a maximum capacity of 4 TB. In 2010 the authors of [2] reconsidered the prediction given by the Kryder's law on the basis of the 2009 and 2010 reported areal density products and say that "a reasonable projection is maintaining a 20% annual areal density increase". The goal of an annual density growth of 20% is accomplished if a capacity of a 3.5-inch HDD of 6 TB is reached by the year of 2014, which seems to be a more realistic goal. Concern about the slowing down of the annual capacity increase becomes also evident in an online article published in September 2013 by Tom Coughlin [3], a storage analyst and consultant. He writes that "It has been more than two years since there was an increase in the areal density of HDDs.", but he foresees an increase of enterprise 3.5-inch HDDs up to 6-8 TB within the next year. Just like Coughlin and the authors of [2] expected, in November 2013 the first 6 TB HDD has been released, when the hard drive company HGST [4] presented its first "hermetically sealed, helium hard drive". The hard drive named Ultrastar® He6 aims at operation for cloud and research leaders including HP, Netflix and CERN. But what seems to make the technique using liquid helium interesting is not the increased capacity, but rather the reduced customer total cost-of-ownership, as the disk has a much smaller energy consumption compared to commodity hard drives. Even though the Ultrastar® He6 is still an enterprise product, it makes hope that also commodity HDDs will reach the

6 TB in 2014. Today's disks are made of a thin film of a magnetic alloy, which is composed of a mosaic of tiny grains. An ensemble of such grains act as magnetic elements. A single bit typically consists of 50 to 100 of these grains. If a single grain of a certain bit flips its magnetization spontaneously, the magnetic information of the whole bit is still valid. If too many grains start to flip, the corresponding bit of data is lost. As a consequence the magnetization will only be stable if the number of grains is high enough. Thus, to shrink the size of a bit, the size of the grains has to be shrunk as well. It seems that the state-of-the-art HDD technology reach a critical bit density, where the grains become so small that they approach the so-called superparamagnetic limit. A superparamagnetic grain might flip its magnetization due to ambient heat [5–7].

The easiest way to further increase the capacity of a storage device which comes to mind is to reduce the size of the bits. However, the superparamagnetic limit prevents to shrink the bit size in any order. This superparamagnetic behavior is known to increase with decreasing system size [8–10]. In the present thesis a new concept is proposed which allows to define the critical temperatures, i.e., the temperatures at which the system turns from one magnetic state (i.e., the ferro-, superpara-, or paramagnetic state) into another. The accurate determination of the critical temperatures allows to reduce the uncertainty limits and, hence, to decrease the bit size. For the infinite system, a magnetic phase transition is characterized by a divergence of the correlation length ξ, which characterizes the spatial decay of the spin-spin correlation function. For a nanosized system, on the other hand, it is by no means clear how the crossover at the Curie temperature manifests itself in the correlation function. Therefore, the goal was to provide a systematic analysis of the spin-spin correlation function for isotropic and anisotropic classical spin models in different dimensions with a finite and, in a thermodynamic meaning, small number of microspins. It will be shown, that for a finite system one can define a *reduced Curie temperature* $T_{\mathrm{C}}(L)$ from the modified spin-spin correlation function. As the main result, it is found that three different temperature scales, the blocking temperature $T_{\mathrm{b}}(L)$ and the reduced Curie temperature $T_{\mathrm{C}}(L)$ of the finite spin system as well as the Curie temperature of the infinite bulk $T_{\mathrm{C}}(\infty)$, can be read off from a suitably defined spin correlation function, which is accessible to scattering experiments. A simple three-parameter fit formula for the correlation function is proposed, which turns out to be very effective in describing the numerical data for the entire temperature range and may serve to give a definition for the reduced

Curie temperature that is consistent with the usual estimates of $T_C(L)$ based on the magnetic susceptibility or the specific heat. Finally, the blocking temperature, relative to the observation time, can easily be accessed by interpreting the Monte Carlo steps as time steps.

In order to develop new storage devices it is, besides the knowledge of the critical temperatures, important to understand the underlying physical processes that favor or hinder the magnetization switching of nanomagnets. Depending on the magnetic anisotropy, exchange parameter, size and shape, a monodomain particle may reverse its magnetization via nucleation and propagation rather than by a coherent rotation as proposed by the Neél-Brown model [5, 6]. In the present thesis an investigation of the size, the shape, and the temperature dependency of the superparamagnetic switching of individual magnetic nanoislands is presented. Like in the Neél-Brown model, an Arrhenius-like switching behavior is expected, with an energy barrier represented by the energy needed for the combined nucleation and domain wall formation. In particular it is studied how the energy barrier of an Fe/W(110) nanoisland depends on the ratio between the lengths in $[1\bar{1}0]$ and [001] direction. The presented study provides insights into the microscopic processes of magnetization reversal via domain wall nucleation and propagation. The switching rates and also the Arrhenius pre-factor and energy barrier have been found to be strongly dependent on the morphology of the simulated systems. The studies help to systematically tailor future magnetic nano-objects that hinder or favor magnetization reversal, which is important for the development of new types of data storage media or magnetic sensors at the nanoscale.

In order to catch up and maintain the projections given by the authors of [2] for HDD or other techniques like NAND Flash, storage manufacturers may have to consider new physical approaches not only for the bit design, but also for the reading and writing of magnetic information. Exciting developments towards new storage and logic devices are based on the current- and field-driven motion of magnetic domain walls [11–13]. In order to read or write a bit of information, a domain wall has to be moved towards the reading or writing devices. However, neither external fields nor currents allow to address each domain wall individually. A spin-polarized current moves neighboring domain walls in the same direction, while a magnetic field moves them in opposite directions. Up to now, the manipulation of an individual domain wall has been achieved by the stray field emanating from a tip of a magnetic force microscope (MFM) [14, 15]. The best resolution of the MFM experiments is of the order of 20 nm [15]. The goal of the presented investi-

gation is the manipulation of a narrow domain wall of width < 2 nm in a nanowire of monolayer thickness, which is about 1 order of magnitude smaller than that of walls in soft magnetic materials [14, 15]. For that purpose it is proposed to address a magnetic domain wall individually using the spin torque induced by a magnetic tip of an STM. The spins of the tunneling electrons transfer an angular momentum on the magnetic moments of the atoms underneath the tip. This phenomenon is usually referred to as spin transfer torque effect [16, 17]. It is demonstrated in the framework of a classical Monte Carlo simulation that the application of a polarized tunneling current allows the controlled manipulation and subsequent imaging of atomically sharp domain walls in nanoscale magnetic wires. The Monte Carlo simulations have been compared with atomistic spin dynamic simulations and it is shown that both theoretical approaches lead to the same results. Several different tip magnetizations have been analyzed and the orientation of the tip magnetization parallel to the domain wall magnetization has been revealed as the most promising geometry for future experimental applications. Furthermore, it is shown that magnetic defects present in the wire impede or even prevent a propagation of the domain wall. The defects are described as atoms with altered magnetic properties, which lead to a pinning of the domain wall.

In the following a brief overview of the present thesis is given. Chapter 2 reviews important theoretical aspects used in this work and introduces the applied classical Monte Carlo method.

In chapter 3 the manipulation of a narrow domain wall in a ferromagnetic nanowire, utilizing the spin-current induced by the tip of an STM, is presented. In contrast to experiments with a current applied parallel to the wire [11, 12], or with an extended external magnetic field [12, 13], this technique allows to address and control a single domain wall separately.

Chapter 4 is based on the simulations of chapter 3, but it additionally takes defects situated at the rim of the nanowire into account. The defects are defined as lattice sites with altered magnetic properties, which, for instance, could represent a nanowire grown at the step edge of a substrate. This chapter studies the influence of defects on the domain wall propagation and discusses the effect of domain wall pinning at defects.

The samples investigated in chapter 3 and chapter 4 have been studied at a very low temperature and the sample would reside in a thermally stable ferromagnetic state, as long as no external forces are applied. To learn more about the influence

of the temperature on the magnetization dynamics of the ferromagnetic system, a study of the so-called *critical temperatures* is presented in chapter 5. These critical temperatures assign the boundaries of the superparamagnetic region, hence, they define the temperatures at which the system turns from one magnetic state (i.e., the ferro-, superpara-, or paramagnetic state) into another and are known to depend crucially on the system size [8, 18]. The knowledge of the boundaries of the superparamagnetic temperature region is fundamental for studying the superparamagnetic magnetization dynamics of nanoislands presented in chapter 6. Moreover, the superparamagnetic region has been determined not only from well known methods, namely the specific heat C and the magnetic susceptibility χ [10], but also a new method is introduced, employing the spin-spin correlation function.

In chapter 6 the superparamagnetic switching of Fe/W(110) nanoislands is investigated. The domain wall nucleation and propagation process is studied in some detail and a size, shape, and temperature dependent investigation of the superparamagnetic switching presented.

Eventually chapter 7 summarizes and discusses the main results of the thesis and gives an outlook for future simulations and experiments. Note, that a focused discussion of results is given at the end of each chapter.

2 Some theoretical background

Parts of this chapter have been published in my diploma thesis: Thim Stapelfeldt, *Superparamagnetic Switching of Two-dimensional Magnetic Islands Studied by Monte Carlo Simulation*, Universität Hamburg, 2008 [19].

The performed Monte Carlo simulations shall give insights into the dynamics of an ensemble of interacting particles, i.e., exchange coupled magnetic spins. As the Monte Carlo method is based on statistical processes, in the present chapter important statistical and thermodynamical basics are briefly reviewed. It follows an introduction to the phenomenon of phase transitions and finite size effects, which becomes in particular important for the understanding of chapter 5. At the end, an introduction to the theory of Monte Carlo simulations is given and the single spin update Metropolis algorithm explained, which is the heart of the simulation.

2.1 Basics of statistical mechanics and thermodynamics

2.1.1 Probability distributions, partition function, and canonical ensemble

In a thermodynamic ensemble states are occupied with a certain probability p_μ. To describe such an ensemble statistically correct by means of a numerical simulation an appropriate probability distribution has to be used. In statistical mechanics, the Maxwell-Boltzmann statistics describes the statistical distribution of material particles over various energy states E_μ in thermal equilibrium, when the temperature is high enough and the density is low enough that quantum effects are negligible. This probability distribution is known as the Boltzmann distribution [20] and has been used for the simulations presented in this work:

$$p_\mu = \frac{1}{Z} \mathrm{e}^{-E_\mu \beta}, \tag{1}$$

where Z is the partition function and reads

$$Z = \sum_\mu \mathrm{e}^{-E_\mu \beta}. \tag{2}$$

Here, the summation goes over all possible states μ of the system and thus depends on the size L of the system and the degrees of freedom for each of the interacting spins. It can be shown that p_μ is the distribution which is most likely, if each particle in the ensemble can exchange energy with a heat bath or alternatively with a large number of similar particles. Equivalently, it is the distribution which has maximum entropy for a given average energy $\langle E_\mu \rangle$. Such an ensemble is usually denoted as canonical ensemble.

2.1.2 Expectation values

The relation to the macroscopic properties of an ensemble is given by the expectation value [20] of a certain quantity Q, which takes the value Q_μ in state μ:

$$\langle Q \rangle = \sum_\mu Q_\mu p_\mu. \tag{3}$$

The expectation value contains important information about the value of Q that one expects to measure in an experiment. Considering a canonical ensemble with a Boltzmann probability p_μ. From equations (1), (2) and (3) the expectation value of a quantity Q for a system in equilibrium is

$$\langle Q \rangle = \sum_\mu Q_\mu p_\mu = \frac{1}{Z} \sum_\mu Q_\mu \mathrm{e}^{-\beta E_\mu} = \frac{\sum_\mu Q_\mu \mathrm{e}^{-\beta E_\mu}}{\sum_\mu \mathrm{e}^{-\beta E_\mu}}. \tag{4}$$

The expectation value then is the average of the quantity over all states μ, weighted with its own Boltzmann probability. This is only applicable in very small systems. In larger systems one averages over a subset of states $\{1, ..., n\}$, but introduces some inaccuracy into the calculation. By increasing the number of states of the subset, the simulated average $\bar{Q}$ gets more accurate and most accurate for $n \to \infty$. Monte Carlo techniques work by choosing a subset of states at random from some probability distribution p_μ which has to be specified. The best estimate of the quantity Q will then be given by [21]

$$\bar{Q} = \frac{1}{n} \sum_{i=1}^{n} Q_i. \tag{5}$$

To reduce the inaccuracy on the one hand and reduce the computational effort on the other, an appropriate set of states is chosen by importance sampling (see Section 2.3.4).

2.1.3 Thermodynamic Potentials

As described in the previous section an expectation value of a certain quantity is achieved by time averaged measurements. It is useful to calculate the standard deviation of this quantity, because it gives the magnitude of the variation over time, denoted as fluctuations. These fluctuations may indicate a change in the specific properties of materials, see section 2.2.2. An important quantity is the mean square deviation of the energy

$$\left\langle (E - \langle E \rangle)^2 \right\rangle = \left\langle E^2 \right\rangle - \langle E \rangle^2. \tag{6}$$

$\langle E^2 \rangle$ can be determined from the derivative of the partition function, similar to the calculation of the expectation value of the energy $\langle E \rangle$:

$$\left\langle E^2 \right\rangle = \frac{1}{Z} \sum_{\mu} E_\mu^2 e^{-\beta E_\mu} = \frac{1}{Z} \frac{\partial^2 Z}{\partial \beta^2}. \tag{7}$$

This leads to

$$\left\langle E^2 \right\rangle - \langle E \rangle^2 = \frac{1}{Z} \frac{\partial^2 Z}{\partial \beta^2} - \left[\frac{1}{Z} \frac{\partial Z}{\partial \beta} \right]^2 = \frac{\partial^2}{\partial \beta^2} \ln Z. \tag{8}$$

The specific heat C is given by

$$C = (\left\langle E^2 \right\rangle - \langle E \rangle^2) \cdot k_\mathrm{B} \beta^2. \tag{9}$$

The specific heat C is a quantity, that gives the magnitude of fluctuations in energy. Similar to the specific heat C, the susceptibility $\chi = \frac{\partial \langle M \rangle}{\partial H}|_T$ describes the fluctuations of the magnetization M:

$$\chi = (\left\langle M^2 \right\rangle - \langle M \rangle^2) \cdot \beta. \tag{10}$$

The fluctuations scale with the number of particles L in the system like $1/\sqrt{L}$, in the three-dimensional case. With increasing L the fluctuations decrease until the thermodynamic limit is reached. Such fluctuations might be too small to be detectable in experiment, but in computer simulations they are observable and have been used to determine specific heat C and susceptibility χ.

2.2 Critical phenomena and phase transitions

2.2.1 Correlations

At the phase transition (see next section) the properties of a certain material change abruptly when an intensive variable reaches a critical value. Consider a ferromagnetic system consisting of localized spins. In the ferromagnetic phase the majority of the spins are aligned in parallel, but by crossing a critical temperature T_c, the system will transform into a paramagnet, where the spins of the system are arbitrarily oriented.

The correlation length ξ [22] is a measure of the spatial distance, within which the spins are parallel. ξ is defined via the correlation function [23]:

$$\langle \boldsymbol{S}_i \boldsymbol{S}_j \rangle \propto \mathrm{e}^{-\frac{|\boldsymbol{r}_j - \boldsymbol{r}_i|}{\xi}} \tag{11}$$

$\boldsymbol{S}_i$ represents the orientation of a spin $\boldsymbol{S}$ at position $\boldsymbol{r}_i$. Close to the phase transition $T \to T_\mathrm{c}$ the correlation length ξ reaches a magnitude in the range of the system size and diverges at $T \to T_\mathrm{c}$ for an infinite system. The correlation can be approximated by:

$$\xi \propto \left(1 - \frac{T}{T_\mathrm{c}}\right)^{-\nu}. \tag{12}$$

ν is a so-called critical exponent and is characteristic for the system's degree of freedom and dimension. An overview of critical exponents can be found in literature [24]. Due to the strong increase of ξ at $T \to T_\mathrm{c}$, the correlation length dominates the behavior of specific heat C or susceptibility χ at a phase transition.

In order to determine the partition function correctly with a numerical simulation, states at different time steps must be statistically independent. In terms of a Monte Carlo simulation a time step is represented by a Monte Carlo step (MCS), see section 2.3. To determine the correlation between different magnetic states, one introduces the magnetization M_k at k-th MCS. The statistical intercorrelation between states at k-th and $k + j$-th MCS is then given by the autocorrelation function

$$A(j) = \langle M_k M_{k+j} \rangle - \langle M_k \rangle \langle M_{k+j} \rangle, \tag{13}$$

where the average in equation (13) is over all system states k and $k + j$. In thermal equilibrium the autocorrelation function is independent of k and in an ideal case $A(j > 0) = 0$, if the system configurations are statistically independent. Numerically correlations are usually not avoidable and to estimate the correlations

one defines the autocorrelation time τ_{eq} by

$$A(\mathrm{j}) \propto \mathrm{e}^{-\frac{\mathrm{j}}{\tau_{eq}}}. \tag{14}$$

To receive reliable data from the Monte Carlo simulation at least $k \geq \tau_{eq}$ MCSs have to be performed, before starting the simulation. After τ_{eq} MCSs the system states are statistically independent and the system is considered to be in thermal equilibrium.

2.2.2 Phase transitions

In thermodynamics, a phase transition or phase change is the transformation of a thermodynamic system from one phase to another. A remarkable characteristic feature of a phase transition is an abrupt change in one or more physical parameters, in particular, the order parameters specific heat C and susceptibility χ. Figure 1 shows characteristic properties of first- and second-order phase transitions for an infinite system $L \to \infty$.

It shows schematically the behavior of the magnetization M, specific heat C and susceptibility χ. First order phase transitions are characterized by discontinuities of the order parameter. For a magnetic material the magnetization is referred to as an order parameter, because of the jump ΔM in the magnetization. This reflects the fact that at the critical point T_c, two (or more) phases can coexist.

A phase transition might be of any order n and is defined at a point where the n-th derivative of an order parameter is steady but the n-1st is not [20]. In chapter 5 second-order phase transitions are considered, thus the first derivative of the order parameter is steady. They are characterized by a divergent correlation length ξ (see Section 2.2.1) at the transition temperature T_c for infinite systems. The correlation length is a measure of the order in a system, it tells how microscopic variables at different positions are correlated. A diverging correlation length leads to a divergent peak in the specific heat C, with the internal energy as corresponding order parameter, and susceptibility χ, with magnetization as corresponding order parameter, see Figure 1.

In the case of the Heisenberg model the order parameter is continuous at T_c, thus the magnetization is steady and the transition is second order for the Heisenberg model and is called a continuous phase transition [21]. In contrast to infinite systems the peaks of the specific heat and the susceptibility are finite in finite systems. From the theoretical point of view no phase transitions in a system with

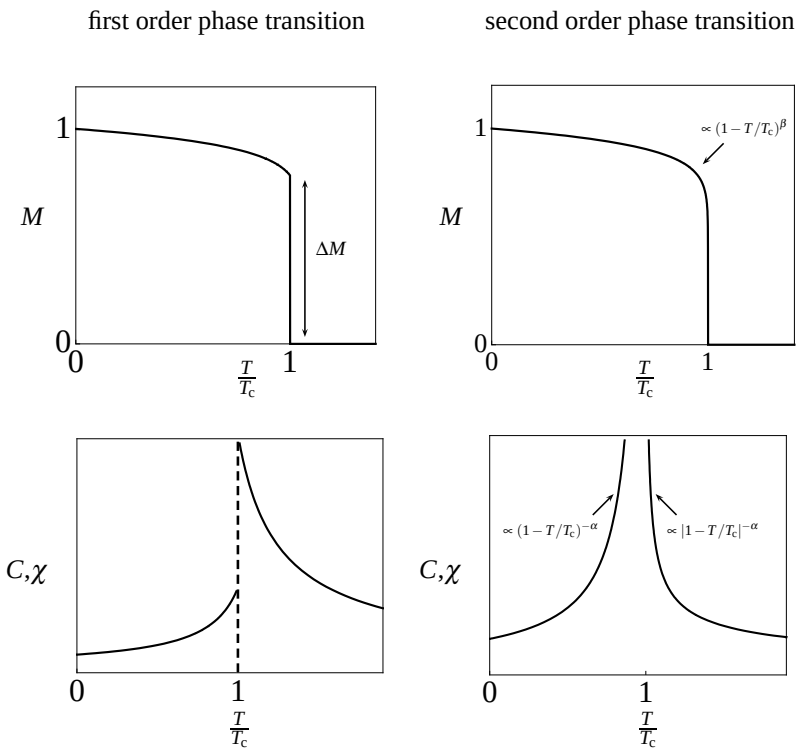

Figure 1: The left column shows the behavior of the magnetization M, specific heat C, and susceptibility χ as a function of temperature for a first order phase transition at the critical temperature T_c. The right column shows schematically a second order phase transition at the critical temperature T_c.

finite number of degrees of freedom exist. But also for finite systems the specific heat and susceptibility show pronounced peaks. With increasing system size the fluctuations, reflected in the specific heat and susceptibility, decrease and the peaks in $C(T)$ and $\chi(T)$ get sharper. As long as a simulated system is large enough to show a significant change of the order parameters and pronounced peaks in $C(T)$ and $\chi(T)$ exist, it will be considered that a phase transition has taken place in this work. Chapter 5 focuses on the determination of the critical temperatures of finite systems.

2.2.3 Finite size effects

The expected thermodynamic behavior of finite systems of interacting particles (spins in the present work) has been discussed by Fischer and Ferdinand [25, 26] in terms of a scaling theory involving critical exponents of the corresponding infinite system. They found the Curie temperature for a finite system shifted compared to

the Curie temperature $T_c(\infty)$ of the infinite system. This shifted temperature is called the reduced Curie temperature $T_c(L)$, with L the number of particles (spins) of the ensemble, and is usually defined by the maximum in the specific heat or susceptibility. The Curie temperature shifts to slightly higher temperatures than $T_c(\infty)$ for periodic boundary conditions. On the other hand, the data obtained in [10, 27] showed pronounced size dependence for lattices with free edges. In the case of open boundaries, the peaks in the specific heat are dramatically shifted to lower temperatures. This explains the term *reduced Curie temperature*. The shift is given by

$$\delta_{T_c} = [1 \pm \frac{T_c(L)}{T_c(\infty)}] \approx aL^{-\frac{1}{\nu}}, \quad L \to \infty. \tag{15}$$

Landau [10, 27] found that the effect of finite size on the variation of the internal energy is quite small for lattices with periodic boundary conditions except near to $T_c(\infty)$.

Finite size effects are qualitatively similar for the spontaneous magnetization. Only data obtained for open boundary conditions showed significant finite size effects below $T_c(\infty)$. The peaks in the susceptibility, for open boundaries, are shifted towards lower temperatures as well. Note, that all simulations presented in this thesis have been performed for finite systems and open boundary conditions have been used.

2.3 Theory to Monte Carlo simulations

2.3.1 Master equation

Consider a canonical ensemble representing some probability distribution p_μ; then $w_\mu(t)$ represents the occupation probability that the system will be in state μ at time t. The time dependent probabilities of a system to occupy each state is given by the so-called master equation

$$\frac{\mathrm{d}w_\mu}{\mathrm{d}t} = \sum_\nu [w_\nu(t)R(\nu \to \mu) - w_\mu(t)R(\mu \to \nu)]. \tag{16}$$

The first term on the right-hand side of the equation represents the rate at which the system is undergoing transitions into the state μ. The second term is the rate at which it is undergoing transitions out of μ into other states ν, while any transitions from state μ into any state ν, and vice versa, are possible. The occupation

probabilities must obey the following rules:

$$w_\mu(t) \geq 0 \text{ and } \sum_\mu w_\mu(t) = 1 \tag{17}$$

for all times t. After a sufficiently large time ($t \to \infty$), the ensemble will be in thermal equilibrium and the transition rates will take constant values,

$$w_\mu R(\mu \to \nu) = w_\nu R(\nu \to \mu), \tag{18}$$

so that equation (16) yields $\frac{\mathrm{d}w_\nu}{\mathrm{d}t} \to 0$ for all μ [23]. The rate at which the system makes transitions into and out of any state μ is equal. Equation (18) expresses the condition of detailed balance, which each Monte Carlo simulation has to satisfy for a correct simulation of equilibrium states. A probability to find a system in a state μ at the equilibrium is called the equilibrium occupation probability:

$$p_\mu = \lim_{t\to\infty} w_\mu. \tag{19}$$

In thermal equilibrium, the occupation probabilities are defined by the assumed probability distribution p_μ and the transition probabilities can be expressed as

$$\frac{R(\mu \to \nu)}{R(\nu \to \mu)} = \frac{p_\nu}{p_\mu} \tag{20}$$

in the limit of infinite times $t \to \infty$.

In a physical system at thermal equilibrium a state μ in phase space Ω is occupied with a certain probability p_μ. In the Monte Carlo simulation presented in this work a new state ν is generated according to the previous state μ, hence, according to the Markov process.

2.3.2 Markov Process

Let a system be in a state μ, then a Markov process [21] generates a new state ν of that system. The generation is at random and does not necessarily generate the same state ν each time it is in the initial state μ. The transition probability $R(\mu \to \nu)$ is the probability generating the state ν at given state μ. The transition probabilities of a Markov process should satisfy two conditions:

1. they should not vary over time

2. they should depend only on the properties of the current state μ and ν, and not on any other state the system has passed through.

The transition probabilities $R(\mu \to \nu)$ must also satisfy the constraint

$$\sum_{\nu} R(\mu \to \nu) = 1, \tag{21}$$

because the Markov process must be able to generate any state ν out of the state μ. As there may be a finite probability that the Markov process will stay in state μ, the transition probability $R(\mu \to \mu)$ needs not to be zero.

In a Monte Carlo simulation the Markov processes are used repeatedly to generate a Markov chain of states. Starting in a state μ the process generates a new state ν. Feeding the process with the state ν it will generate the next state λ, and so on. When the Markov process has run long enough, starting from any state of the system, it will eventually produce a sequence of states that appear with the probability distribution p_μ satisfying the condition of detailed balance. The system then is in thermal equilibrium.

2.3.3 Single spin update Metropolis algorithm

Let the probability of a system to be in state μ with energy E_μ in thermal equilibrium be described by the Boltzmann distribution, see equation (1). The Metropolis algorithm [28] applied in the present work realizes a Markov chain by single spin update dynamics (single flip algorithm). A single flip algorithm chooses a spin of the system randomly and changes its spin orientation into some direction. After each spin update, the energy of the new configuration is determined. If E_μ and E_ν denote the energy before and after the spin update, respectively, then the acceptance probability $A(\mu \to \nu)$ of the proposed spin update is given by

$$A(\mu \to \nu) = \min\left(1, \frac{p(\nu)}{p(\mu)}\right), \tag{22}$$

satisfying the criterion of detailed balance. If $E_\mu > E_\nu$, the transition is always accepted, hence, $A(\mu \to \nu) = 1$. If $E_\mu < E_\nu$, the transition is accepted according to the Boltzmann probability and the equation (22) yields

$$A(\mu \to \nu) = \frac{p_\nu}{p_\mu} = \frac{\mathrm{e}^{-E_\nu \beta}}{\mathrm{e}^{-E_\mu \beta}} = \mathrm{e}^{-\Delta E \beta}. \tag{23}$$

It means that in Metropolis single spin update, the spin update is always accepted if the energy is lowered. However, even if the energy is increased, the update is accepted with a certain probability $\exp(-\Delta E\beta)$. By that means the Metropolis algorithm leads to a minimization of the free energy in thermal equilibrium.

2.3.4 Importance Sampling

The acceptance of a new generated state according to the Metropolis algorithm explained in the previous section is denoted as importance sampling. It ensures that the best estimate of the quantity Q (see equation (5)) reduces to a simple arithmetic mean

$$\bar{Q} = \frac{1}{n}\sum_{i=1}^{n} Q_i. \tag{24}$$

The equilibrium properties of a system can be obtained, when the measurements are started after waiting a certain number of steps, which is at least as large as the corresponding autocorrelation time τ_{eq} (see section 2.2.1).

With a proper selection of states in thermal equilibrium the estimator $\bar{Q}$ is calculated with reasonable accuracy and computer time.

2.3.5 Error Estimation

In an experiment one would like to get an impression what the statistical errors of the measured quantities are. Suppose a quantity Q is distributed according to some function with expectation value $\langle Q\rangle$. After n statistically independent observations $\{Q_i\}$ of this quantity an unbiased estimator for the expectation value $\langle Q\rangle$ is given by the arithmetic mean of equation (24). The computed mean square deviation δQ is

$$\delta Q = \sqrt{\frac{1}{n}\sum_{i}^{n}(Q_i - \bar{Q})^2} = \left\langle Q^2\right\rangle - \langle Q\rangle^2 . \tag{25}$$

Q_i is a value of a quantity in state i and $\bar{Q}$ is the arithmetic mean of all states n. The task is to find estimates for the unknown parameter $\{Q_i\}$ of the underlying distribution and to control the errors. The following relation holds only for large n. As shown in equation (5) an estimate is

$$\langle Q\rangle \approx \bar{Q} \tag{26}$$

with a mean square error of $\langle Q \rangle$ of

$$\delta_{\langle Q \rangle} \approx \frac{1}{n-1} \overline{\delta}_{Q^2}. \tag{27}$$

To ensure one has received reliable expectation values $\langle Q \rangle$ in an experiment or simulation, the mean square error has to be minimized. To determine the mean square error $\delta_{\langle Q \rangle}$, a measurement of the same quantity Q has to be repeated several times. In a Monte Carlo simulation random number algorithms are used to create new states. It is necessary, that the production of random numbers is fast and efficient. Random numbers are produced with the help of an algorithm that is per se deterministic and therefore predictable. These sequences are only *pseudo-random* and do have limitations which are discussed in literature, e.g., in Numerical Recipes [29]. It is known that poor quality random number algorithms can lead to systematic errors in Monte Carlo simulations. To avoid such systematic errors, a random number generator should behave similar to realizations of independent, identically distributed random variables. The algorithms used in this thesis are taken from [29] and are known to satisfy independency and identical distribution of random numbers.

To simulate independent measurements, the starting condition of the applied random number generator has to be changed, so that a different set of random numbers is created. Independent simulations in this work means simulations with different starting conditions defined by the so-called *seed* of the random number generator.

3 Manipulation of a domain wall in a ferromagnetic nanowire utilizing an STM tip

In this chapter a study of the controlled manipulation of a single domain wall in a ferromagnetic nanowire is presented. In the proposed procedure a spin-polarized current is induced by a magnetic tip of an STM. The tip is placed above a magnetic nanowire and then moved along the wire's long axis, with a current flowing through the vacuum barrier. The angular momentum from the spin-polarized current exerts a torque on the magnetic moments underneath the tip and leads to a displacement of the domain wall. Particularly, the manipulation of a ferromagnetic 180° transverse domain wall has been studied by means of Monte Carlo simulations.

Parts of the material presented in this chapter has been originally published in *Physical Review Letters*: "T. Stapelfeldt, R. Wieser, E. Y. Vedmedenko and R. Wiesendanger, *Domain Wall Manipulation with a Magnetic Tip*, Phys. Rev. Lett., 107, 2, 027203 (2011)" [30] Copyright (2011) by the American Physical Society.

The present chapter starts with an introduction to the properties of the nanoparticle under investigation. It follows a theoretical description of the tunneling current, which is defined by the Tersoff-Hamann model. Then the simulation scheme of the Monte Carlo simulation is presented. Thereafter, a theoretical description of the domain wall propagation through the Peierls potential of the discrete lattice is given and first results of successful domain wall manipulation are presented. It follows a discussion on how a very localized perturbation, such as a tunneling current, can lead to the propagation of an extended domain wall. Then, additional simulations are presented for the domain wall manipulation with different tip magnetizations and the results are compared with spin-dynamic simulations. Eventually, the spin-polarized part of the current is analyzed, because it allows to compare the theoretical results with future experiments, as the spin-polarized part of the current is proportional to the $\mathrm{d}I/\mathrm{d}U$ signal of an STM.

3.1 The system properties and the simulation scheme

3.1.1 The model and corresponding experimental systems

For a realistic simulation one needs system parameters, like the exchange and the anisotropy constants, which define the magnetic properties of the system. The

material parameters used in the simulations are typical for experimental investigations on ultrathin films [31–42]. Note, that the range of material parameters specify a class of hard magnetic materials like Fe/W(110), but do not represent any concrete system. Hence, the results of this work can be adapted to all systems possessing similar properties. A welcoming effect for numerical simulations is, that dipolar interactions are negligible in such systems due to the anisotropy lying in-plane. As dipolar interactions are long ranged, neglecting them drastically decreases the computational time of the simulation.

For Fe/W(110) it is known, that due to the diffusion energy, iron wires grow smoothest along the [001] direction and least smooth along $[1\bar{1}0]$ [43]. Therefore, the sample systems have been created in the xy-plane, which shall correspond to the (110)-plane of tungsten. The x-direction in the simulation corresponds to [001], and the y-direction to $[1\bar{1}0]$, see Figure 2. A maximal lateral dimension of about $N_x \times N_y \approx 80 \times 30$ atomic rows (AR) has been modeled, which matches the dimensions of an Fe/W(110) nanostripe of about 15 nm × 7 nm. N_x and N_y are the number of atomic rows in x- and y-direction. Each lattice site is occupied by a classical Heisenberg moment $\boldsymbol{S}_i = (S_x, S_y, S_z)_i = (S_{[001]}, S_{[1\bar{1}0]}, S_{[2,2,1]})_i$ of unit length. The easy-axis of the monolayer Fe/W(110) lies along $[1\bar{1}0]$ [44] and a hard-axis is assumed to lie out-of-plane [45]. Furthermore, for Fe/W(110), density functional theory calculation [46] revealed a change of the exchange coupling along different spatial directions, compared to bulk iron, which is due to a lattice mismatch of about 10% [47]. A combined experimental and theoretical study [48] of Fe/W(110) nanowires estimates the best overall accordance of a ratio of the exchange constants between first, second, and third nearest neighbors of $J_1 : J_2 : J_3 = J_{[001]} : J_{[1\bar{1}1]} : J_{[1\bar{1}0]} = 1 : 2 : 4$. As the implemented code allows to calculate long range interactions, the mentioned anisotropic exchange has been considered in the simulation. The magnetic properties of the sample system are then described by the following Hamiltonian:

$$\begin{aligned}\mathcal{H} = -J_{[001]} \sum_{\langle ij \rangle} \boldsymbol{S}_i \boldsymbol{S}_j - J_{[1\bar{1}1]} \sum_{\langle ij \rangle} \boldsymbol{S}_i \boldsymbol{S}_j - J_{[1\bar{1}0]} \sum_{\langle ij \rangle} \boldsymbol{S}_i \boldsymbol{S}_j \\ -K_y \sum_i (S_y^i)^2 + K_z \sum_i (S_z^i)^2,\end{aligned} \tag{28}$$

where $J_{[hkl]} > 0$ denotes the effective nearest neighbor exchange coupling constant along different crystallographic directions defined by the miller indices h,k, and l, see [49] for more details. $K_y > 0$ is an easy-axis anisotropy pointing along

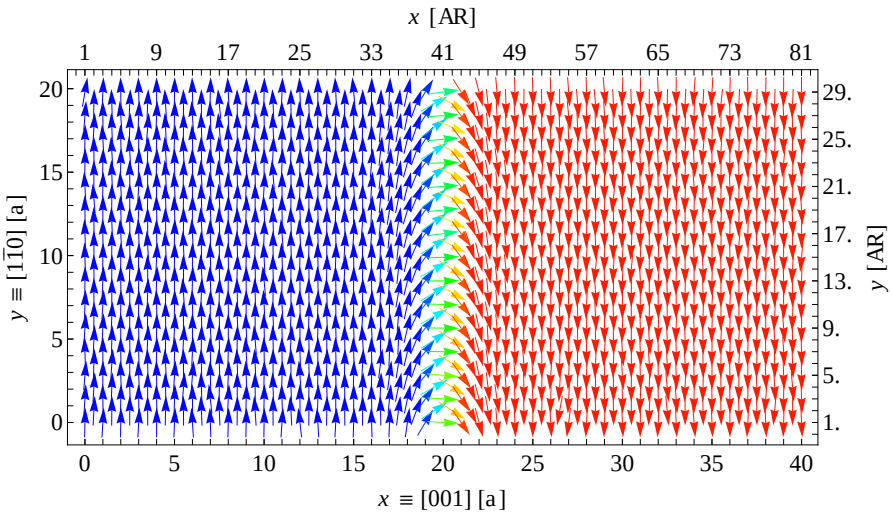

Figure 2: Sketch of a simulated nanowire. Two ferromagnetic domains (blue and red), consisting of about 600 Heisenberg moments each, separated by a 180° transverse domain wall. The moments in the domain are oriented along the easy-axis. The second x and y axis show the length of the nanowire in atomic rows (AR).

$y = [1\bar{1}0]$, and $K_z > 0$ an out-of-plane hard-axis anisotropy. The first three sums run over all nearest neighbors along a certain crystallographic direction and the last two sums run over all lattice sites i.

3.1.2 The different sets of energy constants used in the simulations

Four different sets of parameters have been used for the studies presented in this thesis. The reason for using different parameters is on the one hand to optimize the computational effort according to the problem under investigation, which crucially depends on the complexity of the considered Hamiltonian, and on the other hand, to be able to compare results for different ferromagnetic systems. Table 1 summarizes all different sets of energy constants used. Note, that SET1 and SET2 have been used in the present chapter. Apart from the different exchange and anisotropy constants J and K, the underlying crystal lattice used for the parameter set is given, and a chapter which contains results of the given parameter set.

To ensure a reasonable simulation time, the parameters have been adjusted to the problem under investigation, thus, according to the computational demand and the available computer resources. For instance the simulation of a system with exchange interactions up to third nearest neighbors, defined by SET1, is much more time consuming than a simulation taking only first nearest neighbors into account, e.g., defined by SET2. However, all sets represent the same class of physical

	SET1	SET2	SET3	SET4
Lattice	BCC(110)	SC	SC	BCC(110)
Chapter	3, 4	3	5	6
J_1	1	1	1	-
J_2	2 J_1	-	-	1
J_3	4 J_1	-	-	2 J_2
K_y	1 J_1	0.125 J_1	$0.6J_1$	0.44 J_2 /0.043 J_2
K_z	1 J_1	$0.05J_1$	-	-

Table 1: The table summarizes the different sets of material parameters used for the simulations in this work. The exchange interaction constants for first, second, and third nearest neighbors (J_1,J_2,J_3), and anisotropy constants for the in-plane easy-axis K_y and the out-of-plane hard-axis anisotropy K_z are given. SET4 shows two different constants of the easy-axis anisotropy used: the first belongs to lattice sites situated at the rim of the nanoisland and the second to lattice sites on the surface.

systems introduced in the previous section. All simulations have been performed in the computing center PHYSnet-Rechenzentrum, which has experienced a vast increase of the computational resources in the last years allowing to perform more and more extensive calculations.

3.1.3 The system properties and the geometry of the ferromagnetic nanowire

For the study of the controlled domain wall manipulation a 180° transverse domain wall, with an orientation along the y-axis, has been placed in the middle of a nanowire with fixed dimension, as illustrated by Figure 2 and 3. The chosen exchange and anisotropy constants lead to a width δ_{DW} of the relaxed domain wall in the range of a few atomic distances, which is typical for ferromagnetic materials of such high anisotropy [35, 50]. The black dashed line in Figure 3 is a hyperbolic tangent fit on the row-wise averaged magnetization $M_y(x) = \frac{1}{N_y}\sum_1^{N_y} m_y(x)$, which is the averaged magnetization over all moments along the y-axis for each atomic row along x. Hence, the black dashed line gives the averaged shape of the domain wall, which corresponds to the spin-configuration displayed in Figure 2. The green shaded area indicates the area S_0 of the domain wall.

Simulations have been performed for two different parameter sets. SET1 has been used to represent a monolayer of ferromagnetic material with an anisotropic exchange, like iron on the tungsten (110) surface, and SET2 has been used for simulating an isotropic ferromagnetic monolayer on a square lattice. The param-

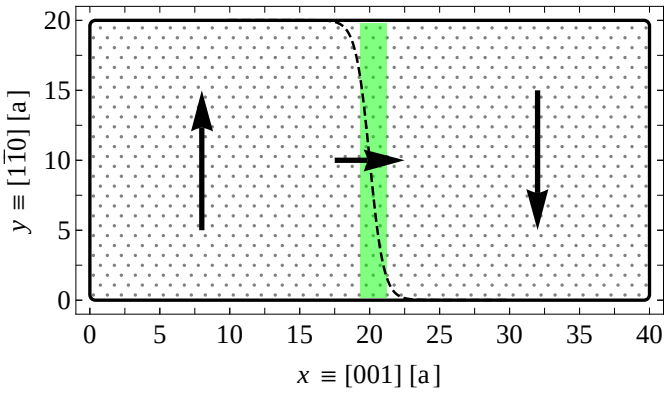

Figure 3: Sketch of the nanowire including a 180° transverse domain wall with an orientation along the y-axis. The black arrows indicate the orientation of the magnetization in the domains and the domain wall. The green rectangle illustrates the area S_0 of the domain wall and the black dashed line is a hyperbolic tangent fit on the averaged domain wall profile.

eter set SET2 has been used, in order to compare the results of the Monte Carlo simulation with spin-dynamic simulations, which have been performed by Robert Wieser for nanowires on a square lattice.

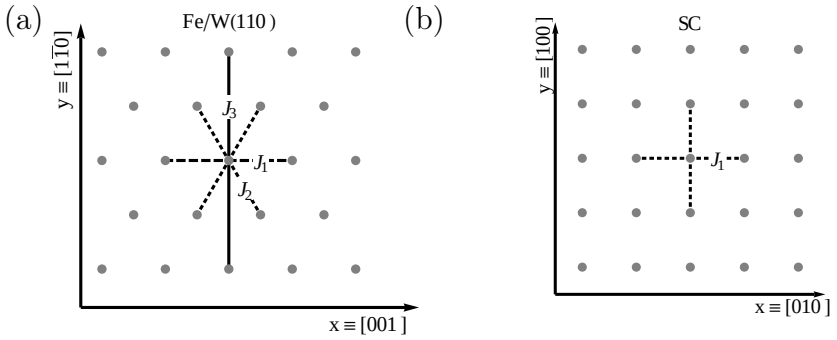

Figure 4: Sketch of the exchange bonds considered in the simulations for Fe/W(110) in (a) and for the two-dimensional square lattice in (b).

For the simulations presented in this chapter a perfect crystal structure of the nanowires has been assumed. However, in experiments imperfections of samples occur and become evident as defects in the material's crystal structure. In order to study also the effect of magnetic defects on the domain wall propagation, chapter 4 presents additional simulations for a nanowire including defects. The next section introduces the model used to account for the spin-polarized tunneling current of an STM in the simulations.

3.1.4 The spin-polarized tunneling current

In section 3.3, the influence of a spin-polarized current, induced by the tip of an STM, on the domain wall position is presented (a detailed description of spin-polarized scanning tunneling microscopy (SP-STM) can be found elsewhere [51]). For that purpose one needs a model to describe the current induced by a magnetic tip and a model, which describes the interaction between the spin-polarized current and the magnetic moments of the sample. The tunneling current has been defined by the extended version of the Tersoff and Hamann model, which includes the spin-polarized contribution to the current [52, 53]:

$$\boldsymbol{\mathcal{T}}(\boldsymbol{r}_{\mathrm{tip}}, \theta) = \boldsymbol{\mathcal{T}}_{\mathrm{U}}(\boldsymbol{r}_{\mathrm{tip}}) + \boldsymbol{\mathcal{T}}_{\mathrm{P}}(\boldsymbol{r}_{\mathrm{tip}}, \theta), \tag{29}$$

where $\boldsymbol{\mathcal{T}}_{\mathrm{U}}$ is the unpolarized part and $\boldsymbol{\mathcal{T}}_{\mathrm{P}}$ the polarized part of the tunneling current; $\boldsymbol{r}_{\mathrm{tip}}$ denotes the position of the tip and θ is the angle between the tip magnetization $\boldsymbol{m}_{\mathrm{tip}}$ and the magnetization of the atoms in the sample $\boldsymbol{S}_i$. Tersoff and Hamann modeled the tip apex atom as a spherically symmetric s wave, at the point where it approaches nearest to the sample surface. Furthermore, they assumed that the *spin-up* and *spin-down* s wave states can be characterized by the same decay constant κ ($\kappa = \hbar^{-1}\sqrt{(2m\phi)}$) and the work function ϕ of the tip is equal to that of the surface. Then they obtained an exponential decay of the tunneling current as a function of the distance [52]. As the non-polarized contribution to the current density in the Tersoff-Hamann picture is a constant factor, here, only the polarized current contribution is shown:

$$\boldsymbol{\mathcal{T}}_i = -\mathcal{T}_0 \cdot \mathrm{e}^{-2\kappa r_i} \cdot P \cdot \boldsymbol{m}_{\mathrm{tip}}, \tag{30}$$

with $r_i = |\boldsymbol{r}_{\mathrm{tip}} - \boldsymbol{r}_i|$ the distance between the tip and the atom i of the sample, P the polarization of the tip magnetization $\boldsymbol{m}_{\mathrm{tip}}$ (a unit vector in the direction of the tip magnetization), and $\mathcal{T}_0$ the spin-polarized current averaged over the surface unit cell. For simplicity, a fully polarized current has been assumed by setting P equal to unity. From equation (30) it follows, that the current density decreases exponentially with the distance between tip and sample. As a consequence, the majority of electrons, tunneling through the vacuum barrier, interact with the atoms directly underneath the tip only.

To understand the model, which describes the transfer of a spin-torque between the tunneling s electrons and the localized moments of the sample, the authors of

[54] write that

"[...] one has to recognize two types of electrons: spin-dependent transport is provided by electrons at or near the Fermi level and the magnetization dynamics can involve electrons below the Fermi sea".

As in real ferromagnets it is impossible to unambiguously separate electrons of transport from electrons of magnetization, it has been conventionally modeled in an s-d Hamiltonian. In this so called s-d model, the coupling between the spins $\boldsymbol{\mathcal{T}}_i$ of the itinerant $4s$ conduction electrons and the spins $\boldsymbol{S}_i$ of the $3d$ localized electrons is given by the s-d exchange interaction $-J_{\mathrm{sd}}\boldsymbol{\mathcal{T}}_i\boldsymbol{S}_i$ [17] (illustrated in Figure 5):

$$\mathcal{H}_{\mathrm{sd}} = -J_{\mathrm{sd}} \sum_i \boldsymbol{\mathcal{T}}_i \boldsymbol{S}_i, \tag{31}$$

where J_{sd} is the s-d exchange integral. J_{sd} has been set equal to one, so that all information on the spin-polarized current is given by $\boldsymbol{\mathcal{T}}_i$. The s electrons transform

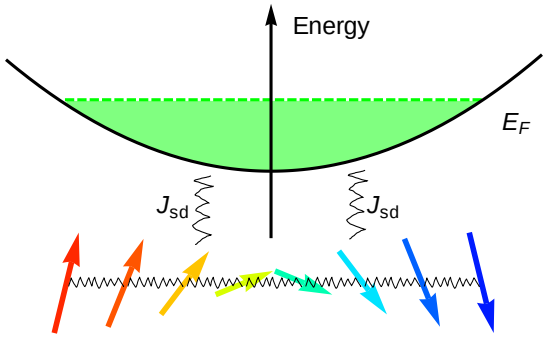

Figure 5: Illustration of the coupling between the tunneling s electrons and the localized d electrons, as described by the s-d model. Electrons from the Fermi sea are coupled by the couplings constant J_{sd} with the moments of the crystal atoms.

a torque on the localized d electrons and align the magnetic moments of the atoms into the direction of the tip magnetization.

The influence of the spin-torque on domain walls in nanowires has been investigated intensively in the past [17, 55–57]. In the cited theoretical investigations, the dynamics of a domain wall propagation has been modeled by spin-dynamic simulations, employing the Landau-Lifshitz-Gilbert equation (LLG) [16, 17, 58, 59]. In that model, the spin-torque is represented in the LLG equation by an additional

precession term and an additional relaxation term (highlighted):

$$\frac{\partial \boldsymbol{S}_i}{\partial t} = -\frac{\gamma}{(1+\alpha^2)}\boldsymbol{S}_i \times \boldsymbol{H}_i - \frac{\alpha\gamma}{(1+\alpha^2)}\boldsymbol{S}_i \times (\boldsymbol{S}_i \times \boldsymbol{H}_i) + \underbrace{\mathcal{C}\boldsymbol{S}_i \times \boldsymbol{\mathcal{T}}_i}_{precession} + \underbrace{\mathcal{D}\boldsymbol{S}_i \times (\boldsymbol{S}_i \times \boldsymbol{\mathcal{T}}_i)}_{relaxation}, \tag{32}$$

with the gyromagnetic ratio γ, the Gilbert damping α, the *internal field* $\boldsymbol{H}_i = -\partial\mathcal{H}_i/\partial\boldsymbol{S}_i$, the spin-current $\boldsymbol{\mathcal{T}}_i$, and two constants $\mathcal{D}$ and $\mathcal{C}$. The precession term leads to a precession of the magnetic moments around the axis of the tip magnetization and the relaxation term leads to an alignment of the magnetic moments along the direction of tip magnetization. In a spin-dynamic simulation, a system will go to its energy minimum on a predefined path through the phase space, which is defined by equation (32). On the contrary, in a Monte Carlo simulation, the path to reach the minimum of the total energy is arbitrary. Nevertheless, with the assumption made in section 2.3, the system will end up in a thermodynamically stable configuration. In the Monte Carlo simulation the influence of the spin-torque is reproduced by a ferromagnetic-like coupling between tip and sample, and is incorporated in the simulation by the additional Hamiltonian $\mathcal{H}_{\mathrm{sd}}$, see equation (31). This *s-d* Hamiltonian is similar to a Hamiltonian of an external magnetic field, like used in [60], but depends on the position of the tip. It represents a very localized and non-homogeneous interaction like the spin-current induced by an STM tip. Such a spin-current leads to a minimization of the total energy, if the magnetic moments underneath the tip are aligned parallel to the tip magnetization. To crosscheck the capability of the Monte Carlo simulation to reproduce the influence of the spin-torque, the results of the Monte Carlo simulation have been compared with spin-dynamic calculations in section 3.3, published in [30].

The next section gives an introduction into the used Monte Carlo simulation scheme.

3.1.5 The simulation scheme of the Monte Carlo simulation

The simulations have been performed with a completely relaxed 180° transverse domain wall at low temperature ($T = 0.01\ J/k_{\mathrm{B}}$). Figure 6 illustrates the tip-wire setup in the simulation. The tip has been initially placed far away from the domain wall with a constant tip magnetization $\boldsymbol{m}_{\mathrm{tip}}$ and at a height h of two lattice constants above the wire. Then, a constant spin-polarized current

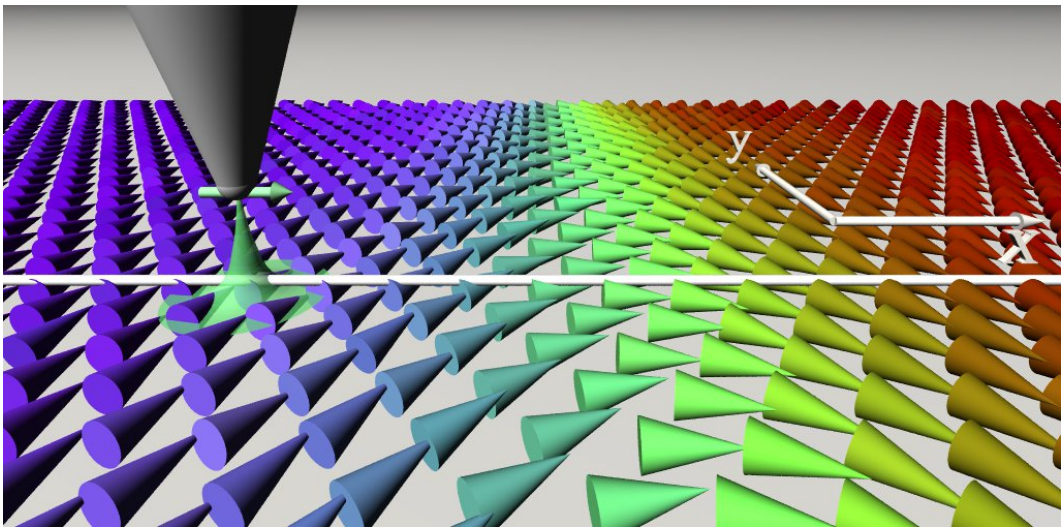

Figure 6: Scheme of a spin configuration of the sample. A domain wall elongated along the y-axis separates two domains. The spins in the domains point along the easy-axis, hence, along y. A tip with a magnetization $\boldsymbol{m}_{\text{tip}}$ and height h above the sample moves towards the domain wall along the indicated track into $+x$-direction (white horizontal line) with a spin-current applied.

has been switched on. From equation (31) a maximal energy of about 100 meV results, which is induced into the system. A current of such intensity does not affect the domain wall position as long as the tip is far away. The tip starts to move towards the domain wall with a constant tip velocity into the $+x$-direction. After a tip displacement of $\Delta x_{\text{tip}} = 0.1$ lattice constants (a) the system has been relaxed for 15 000 MCSs (each step calculated within the Metropolis algorithm), which corresponds to a tip velocity of $V_{\text{tip}} = 1.5 \times 10^{-5}\ a$ per MCS. After the relaxation at each tip-step, the net magnetization has been calculated. Initially the magnetization is zero, as the domain wall is placed in the middle of the wire, separating two equally sized domains with opposed magnetization. A change of the domain wall position x_0, due to a domain wall propagation, is visible as a change in the magnetization. For all manipulation trials 200 tip-steps have been performed and the domain wall position determined at each step. A manipulation trial is defined as successful, if the domain wall is manipulated until the end of the wire, hence, if the net magnetization of the wire switches from initially zero to one. To assure reliable statistics of the simulation, each manipulation trial has been repeated several times for different seeds of the random number generator.

The next section introduces the domain wall propagation in the Peierls potential of the discrete lattice using the example of a one-dimensional chain.

3.2 Propagation of a domain wall on a discrete lattice: the Peierls potential

If a domain wall propagates in a magnetic material it has to pass through different spin configurations as it moves from one atomic row to another. From the literature [50, 61] it is known that if the domain wall width is close to the lattice spacing one must take into account the effect of the discrete structure of the lattice on the propagation of such a domain wall. Figures 7 (a) and (b) show two principal spin

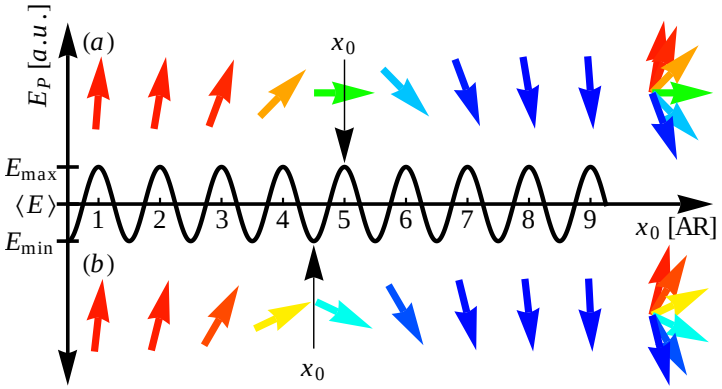

Figure 7: The Peierls potential as a function of the domain wall center position x_0. The black solid line shows the spatial dependence of the domain wall energy in respect to the domain wall center position x_0. The two spin configurations displayed correspond to the domain wall center lying at an atomic row (a) and between two atomic rows (b). These two configurations exhibit the maximum and minimum total energy of the system, respectively.

configurations of a domain wall in a ferromagnetic chain — these configurations exhibit the maximum and minimum total energy of the system and correspond to the center of the wall (x_0) lying at or between atomic rows, respectively. This spatial variation of the domain wall energy due to the change of the spin configuration (black solid line in Figure 7) is generally referred to as the *Peierls potential* $V_{\mathrm{P}}(x)$ or the *Peierls energy* $E_{\mathrm{P}}(x)$, which is the activation energy for the domain wall motion in an ideal crystal. The energy modulation is a result of the changing alignment between neighboring spins during the domain wall propagation. The authors of [50, 62] predicted a sinusoidal dependence on coordinate of the domain wall energy in a cubic lattice and expressed the total wall energy as:

$$E_{\mathrm{P}}(x) = E_{\mathrm{PN}} \sin^2\left(\frac{\pi x}{d}\right), \tag{33}$$

where d is the inter-atomic distance along the x axis and E_{PN} the amplitude of the wall energy. The black solid line in Figure 7 illustrates the dependency of the Peierls energy on the coordinate x. E_{PN} corresponds to the energy difference of the two spin configurations depicted in Figure 7, with the maximum and minimum energy, and is often referred to as *Peierls-Nabarro barrier*, $E_{\mathrm{PN}} = E_{\mathrm{max}} - E_{\mathrm{min}}$. From numerical calculations the authors of [62] found that the amplitude of the Peierls potential depends exponentially on the parameters of the domain wall:

$$E_{\mathrm{PN}} \propto \frac{cJ_{[hkl]}S^2}{a^2} \exp(-\frac{\pi\delta_{\mathrm{DW}}}{d}), \tag{34}$$

where c = 1 for the simple cubic lattice, c = 2 for the bcc lattice and c = 4 for the fcc lattice [63].

In 1940 the Peierls potential was introduced by Peierls for dislocations [64–66] and about fifty years after that, it was discovered in the pinning of vortices in superconducting materials [67]. Another two decades later the influence of the Peierls potential on the propagation of a ferromagnetic domain wall was experimentally observed for the first time by Novoselov *et al.* in 2003 [68], using the state-of-the-art technique of ballistic Hall micromagnetometry.

In an ideal system without defects the intrinsic pinning is determined by the Peierls-Nabarro barrier, which is also denoted as *pinning barrier* in the following. This pinning barrier has to be overcome in order to successfully manipulate the domain wall. That can be achieved by increasing the thermal energy of the system or for instance by applying an external magnetic field or a polarized current. In the case of a domain wall depinning by thermal excitations only, the domain wall propagation takes place according to the random walk theory [69] (see also section 6.3.1). However, when applying an external magnetic field the orientation of the field defines the direction of the domain wall propagation. If applying a spin-polarized current, it is the polarization of the current which defines the direction of the domain wall propagation. The application of an external magnetic field or a current results in a pressure f applied to the domain wall existing in the system. If this external pressure f is sufficiently large, it leads to a propagation of the domain wall. The external pressure causes a modulation of the internal field and is, therefore, denoted as *effective internal field* in the following.

Figure 8 schematically illustrates the total energy of a defect free crystal with a propagating domain wall for three different values of the external pressure f. As external pressure an extended magnetic field pointing along the easy axis is

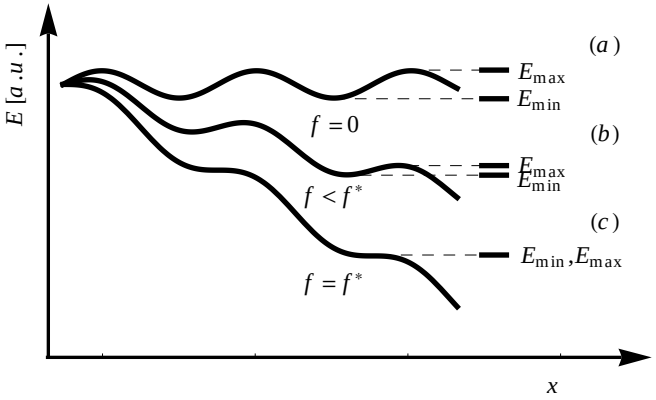

Figure 8: Sketch of the spatial dependence of the total energy of a ferromagnetic chain with a propagating domain wall. Without external pressure (a) and with an external pressure smaller than the depinning field (b), and with an external pressure equal to the depinning field (c). As external pressure an extended magnetic field pointing along the easy axis is assumed.

assumed. At zero field (a) all energy minima are identical, which corresponds to the center of the domain wall lying between atomic rows. Also all energy maxima are identical, which corresponds to the wall center lying atop of an atomic row. Hence, the energy curve has no inclination, there is no driving force acting on the domain wall and the transition from one to another stable position *between the sites* can be achieved only stochastically due to thermal fluctuations. If now an external pressure exists, one of the two propagation directions becomes energetically preferred. Hence, if the domain wall propagates towards the energetically favorable direction, the total energy will decrease as shown by Figure 8 (b-c). For a constant domain wall velocity V_{DW} this decrease is linear. The authors of [70] propose a spatial dependence of the perturbed wall energy $E_{\mathrm{P}}^{f}(x)$ in the form

$$E_{\mathrm{P}}^{f}(x) = S_0(E_{\mathrm{P}}(x) - f(x)), \tag{35}$$

where S_0 is the area of the wall. They divide the range of the external pressure into two regions: $f < f^*$ and $f \geq f^*$. For all $f < f^*$ a pinning barrier $E_{\mathrm{PN}} > 0$ exists, while for all $f \geq f^*$ the pinning barriers disappear. These two situations are depicted in Figure 8 (b) and (c). The authors of [70] call the regime of motion shown in Figure 8 (a-b) the *activated regime*, as here thermal energy is needed for a domain wall propagation. They call the situation illustrated in Figure 8 (c), where the wall can move without thermal assistance, the *non-activated* regime. They mathematically distinguish between these two regimes by comparison of the

external pressure and the maximal steepness of the potential $f^* = \mathrm{Max}[\mathrm{d}E_\mathrm{P}/\mathrm{d}x]$: the activated regime corresponds to $f < f^*$, the non-activated regime to $f > f^*$. The external pressure has to be larger than f^* in order to depin the domain wall in the non-activated regime. In the following, f^* will be denoted as the *depinning field*.

In the next section the tunneling current induced by the tip of an STM will be introduced as a local perturbation of the Peierls potential and results of the current induced domain wall manipulation are presented.

3.3 Manipulation of a domain wall by means of a localized current

The energy landscape of a domain wall moving through a one-dimensional wire, under the influence of an extended magnetic field or current, is shown in Figure 7. If now a magnetic tip, with a polarized current flowing from tip to sample, is placed in the vicinity of the domain wall, the energy landscape changes locally due to the energy contribution of the *s-d* Hamiltonian (equation (31)). Figure 9 illustrates, at two different tip positions x_1 and x_2, the energy landscape of the Peierls potential modified by a polarized tunneling current, for a tip magnetization parallel (a) and anti-parallel (b) to the domain wall orientation. For a parallel alignment the illustration shows that the total energy can be minimized if the domain wall is situated directly underneath the tip. If the pinning barrier of the domain wall is sufficiently reduced by the induced current, the domain wall can propagate towards the tip and thereby reduce the total energy of the system. On the contrary, for the anti-parallel alignment, the increased potential barrier hinders the domain wall to move towards the tip, hence, the domain wall in Figure 9 (b) will move away from the tip in order to keep the total energy minimal.

This one-dimensional demonstration can also be used to explain the findings of the simulations for the two-dimensional case. Figure 10 shows the manipulation curves, i.e., the domain wall position x_0 as a function of the time, for a tip magnetization parallel (black) and anti-parallel (red) to the domain wall. The simulations have been performed at $T < 0.01\ J/k_\mathrm{B}$ using SET1 of Table 1. As long as the tip is far away from the domain wall the induced current does not affect the domain wall position, thus, besides some thermal fluctuation the net magnetization of the nanowire does not change. When the tip approaches the wall the domain wall starts to propagate if a critical distance r_c to the wall is reached.

The *s-d* Hamiltonian then has changed the energy landscape so much that the domain wall propagates towards the nearest minimum (which can lie either in $+x$- or $-x$-direction, depending on the tip magnetization). In other words: The spin-torque is transformed into kinetic energy leading to a domain wall propagation, which decreases to zero when the minimum of the total energy is reached.

For the parallel alignment of tip and wall ($\boldsymbol{m}_{\text{tip}} \uparrow\uparrow \boldsymbol{S}_{\text{DW}}$) the spin-torque is maximal when the tip is above the domains. Hence, the angle θ between the orientation of the tip magnetization and the orientation of the magnetic moments underneath the tip is $\pi/2$. The spin-torque is minimal if the tip is situated above the domain wall ($\theta = 0$). Also the *s-d* Hamiltonian reaches its minimum value if tip and wall are aligned in parallel, as clear from Figure 9 (a). Consequently, the domain wall propagates towards the tip in order to minimize the total energy. In the manipulation curves shown in Figure 10 after approximately 2.4×10^6 MCSs ($x_{\text{tip}} \approx 15\ a$) the magnetization decreases at the moment when the domain wall leaves its initial position and propagates towards the tip. For the remaining manipulation trial the domain wall stays in the energy minimum underneath the tip, hence, follows the tip and is successfully manipulated until the end of the wire.

In the case of an anti-parallel alignment ($\boldsymbol{m}_{\text{tip}} \uparrow\downarrow \boldsymbol{S}_{\text{DW}}$) the spin-torque again is maximal when the tip is above the domains ($\theta = -\pi/2$) and minimal above the domain wall ($\theta = \pi$). However, the energy contribution of the *s-d* Hamiltonian leads to an increasing total energy when the tip approaches the domain wall, leading to a maximal total energy above the domain wall center, as clear from Figure 9 (b). As a result, the domain wall avoids the tip and stays always in front of it. Again, the domain wall is successfully manipulated, as shown by the black curve in Figure 10 (a). Hence, both types of the tip magnetization are capable to manipulate the domain wall, but in essentially different ways: One by creating a potential valley, which traps the domain wall and allows the domain wall being pulled along with the tip, i.e., the parallel alignment $\boldsymbol{m}_{\text{tip}} \uparrow\uparrow \boldsymbol{S}_{\text{DW}}$; and one by an increased potential barrier underneath the tip, which pushes the domain wall out of the wire, i.e., the anti-parallel alignment $\boldsymbol{m}_{\text{tip}} \uparrow\downarrow \boldsymbol{S}_{\text{DW}}$.

On the timescale of the simulation one can say, that the simulation of the manipulation of a domain wall has been performed in the non-activated regime. The applied temperature is too small for the domain wall to overcome the pinning barrier. Nevertheless, the temperature manifests itself in small fluctuations of the simulated expectation values, see Figures 10 (b).

In the next section it is discussed in detail, how a localized perturbation, like

a spin-polarized tunneling current, can lead to the propagation of an extended domain wall, even though the local perturbation is about 50 times smaller than the extension of the domain wall.

3.3.1 How does a localized current displace an extended 2D domain wall?

If one considers a domain wall in a two-dimensional system with a localized current applied, it is not clear how such a current can reduce the pinning barrier for the whole extended domain wall. It will be shown, that the reduction of the pinning barrier is a time-dependent process. In the two dimensional nanowire, the change of the energy landscape underneath the tip spreads through the system via the exchange interaction of neighboring moments. To start the discussion and before presenting results of the simulation, a domain wall propagation is schematically demonstrated in this section.

Figure 11 shows an illustration of the spin configurations of three atomic rows of a two dimensional nanowire for three different time steps t_1, t_2, and t_3. The black solid lines display the energy landscapes of the domain wall propagation for each atomic row considering the exchange interactions along y only and the tunneling current. The change in energy due to the on-site anisotropy and the exchange coupling along x, as shown in Figure 7, is ignored in this scheme because it is identical for the three rows and constant over time. The applied current changes the energy landscape in the ith row only and it reduces the potential energy about two lattice constants in front of the domain wall center, visible as a pronounced potential valley in $-x$-direction. The direction of the effective internal field created by the current depends on the orientation of the domain wall and points, in the case shown in Figure 11, into the $-x$-direction.

The exchange energy along the y-direction (E_{J_3}) is minimal if the domain wall centers of each row reside at the same x-position. In such a case all moments along y are aligned in parallel, as shown in Figure 11 (a). (a) corresponds to the first MCS t_1 at which the current is switched on. Starting the simulation leads to a relaxation of the domain wall center of the ith row into the minimum underneath the tip at t_2, as shown in Figure 11 (b). As a result the internal field acting on the domain wall center of the ith row vanishes, but the displacement of the ith domain wall center alters the exchange interaction between magnetic moments along the y-direction and, as a consequence, creates an internal field in the $i\pm1$th rows pointing

into the $-x$-direction. The energy landscapes of the neighboring rows ($i \pm 1$th) show, that the energy minimum is then shifted into the $-x$-direction. In order to minimize the total energy and to reduce the effective internal field the neighboring domain wall centers ($i \pm 1$th) have to propagate towards that position, because the energy minimum created by the current keeps the ith domain wall center trapped underneath the tip. In this scheme the domain wall centers of the $i \pm 1$th rows propagated with a delay compared to the ith row.

Such a delayed propagation of different atomic rows described above can be extracted from the simulations. Figure 12 shows the position of the domain wall center x_0^i for two different atomic rows, with i the number of the atomic row along the y direction. For two neighboring rows, shown in Figure 12 (a), the rows propagate almost simultaneously and both curves nearly coincide. This becomes more clear when subtracting both curves from each other resulting in a mean displacement $\langle \Delta x_0^{\Delta i} \rangle$ between both rows of $0.041 \pm 0.035\ a$, shown by the insets in Figure 12. Because of the short distance between the two rows ($r_y = \sqrt{2}\ a$) the domain wall center positions of both rows are strongly correlated and the relaxation of both rows takes place on the time scale of a single tip-step (15 000 MCSs). Figure 12 (b) shows x_0 for a row in the middle of the wire close to the path of the tip (red) and a row close to the edge of the wire (black), $r_y = 5 \times \sqrt{2}\ a$. Obviously, the domain wall center at the edge propagates with some delay compared to the domain wall center that is closer to the tip, leading to a five times larger mean displacement of $0.2 \pm 0.08\ a$ than that of the two neighboring rows in (a). The larger mean displacement indicates a smaller correlation of the domain wall position x_0^i for rows that are far apart one from another than those close to each other.

To find out more about the correlation between the domain wall center position of different atomic rows i, the correlation function for x_0^i as a function of the distance $r = |r_y^j - r_y^i|$ between two atomic rows along y has been calculated, defined as follows:

$$G_{x_0}(r) = \frac{1}{n(r)} \sum_{i<j} \langle x_0^i x_0^j \rangle, \tag{36}$$

with $n(r)$ being the number of occurrence of the distance r, and i and j the index of atomic rows. $\langle \cdots \rangle$ denotes the time averaging during manipulation and corresponds to a time interval of $\tau = 1.5 \times 10^6$ MCSs. For more details on correlation functions see also section 2.2.1. Figure 13 shows the correlation function $G_{x_0}(r)$ as a function of the distance r in (a) and the correlation function for each row with its closest neighboring rows in (b) (averaged over 1st, 2nd, and 3rd nearest

neighboring rows). Figure 13 (a) points out that the correlation of the domain wall position between two rows decreases with increasing distance between the rows. As expected, the correlation is maximal for nearest neighboring rows and decreases reaching a minimum at $r = 12\,\mathrm{AR}$, which is close to half the width of the nanowire.

The decreasing slope of $G_{x_0}(r)$ for large r indicates that the correlation between atomic rows at the edges are larger than for atomic rows inside the wire, which becomes more clear when looking at the correlation between neighboring atomic rows as a function of the atomic row position i, shown in Figure 13 (b). This representation clearly shows that the correlation between rows at the edges on either side of the wire is higher than for rows inside the wire. The reason for the correlated propagation of the domain wall centers at the edge is the more effective exchange coupling between the rows due to a reduced coordination number of the edge rows. Striking in Figure 13 (b) is a sudden increase at $i = 13$ AR, which is due to the rows lying directly on or close to the tip's path and is reflecting the strong but localized influence of the induced current on the domain wall center in the middle of the nanowire.

The simulations show that the correlation between magnetic moments of atomic rows in a distance r close to the exchange length l_{ex} ($l_{\mathrm{ex}} \approx r$) is very high, but magnetic moments far away ($l_{\mathrm{ex}} > r$) are less correlated. As a consequence the propagation of the domain wall center is more delayed for rows which are farther away from the tip. The described behavior makes clear that the current does not reduce the pinning barrier for the whole domain wall, but rather causes the displacement of a part of the domain wall directly underneath the tip. This displacement then, due to the change of the exchange energy, leads to the subsequent propagation of the atomic rows that are situated farther away. Hence, the change of the exchange energy leads to an increasing effective internal field. In a similar fashion, Novoselov *et al.* describe in [68] the propagation of a domain wall between Peierls valleys:

"[...] where at first only a submicrometre segment of a domain wall (a jog) moves to the next valley. Spreading the boundary of such a jog along the wall eventually leads to the relocation of the whole domain wall".

The next section presents results of the domain wall manipulation for six different tip magnetizations. Moreover, it presents a comparison of results obtained

from the Monte Carlo simulations with spin-dynamic simulations.

3.4 Manipulating with different tip magnetizations

This section summarizes the results of the domain wall manipulation with a magnetic tip obtained from Monte Carlo simulations and spin-dynamic simulations for six different tip magnetizations. Besides the two tip-sample geometries discussed in section 3.3 four additional setups have been simulated and spin-dynamic simulations have been performed by Robert Wieser in order to compare the results of the two simulation methods. The chosen tip-sample geometries can be categorized into three principal scenarios each defined by the axis along which the tip magnetization is oriented:

I With a tip magnetization parallel ($\boldsymbol{m}_{\mathrm{tip}} \uparrow\uparrow \boldsymbol{S}_{\mathrm{DW}}$) or anti-parallel ($\boldsymbol{m}_{\mathrm{tip}} \uparrow\downarrow \boldsymbol{S}_{\mathrm{DW}}$) to the domain wall magnetization $\boldsymbol{S}_{\mathrm{DW}}$

II With a tip magnetization parallel ($\boldsymbol{m}_{\mathrm{tip}} \uparrow\uparrow \boldsymbol{S}_{\mathrm{D}}$) or anti-parallel ($\boldsymbol{m}_{\mathrm{tip}} \uparrow\downarrow \boldsymbol{S}_{\mathrm{D}}$) to the domain magnetization $\boldsymbol{S}_{\mathrm{D}}$

III With a tip magnetization out-of-plane ($\boldsymbol{m}_{\mathrm{tip}} \odot \boldsymbol{S}_{xy}$) or in-plane ($\boldsymbol{m}_{\mathrm{tip}} \otimes \boldsymbol{S}_{xy}$), which are perpendicular to $\boldsymbol{S}_{\mathrm{D}}$ as well as to $\boldsymbol{S}_{\mathrm{DW}}$.

Figure 14 shows the domain wall position as a function of the time for all tip magnetizations, derived from Monte Carlo simulations in the first column (MC) and for spin-dynamic calculations in the second column (LLG). (I a) and (I b) correspond to scenario I, with a tip magnetization parallel or anti-parallel to the domain wall. The first scenario has been discussed in section 3.3, although different lattices and system parameters have been used in the Monte Carlo simulations presented in section 3.3 and, here, the results are essentially the same (for a summary of the used parameters see Table 1). From Figures 14 (I a) and (I b) one can deduce that the two different simulation methods lead to the same results. Differences between the results originate, on the one hand, from thermal fluctuations in the Monte Carlo simulations and, on the other hand, from different time scales of the two simulation methods.

In the second scenario (II) the tip magnetization is collinear with the domain magnetization $\boldsymbol{S}_{\mathrm{D}}$. The spin-torque is minimal above the domains for both cases, since the angle θ between the tip magnetization and the magnetic moments of the atoms underneath the tip is π for $\boldsymbol{m}_{\mathrm{tip}} \uparrow\uparrow \boldsymbol{S}_{\mathrm{D}}$ or 0 for $\boldsymbol{m}_{\mathrm{tip}} \uparrow\downarrow \boldsymbol{S}_{\mathrm{D}}$. In the case

of the tip magnetization parallel to the initial domain magnetization the energy contribution of the *s-d* Hamiltonian is maximal negative and, therefore, the total energy minimal. When the tip approaches the domain wall the energy contribution of the *s-d* Hamiltonian increases due to the non-collinearity of the magnetization in the domain wall ($\pi > \theta > 0$). To keep the energetically favorable situation (before the tip-wall approach) the domain wall has to propagate into the $+x$-direction. In other words, the spin-torque increases when the tip approaches the domain wall and in order to reduce the torque the wall starts to propagate away from the tip. As the domain wall stays in front of the tip, one can say that the domain wall has been pushed by the tip, this manipulation mode is called the *pushing mode*. In the case of the $\boldsymbol{m}_{\mathrm{tip}} \uparrow\downarrow \boldsymbol{S}_{\mathrm{D}}$ geometry the energy contribution of the *s-d* Hamiltonian is maximal positive, thus, the total energy maximal. When the tip approaches the domain wall the total energy decreases and reaches its minimum when the tip is positioned above the second domain, hence, it has to cross the domain wall. To achieve that situation the domain wall propagates into the $-x$-direction, thus, in the direction opposite to the tip motion. Finally, the total energy of the system has been minimized — the tip has crossed the domain wall and moves further into the $+x$-direction leaving the domain wall behind.

In the last scenario (III) the tip magnetization points in- ($\boldsymbol{m}_{\mathrm{tip}} \otimes \boldsymbol{S}_{xy}$) or out-of-plane ($\boldsymbol{m}_{\mathrm{tip}} \odot \boldsymbol{S}_{xy}$) of the nanowire. The spin-torques acting on the magnetic moments in the domains and the domain wall are equal. However, due to the weak exchange coupling of the magnetic moments in the domain wall the spin-torque aligns the moments parallel to the tip. The absolute minimum of the energy for $\boldsymbol{m}_{\mathrm{tip}} \otimes \boldsymbol{S}_{xy}$ as well as for $\boldsymbol{m}_{\mathrm{tip}} \odot \boldsymbol{S}_{xy}$ is reached when the domain wall is positioned directly underneath the tip, which can only happen if the magnetic moments can be aligned along the z-axis. Results shown in Figure 14 (III a) correspond to a system with a weak hard-axis anisotropy along z, allowing the energy minimization by rotating magnetic moments into- or out-of-plane. For this reason, in the Monte Carlo simulations shown in Figure 14, the domain wall is attracted by the tip and then remains underneath it until the end of a manipulation trial. Hence, the domain wall is pulled by the tip in both cases, this manipulation mode is called the *pulling mode*.

In the spin-dynamic procedure a tip with an out-of-plane magnetization pulls the domain wall, while an in-plane magnetization pushes the domain wall ahead, see Figure 14 (III b). The main role for the different behavior, compared to the Monte Carlo simulation, plays the first term of equation (32) used in the spin-

dynamic calculations. This term requires a clockwise rotation of the magnetization with respect to the internal field $\boldsymbol{H}_i$. The spin-torque (the fourth term of equation (32)) tries to align the magnetization of the sample along the hard-axis. In order to avoid this energetically unfavorable situation the domain wall moves along the x-axis. In the Monte Carlo simulation a system always goes towards the minimum of the total energy. The way the system does it is arbitrary. It is different for the spin-dynamics simulation, where the kinetic energy of the second term of equation (32) leads to a motion of the wall away from the tip for $\boldsymbol{m}_{\mathrm{tip}} \otimes \boldsymbol{S}_{xy}$, while towards the tip for the $\boldsymbol{m}_{\mathrm{tip}} \odot \boldsymbol{S}_{xy}$ geometry. Therefore, the domain wall immediately finds the global minimum with zero torque for the $\boldsymbol{m}_{\mathrm{tip}} \otimes \boldsymbol{S}_{xy}$ geometry and remains in a local minimum for the $\boldsymbol{m}_{\mathrm{tip}} \odot \boldsymbol{S}_{xy}$ geometry (pushing mode).

The different modes obtained in the framework of the two simulation methods for the $\boldsymbol{m}_{\mathrm{tip}} \otimes \boldsymbol{S}_{xy}$ geometry (pulling for Monte Carlo simulation and pushing for spin-dynamics) appear for currents strong enough to align magnetic moments into the hard-axis only. Additional Monte Carlo simulations for an enhanced hard-axis anisotropy of 5 meV showed that for scenario III manipulation is not possible, as the spin-torque is too weak to align the moments out of the plane. To gain a better understanding of the described behavior and make a link to the experiments, the experimentally accessible spin dependent tunneling conductivity σ_{sp} has been analyzed and is presented in the next section.

3.5 Simulation of conductivity curves

The conductivity of a tunnel junction with two ferromagnetic electrodes (tip and sample) is proportional to the scalar product $\sigma_{\mathrm{sp}} = \boldsymbol{m}_{\mathrm{tip}} \cdot \boldsymbol{S}_i$ [16, 71]. It is maximal for the parallel ($\theta = 0$) and minimal for the anti-parallel ($\theta = \pi$) magnetization orientation of the two electrodes. In the spin-resolved spectroscopic mode of SP-STM experiments [51] the $\mathrm{d}I/\mathrm{d}U$ curves correspond to the position dependent changes in the conductivity $\sigma_{\mathrm{sp}}(x_{\mathrm{tip}})$. As all information on $\sigma_{\mathrm{sp}}(\boldsymbol{r}_{\mathrm{tip}})$ is incorporated into the *s-d* Hamiltonian it is possible to calculate $\sigma_{\mathrm{sp}}(\boldsymbol{r}_{\mathrm{tip}}) \propto \langle J_{\mathrm{sd}} \boldsymbol{\mathcal{T}}_i \boldsymbol{S}_i \rangle$ and predict $\sigma_{\mathrm{sp}}(x_{\mathrm{tip}}) \sim I/U$.

Conductivity curves for the scenario I are plotted in Figure 15 (a). For this scenario two different manipulation modes have been identified. In the case of a parallel alignment of tip and wall ($\boldsymbol{m}_{\mathrm{tip}} \uparrow\uparrow \boldsymbol{S}_{\mathrm{DW}}$) the tip has been situated above the center of the domain wall and it pulled the domain wall along to the end of the wire. In the case of anti-parallel alignment of tip and wall ($\boldsymbol{m}_{\mathrm{tip}} \uparrow\downarrow \boldsymbol{S}_{\mathrm{DW}}$) the

domain wall has been pushed a couple of lattice constants in front of the tip during the whole manipulation trial until the wall reaches the end of the wire. When using this knowledge for the interpretation of the calculated conductivity curves it becomes clear that σ_{sp} increases while the tip crosses the wall for $\boldsymbol{m}_{\mathrm{tip}} \uparrow\uparrow \boldsymbol{S}_{\mathrm{DW}}$ (black circles) and subsequently remains constant when pulling the domain wall. For $\boldsymbol{m}_{\mathrm{tip}} \uparrow\downarrow \boldsymbol{S}_{\mathrm{DW}}$ the conductivity remains unchanged, because the domain wall is pushed ahead in $+x$-direction.

In the $\boldsymbol{m}_{\mathrm{tip}} \uparrow\uparrow \boldsymbol{S}_{\mathrm{D}}$ geometry (black circles) of scenario II, shown in Figure 15 (b), σ_{sp} is maximal above the initial domain ($\theta = 0$). When the tip reaches the domain wall the conductivity does not change, because the domain wall is pushed ahead in $+x$-direction keeping θ close to zero. For $\boldsymbol{m}_{\mathrm{tip}} \uparrow\downarrow \boldsymbol{S}_{\mathrm{D}}$ (red rectangles), σ_{sp} is minimal above the initial domain ($\theta = \pi$). Approaching the domain wall, σ_{sp} increases due to a motion of the wall towards the tip and finally underneath the tip. In order to retain this energetically favorable situation the tip loses contact. It moves further across the domain magnetized parallel to the tip magnetization, keeping σ_{sp} maximal ($\theta = 0$).

In the last scenario III ($\boldsymbol{m}_{\mathrm{tip}} \otimes \boldsymbol{S}_{xy}$ and $\boldsymbol{m}_{\mathrm{tip}} \odot \boldsymbol{S}_{xy}$) the spin dependent conductivity shown in Figure 15 (c) increases when the tip crosses the domain wall and then remains constant when pulling the domain wall, in both cases. The displacement between the two curves is due to thermal fluctuations. The conductivity increases after the tip-wall contact, because the spin-torque aligns the magnetic moments of the domain wall parallel to the tip. For a large hard-axis anisotropy, where the spins cannot be aligned out of the plane, the conductivity curve would remain constant.

The characteristic shape of the $\sigma_{\mathrm{sp}}(\boldsymbol{r}_{\mathrm{tip}})$ as well as x_0 dependencies permit to make a clear conclusion about the dynamical regime of the domain manipulation, hence, pushing or pulling mode.

3.6 Summary and Conclusion

The manipulation of a narrow domain wall in a ferromagnetic nanowire utilizing a localized spin-current of an STM has been studied theoretically by means of Monte Carlo simulations. It has been found that due to the discreteness of the lattice and the fact that the width of the domain wall is on the scale of the lattice constant the domain wall is intrinsically pinned by the Peierls potential. In order to manipulate a domain wall the applied current has to depin the domain wall via reduction of

the Peierls potential. The results of the simulation show that the current does not reduce the pinning barrier of the entire domain wall, but causes the displacement of a segment of the domain wall underneath the tip. This displacement then, due to the change of the exchange energy, leads to a jogwise propagation of the rest of the domain wall.

For six different tip magnetizations, it has been demonstrated that all tip-sample geometries are suitable for domain wall manipulation, but an analysis of costs and benefits reveals the geometry with a tip magnetization parallel to the domain wall magnetization $\boldsymbol{m}_{\mathrm{tip}} \uparrow\uparrow \boldsymbol{S}_{\mathrm{DW}}$ as the optimal one. The $\boldsymbol{m}_{\mathrm{tip}} \uparrow\uparrow \boldsymbol{S}_{\mathrm{DW}}$ alignment assures the maximal possible conductivity and, furthermore, allows to manipulate the domain wall in both directions along the x-axis. This geometry has been chosen in order to study the influence of magnetic defects on the domain wall propagation, presented in the following chapter. Two different manipulation modes have been identified, namely the pushing mode and the pulling mode.

The theoretical time and distance dependence of the spin dependent conductivity σ_{sp} shows characteristic features for each geometry studied and can be used in future SP-STM experiments for identification of the corresponding manipulation modes.

As mentioned by Novoselov [68, 72] thermal excitation and domain wall pinning at defects make the detection of the Peierls potential very complicated in experiments. Even for the presented simulation, which has been carried out for very low temperatures and without defects, the Peierls potential could not be resolved. The reason for that will be discussed in the following chapter.

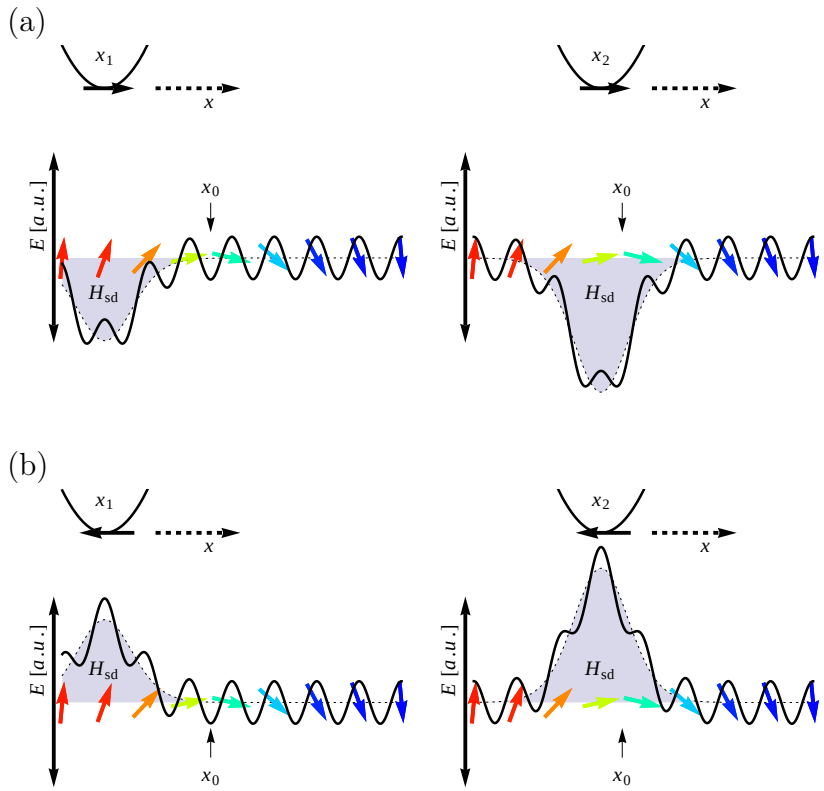

Figure 9: Schematic representation of the spin configuration of a domain wall in a ferromagnetic chain (colored arrows) and the Peierls potential perturbed by a local spin-current (solid black line), for two different tip positions x_1 and x_2. The energy landscape for a tip magnetization parallel to the domain wall magnetization is shown in (a), and for an anti-parallel tip magnetization in (b). For the parallel alignment the spin-current leads to a local decrease of the energy barrier and for the anti-parallel alignment to a local increase of the energy barrier. The dotted arrow indicates the propagation direction of the tip.

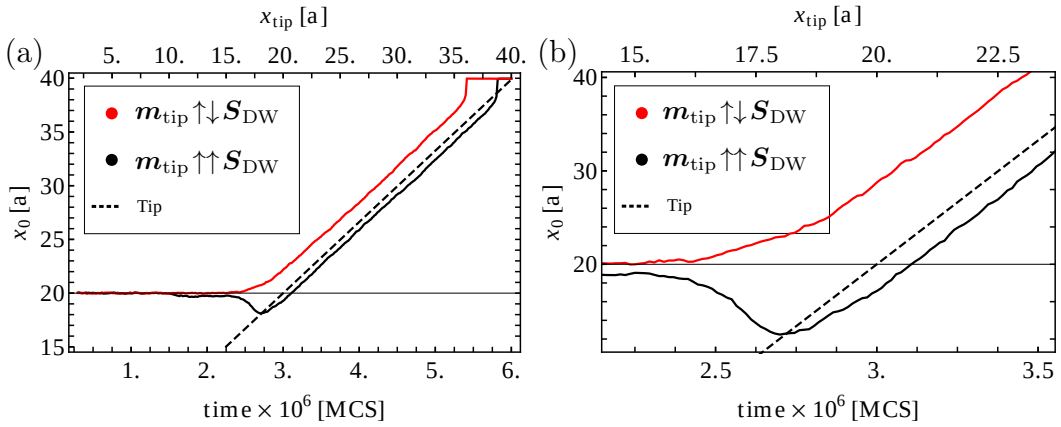

Figure 10: Monte Carlo simulation of the manipulation curves for two successful domain wall manipulations. The black curve corresponds to a tip magnetization oriented parallel to the domain wall orientation ($\boldsymbol{m}_{\mathrm{tip}} \uparrow\uparrow \boldsymbol{S}_{\mathrm{DW}}$), and the red curve to a tip magnetization oriented anti-parallel to the domain wall orientation ($\boldsymbol{m}_{\mathrm{tip}} \uparrow\downarrow \boldsymbol{S}_{\mathrm{DW}}$). A 180° transverse domain wall has initially been placed at $x_0 = 20\ a$. (a) shows the complete manipulation trials, and (b) a section of the manipulation curve in the region of the tip-wall approach. In (b) the thermal fluctuations are slightly more distinct in comparison to (a). The tip moves with constant velocity as marked by the dashed line.

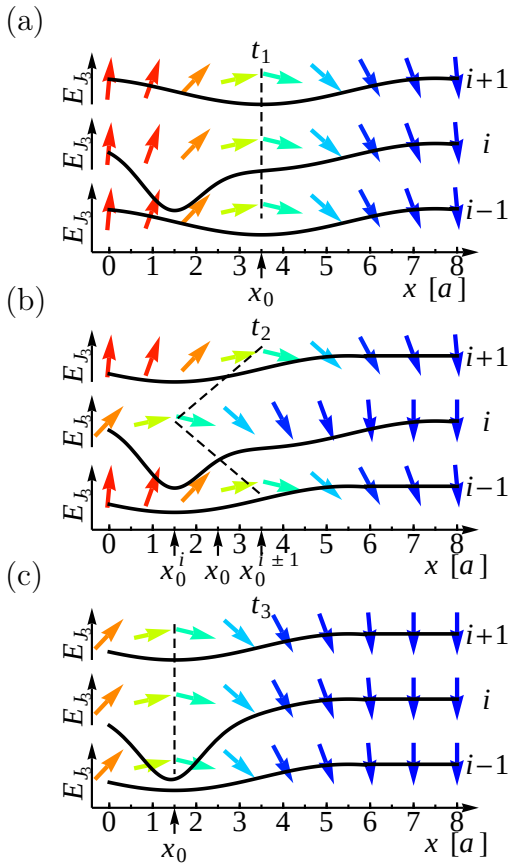

Figure 11: Schematic drawing of three successive time steps illustrating the domain wall relaxation. The black solid lines represent the energy landscapes of the domain wall propagation without the Peierls potential. A current which locally changes the potential in the ith row at the first time step t_1 leads to a relaxation of the domain wall center of the ith row towards this minimum at t_2. In order to minimize the total energy, the domain wall centers of the neighboring rows $(i \pm 1)$ relax to the same x position at t_3.

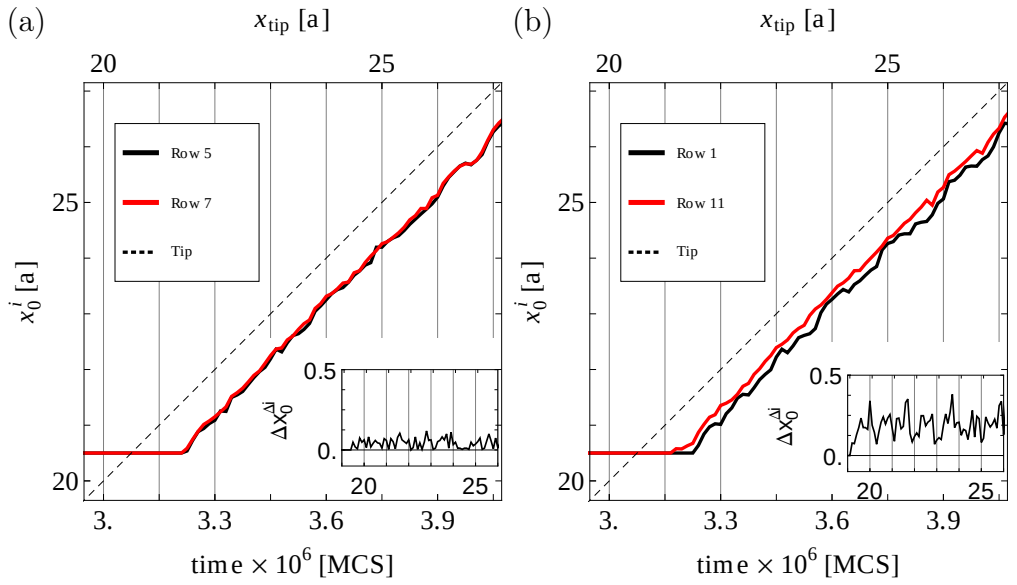

Figure 12: The position of the domain wall center x_0^i during the manipulation for single atomic rows i. (a) x_0^i for two neighboring rows and in (b) for two rows far apart. A 180° transverse domain wall has initially been placed at $x_0 = 20\ a$ and the dashed line corresponds to the position of the tip. The inset on the right-hand bottom shows the difference of the two curves. The simulations have been performed for a tip magnetization parallel to the wall magnetization $\boldsymbol{m}_{\mathrm{tip}} \uparrow\uparrow \boldsymbol{S}_{\mathrm{DW}}$ using SET1 of Table 1.

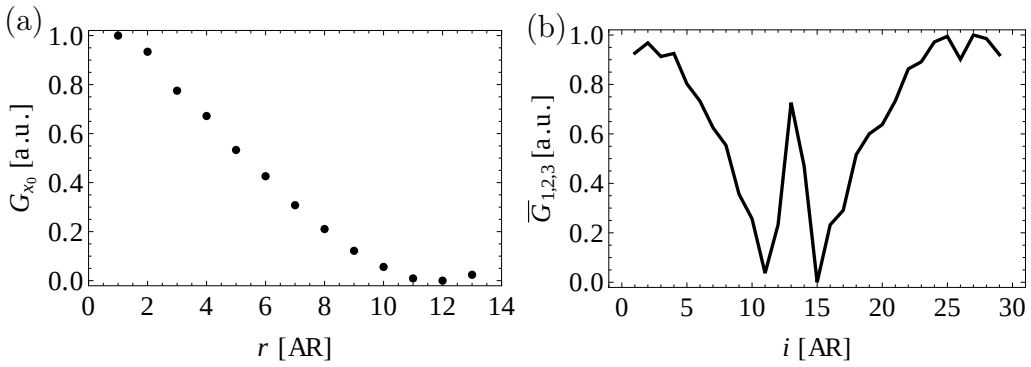

Figure 13: (a) shows the correlation function $G_{x_0}(r)$ as a function of the distance r and (b) shows the correlation function for each row with its neighboring rows i averaged for up to its third nearest neighboring rows. The tip is situated at the 13th atomic row.

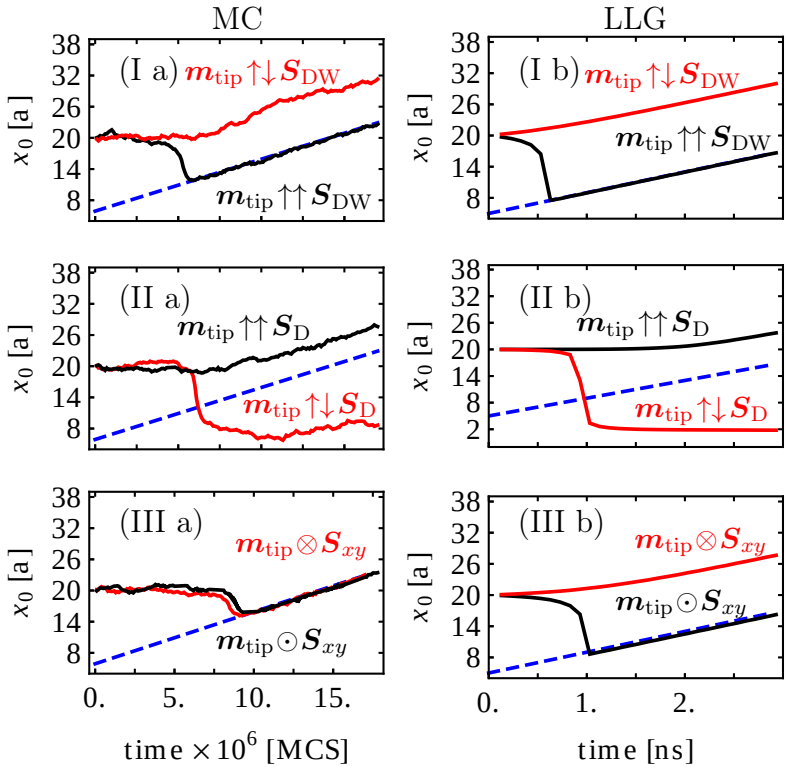

Figure 14: Domain wall position x_0 as a function of the time. Results of Monte Carlo simulations in the left column and of spin-dynamics in the right-hand column. The tip moves with constant velocity marked by the dashed line. (I a) and (I b) for a tip magnetization parallel and anti-parallel to the initial domain $\boldsymbol{S}_{\mathrm{D}}$, (II a) and (II b) parallel and anti-parallel to the domain wall orientation $\boldsymbol{S}_{\mathrm{DW}}$, and (III a) and (III b) pointing in- or out-of-plane. A 180° transverse domain wall has initially been placed at $x_0 = 20\ a$. The spin-dynamic calculations have been performed by Robert Wieser.

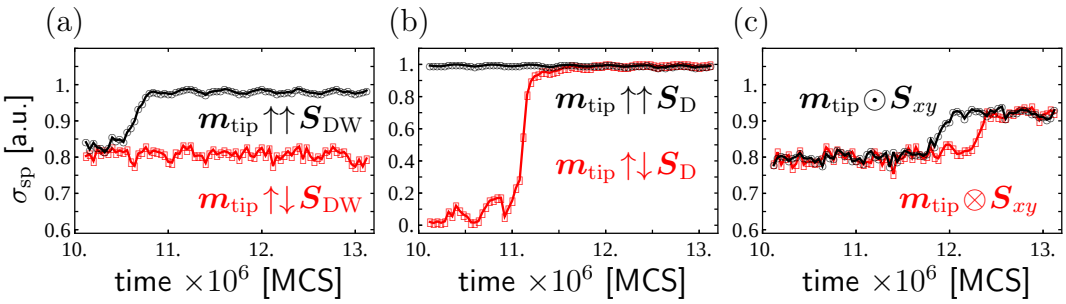

Figure 15: Spin dependent conductivity versus time for the different tip magnetizations of the three scenarios I-III. The red and black curves correspond to different tip magnetizations, as denoted by the insets. This figure has been published in a similar fashion in [30].

4 Manipulation of a domain wall in a ferromagnetic nanowire including magnetic defects

In the previous section a tunneling current has been utilized to manipulate a domain wall in a nanometer scale wire. A nanowire without edge or surface roughness, defects, or constrictions has been assumed. However, in experiments imperfections of samples become evident as defects in the material's crystal structure [73–76] and may impede the domain wall manipulation. In the cited publications different types of defects are described, namely planar defects, line defects, point defects, and atomic disorder. The current chapter presents a Monte Carlo study of the influence of *point defects* on the domain wall propagation and manipulation. A point defect is defined as the local change of the magnetic properties of the system. Furthermore, the study aims at resolving the Peierls potential from a domain wall manipulation.

The chapter starts with the definition of defects and the pinning of a domain wall at such defects. It follows the introduction into the properties of the system, the Monte Carlo simulation scheme and the definition of the defect distribution in the nanowire. Then results of the domain wall manipulation are presented and it will be shown, that the pressure created by the applied current oscillates as a function of the tip position. After this, the Peierls potential is estimated and the depinning fields for defects with different amplitudes of the defect anisotropy presented. At the end a method is proposed how the results of the simulation could be compared with future experiments.

4.1 Defects, pinning sites, and domain wall pinning

4.1.1 Definition of defects and pinning sites

A point defect changes locally the magnetic properties of the crystal, which leads to a local change of the Peierls potential. If such a perturbation of the Peierls potential leads to the pinning of a domain wall, it is referred to as *pinning site*. In previous theoretical and experimental investigations, defects have been described as changes of the anisotropy field [77–81], as changes of the exchange coupling [82], or as a change of the local stray field [83]. In the present work, point defects are defined as lattice sites with an altered magnitude of the easy-axis anisotropy.

In experiments on iron nanowires grown on a stepped tungsten substrate [35, 39], domain walls have been found to be strongly coupled to the step edges. As a

consequence of the coupling to the step edges, one can assume the atoms situated at the island's rim to possess different magnetic properties compared to the atoms at the surface or in the bulk. Furthermore, experiments of nanoislands on a flat substrate showed that atoms at the rim of the nanoislands (e.g., Fe/W(110) [84] or Co/Pt(111) [85]) exhibit a much larger anisotropy than atoms at the surface or in the bulk. The present study takes these experiments as guide and focuses on a defect scenario with defects situated at the rim of the nanowire. One could argue that this defect distribution rather corresponds to line defects, because the defects are lined up next to each other. However, since the obtained results are valid also for single point defects the defects are denoted as point defects, in this thesis. The discussion of defects and pinning sites in the following section is valid in general, hence, the results obtained in this work are also helpful to get an idea of the domain wall pinning at randomly distributed defects, kinks, or constrictions.

Depending on the purpose of the experimental investigation, pinning may be desired or not. Anyhow, in order to design a reliable magnetic storage or logic device exploiting domain walls, the effect of defects on the pinning of domain walls must be understood microscopically. This task requires an understanding of the energy landscape through which the domain wall moves, and has been described in the present work by a local change of the Peierls potential. The results will be presented in detail in section 4.2.2.

4.1.2 Definition of domain wall pinning at defects

In section 3.2 it has been shown, that a localized spin-current can reduce the pinning barrier of the domain wall and allow for the domain wall to move from one atomic row to the next. If structural defects are present in the crystal, they may impede the domain wall propagation. The authors of [70] mention, that "one says that the wall is pinned by defects when, under an external pressure, the wall does not move because of its coupling with defects of the crystal", and that "the potential imposed by the defects onto the wall is called *pinning potential*". They note, that one "introduces a notion of *pinning pressure* defined as external pressure needed to cause *depinning* — the macroscopic motion of the wall through the pinning potential". To stick to the nomenclature introduced in the previous chapter the pinning pressure will be denoted as depinning field f^* in the following.

Experiments revealed that defects cause areas with modified magnetic properties and can, for instance, be described by a change of the anisotropy constant

[77, 86]. In the present work, defects are treated as changes of the magnitude of the in-plane easy-axis anisotropy constant ($K_{[1\bar{1}0]}$), which is similar to former theoretical studies of systems with perpendicular anisotropy [79–81]. If the poten-

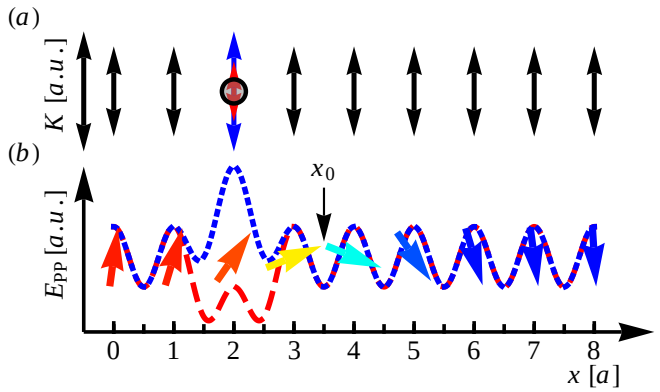

Figure 16: (a) shows schematically the magnitude of the anisotropy for different lattice sites. The anisotropy is constant for sites with a black arrow, and is varied during the simulation for the lattice site with the two colored arrows, representing the anisotropy of a defect (gray circle). The blue arrow indicates an increase of the anisotropy and the small red arrow a decrease of the anisotropy. In (b) the change of the Peierls potential due to the change of the anisotropy is illustrated, the red dashed curve for a decrease and the blue dotted line for an increase of the anisotropy.

tial landscape changes due to a defect of the lattice, the pinning barrier at that coordinate can either be increased or decreased. Figure 16 (a) schematically shows the magnitude of the anisotropy for different lattice sites with a single defect at $x = 2\ a$ and a domain wall at $x = 3.5\ a$. The gray circle indicates the lattice site of the defect with a modified anisotropy constant K (red and blue arrows), while the anisotropy remains unchanged ($K = K_0$) for all other lattice sites (black arrows). For a defect with decreased anisotropy (red dashed curve), the total energy can be minimized if the domain wall propagates towards the defect, as clear from Figure 16 (b). If the wall reaches that position, it gets pinned by the defect. On the contrary, for an increased anisotropy (blue dotted curve), the total energy would increase if the domain wall propagates towards the defect, hence, the domain wall avoids that position. The domain wall is not pinned, but the defect hinders the domain wall from propagating into the $-x$-direction.

If the domain wall is pinned, it can only get depinned when the pinning barrier is essentially reduced by applying an external pressure or by thermal excitations. However, an applied current sufficient to move a domain wall in a defect free wire,

as discussed in sections 3, might not be sufficient to manipulate a domain wall in a wire containing single or multiple defects. In order to check this statement, the same current as used in the previous chapter has been used for the simulations presented in the following.

4.2 The system properties and the simulation scheme

4.2.1 The system properties and the used Hamiltonian

The system properties and the simulation scheme is very similar to the study presented in the previous chapter (see section 3.1.5), only the anisotropy constant K_y has been changed at predefined lattice sites. The global anisotropy constant K_y is replaced by an anisotropy constant for each lattice site i, hence, the Hamiltonian reads:

$$\mathcal{H} = -J_{[001]} \sum_{\langle ij \rangle} \boldsymbol{S}_i \boldsymbol{S}_j - J_{[1\bar{1}1]} \sum_{\langle ij \rangle} \boldsymbol{S}_i \boldsymbol{S}_j - J_{[1\bar{1}0]} \sum_{\langle ij \rangle} \boldsymbol{S}_i \boldsymbol{S}_j - \sum_i K_y^i (S_y^i)^2 + K_z \sum_i (S_z^i)^2, \tag{37}$$

where $J_{[hkl]} > 0$ denotes the effective nearest neighbor exchange coupling constant along different crystallographic directions. $K_y^i > 0$ is an easy-axis anisotropy at site i pointing in-plane, and $K_z > 0$ an out-of-plane hard-axis anisotropy. The first three sums run over all nearest neighbors along a certain crystallographic direction and the last two sums run over all lattice sites i. The exact values of each K_y^i are defined in the next section. As the study presented in the previous chapter revealed the tip magnetization with an orientation parallel to the domain wall orientation being the most promising for successful domain wall manipulation, the defect study has been performed for that tip magnetization only.

The Monte Carlo simulations have been repeated with the magnitude of the defect anisotropy being varied systematically. In the following, the index y will be omitted because only the easy-axis anisotropy (pointing along $y \equiv [1\bar{1}0]$]) has been changed in the simulation. The magnitude of the anisotropy constant K has been chosen in a range of $\{0.1, ..., 10\}$ K_0 in steps of 0.1 K_0. K_0 denotes the magnitude of the anisotropy of all non-defects sites (see Table 1). Hence, two regions can be identified, one with reduced anisotropy ($K < K_0$) and one with enhanced anisotropy ($K > K_0$). Even though it is known that the anisotropy at the rim of the island is higher than the anisotropy of the surface atoms [84, 85], simu-

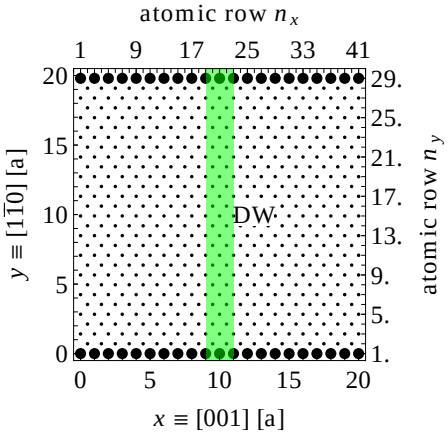

Figure 17: Illustration of the nanowire with an altered magnitude of the anisotropy at two edges, which could represent a nanowire grown on a terrace between two step edges. The large circles correspond to sites with a changed anisotropy K and the small circles correspond to lattice sites with an unchanged anisotropy K_0. The green rectangle illustrates the position and elongation of the domain wall.

lations have also been performed for reduced edge anisotropies, to complete the theoretical picture. In order to map the Peierls potential as precisely as possible, all simulations have been repeated for about 50 different random seeds. Hence, a manipulation trial has been repeated 50 times for each anisotropy value. In order to reduce the simulation time smaller systems than presented in the previous chapters have been simulated ($N_x \times N_y \approx 40 \times 30$ AR), which can be considered as a segment of the wire of chapter 3, depicted in Figure 17. The size of the circles in Figure 17 illustrates the magnitude of the anisotropy for each lattice site: the larger circles correspond to defects with a modified magnitude K, and the small circles correspond to lattice sites with a regular anisotropy K_0.

4.2.2 The Peierls potential of a lattice with magnetic defects

If the domain wall is pinned in the wire, the depinning field depends on both: on the number of defects involved in the pinning and on the change of the anisotropy per defect. The defect anisotropy defines the change of the local energy at site i with respect to a lattice site without defect. In the simulations, the anisotropy constant K of the defects has been increased systematically, which led to a perturbation of the sinusoidal potential of the ideal lattice, as shown in Figure 16. Adding a perturbation term $E_{\text{pert}}(x) = \Delta K F(x)$ to equation (33) one derives (in one-

dimension) the spatial dependence of the perturbed energy landscape $E_{\mathrm{PP}}(x)$:

$$E_{\mathrm{PP}}(x) = E_{\mathrm{PN}} \sin^2(\frac{2\pi x}{d}) + \Delta K F(x) = E_{\mathrm{P}}(x) + E_{\mathrm{pert}}(x). \tag{38}$$

In two-dimensions the perturbed energy term $E_{\mathrm{pert}}(x, y)$ at each lattice site has been defined by a defect distribution function $F(x, y)$, which represents the spatial distribution of the defects. The following defect distribution function places the defects at the edges of the wire:

$$F_{\mathrm{ED}}(x, y) = \begin{cases} 1, & \text{if } \ y \in \{1, N_y\} \\ 0, & \text{else} \end{cases} , \tag{39}$$

where ED stands for **E**dge **D**efects. For each defect present in the system, the pinning barrier decreases or increases corresponding to the anisotropy change $\Delta K = K - K_0$. Figure 17 illustrates the studied defect configuration. A domain wall propagating through the nanowire with defects experiences a different potential landscape compared to the defect free wire. In two dimensions, the spatial dependence of the domain wall energy is described according to equation (35):

$$E^f_{\mathrm{PP}}(x, y) = S_0(E_{\mathrm{PP}}(x, y) - f(x, y)). \tag{40}$$

A one-dimensional approximation of the spatial dependence of the domain wall energy is given by summing up $E^f_{\mathrm{PP}}(x, y)$ for each atomic row along y ($E^f_{\mathrm{PP}_y}(x) = \sum_{i=1}^{i=N_y} E^f_{\mathrm{PP}_i}(x)$) and is illustrated by Figure 18.

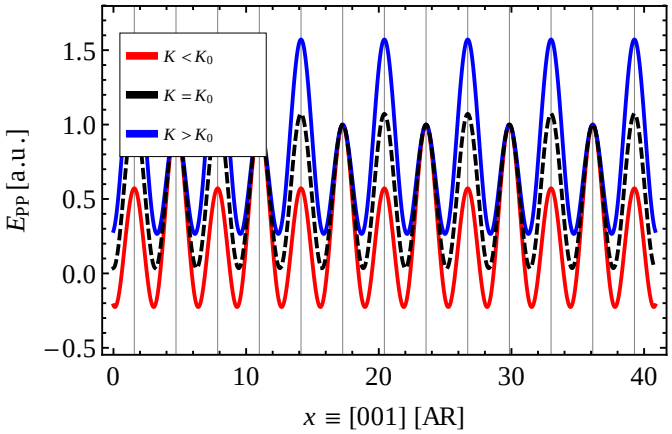

Figure 18: Illustration of the Peierls potential for three different defect anisotropies. The black dashed curve corresponds to the defect free wire, the red curve corresponds to the energy for defects with an enhanced anisotropy ($K > K_0$) and the blue curve corresponds to the energy for defects with reduced anisotropy ($K < K_0$).

Looking at the perturbed potential shown in Figure 18 an asymmetry of the amplitude between odd and even atomic rows is striking, especially for the wire including defects (red and blue curves). This asymmetry is a finite size effect and is due to the BCC lattice structure of the wire. The rows with an odd number along x hold one more lattice site and two defects, the even rows on the contrary do not include any defects. The presence of defects increases this finite size effect, but it is already visible for the defect free wire, as shown by the black dashed curve in Figure 18.

How the perturbed potentials influence the domain wall propagation will be presented in the following sections.

4.3 Domain wall manipulation

Figure 19 (a) shows manipulation curves for different anisotropy values. In the case of a successful manipulation the curves run parallel to the purple dashed line, which indicates the tip position. The manipulation curves end up at $x_0 = 41$ AR, which means the domain wall has been manipulated successfully until the end of the nanowire. Looking at the manipulation curves for larger values of the defect anisotropy (blue curve) a periodic, stepwise modulation of the curve is visible. This stepwise propagation of the domain wall is a result of an oscillating external pressure, which only appears for $K > K_0$ and will be addressed in detail in the next section. In the case of an unsuccessful manipulation the curves drop down to an arbitrary value below $x_0 = 41$ AR (green curves), meaning that the domain wall has been manipulated partially, or, in the case of the green dashed curve displayed, not at all.

Whether a domain wall has been manipulated successfully for a certain defect anisotropy can easily be read from the final magnetization M_y^{fin}, shown in Figure 19 (b). It is equal to unity for successful manipulation and smaller for unsuccessful manipulation. M_y^{fin} clearly shows that the domain wall can be manipulated successfully for defect anisotropies up to $K = 2.5\ K_0$, hence, the probability of a successful manipulation P_{manip} is equal to one. $P_{\text{manip}} = 1$ means that the external pressure f has been larger or equal to the depinning field f^*. Furthermore, M_y^{fin} shows that a partial manipulation occurs for anisotropy values in the range of $2.5\ K_0 < K < 3.2\ K_0$ (red shaded area) and that for $K > 3.2\ K_0$ no manipulation is possible at all. Hence, the probability of a successful manipulation decreases for $K > 2.5\ K_0$ and vanishes above $K = 3.2\ K_0$.

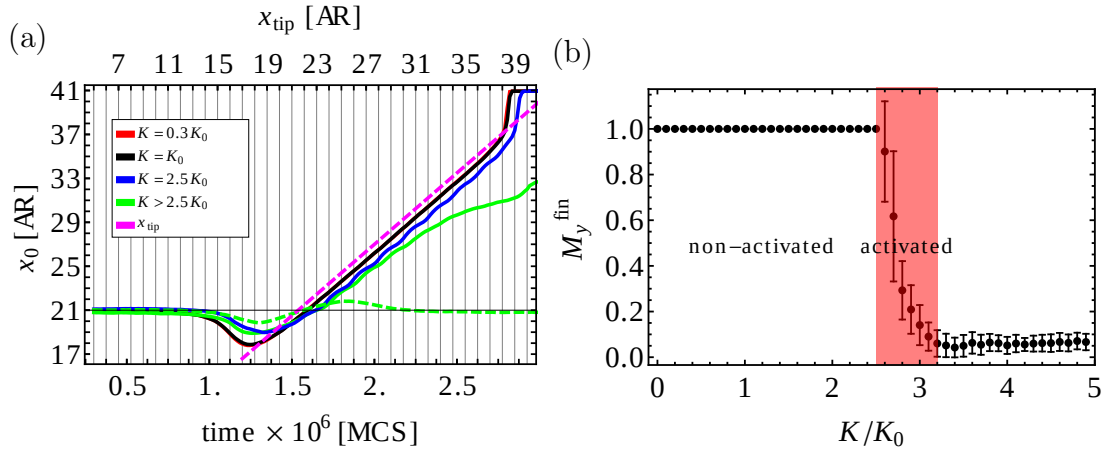

Figure 19: (a) shows manipulation curves for different anisotropy values. The purple dashed line in (a) gives the tip position over time and the vertical lines correspond to the tip position in units of an atomic row. (b) shows the averaged final net magnetization M_y^{fin} after a domain wall manipulation trial for different anisotropies. The red shaded area indicates the activated regime.

From Figure 19 (b) one can identify the two regions mentioned in section 3.2: the non-activated and the activated region. For anisotropies up to $K = 2.5\ K_0$ the final magnetization is equal to one with a vanishing standard deviation indicating that no thermal excitation is needed for the domain wall to overcome the pinning barrier, hence, the manipulations have taken place in the non-activated regime.

The increase of the standard deviation above $K = 2.5\ K_0$ means that only with the help of thermal energy the domain wall can be manipulated, thus, the depinning field exceeds the external pressure. This narrow anisotropy region of $2.5\ K_0 < K < 3.2\ K_0$ corresponds to the activated regime. In the activated regime the so-called escape time τ the system needs to overcome the pinning barrier follows the Boltzmann statistics:

$$\tau = \tau_0 \exp[\frac{\Delta E}{k_{\mathrm{B}} T}], \tag{41}$$

where ΔE is the energy barrier to be overcome by the thermal energy and corresponds to the Peierls-Nabarro barrier reduced by the external pressure, and τ_0 is a prefactor. Due to the periodicity of the defect distribution along the direction of the domain wall propagation (x) the domain wall has to overcome the pinning barrier repeatedly during a manipulation trial. Since the temperature, the number of atomic rows, and also the applied current has been held constant during the simulations the probability of a successful domain wall manipulation in the

activated regime decreases exponentially with increasing pinning barrier:

$$P_{\text{active}} \propto \exp[-\frac{E_{\text{PN}} N_x}{2 k_{\text{B}} T}]. \tag{42}$$

Equation (42) is in agreement with the strong decrease of M_y^{fin} above $K = 2.5\ K_0$ in Figure 19 (b). From the findings presented one can conclude that for a defect anisotropy larger than $K = 2.5\ K_0$ the depinning field f^* exceeds the external pressure f; i.e., $f < f^*$ for $K > 2.5\ K_0$.

Before the pinning barrier and the depinning fields are determined as a function of the defect anisotropy the following section will shed some light on the stepwise behavior of the manipulation curve in Figure 19 (a) (blue curve).

4.4 Oscillation of the external pressure

In section 3.3.1 it has been discussed that the applied current does not directly reduce the pinning barrier for the whole domain wall. It only causes a displacement of the part of the domain wall directly underneath the tip. The displacement of this first segment leads to an increase of the internal field, which in turn leads to the subsequent propagation of the segments of the domain wall that are situated farther away. In the study presented in chapter 3 the external pressure did successfully reduce the pinning field at all times (for each tip-step). As a result, the domain wall followed the tip at a constant distance leading to a smooth manipulation curve (see black curve in Figure 10 (a) and Figure 19 (a)). However, the dynamics of the domain wall propagation becomes more complicated for larger pinning barriers (see blue curve in Figure 19 (a)), as will be discussed in the following.

Figure 20 (a) shows the mean tip-wall distance during manipulation as a function of the anisotropy value K. For anisotropy values $K \lesssim K_0$ the domain wall follows the tip at a distance of about $\langle r_{\text{tw}} \rangle = 0.4\ a$, but the tip-wall distance increases for $K > K_0$ until the domain wall cannot be manipulated anymore above $K = 2.5\ K_0$. An analysis of the time resolved domain wall dynamics revealed that with increasing depinning field, on the one hand, the tip moves further in front of the domain wall and, on the other hand, the bending of the domain wall increases. Both these factors lead to an increase of the effective internal field, which can be seen as an increase of the external pressure. Hence, the increasing tip-wall distance reflects an increase of the external pressure f.

When looking at the time resolved tip-wall distance one finds an oscillating behavior for anisotropies larger than $K = K_0$, shown in Figure 20 (b). Note, that each data point of Figure 20 (a) corresponds to the time average of a curve in the manipulation regime of Figure 20 (b). For anisotropies larger than K_0 the external

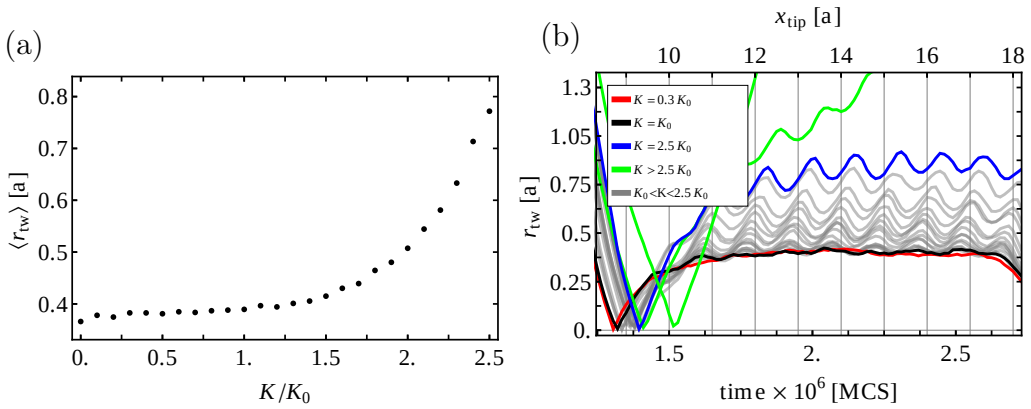

Figure 20: (a) shows the tip-wall distance $\langle r_{\mathrm{tw}} \rangle$ averaged over the whole manipulation process after the tip-wall contact has been achieved. (b) gives the distance r_{tw} between tip and wall as a function of time for different anisotropy values. The data points in (b) corresponds to an average of the curves in (a) for the interval between the tip positions 11 a and 18 a.

pressure at $r_{\mathrm{tw}} \approx 0.4\ a$ is not sufficient any more to depin the domain wall. From now on the domain wall dynamics drastically change. In order to overcome the pinning field and to depin the domain wall the tip has to move further. Hence, the external pressure at $\langle r_{\mathrm{tw}} \rangle = 0.4\ a$ only leads to a partial propagation of the domain wall segments close to the tip, while the segments at the edges are (temporarily) pinned. Then the tip moves another tip-step and the segments close to the tip path follow again, which increases the external pressure. As long as the coupling between the tip and the domain wall is strong enough, the external pressure increases further each tip-step, but does not necessarily depin the whole domain wall. For each further tip-step, the bending of the domain wall increases until finally the depinning field is reached and also the domain wall segments at the edges can overcome the pinning barrier. After the successful depinning of the domain wall the domain wall propagates towards the tip to the next pinning site. As a result the external pressure decreases again. The described dynamics become evident in the time dependence of the tip-wall distance in Figure 20 (b). The alternation between stepwise increasing external pressure and the subsequent propagation of the domain wall leads to the oscillatory development of the tip-wall distance r_{tw} and manifests itself in the step by step propagation of the domain wall. The tip-

wall distance curves are smooth for $K \leq K_0$ (red and black curves) but show the oscillatory behavior for $K_0 < K < 2.5\ K_0$ (gray curves), which becomes more and more pronounced for increasing K and gets maximal for $K = 2.5\ K_0$ (blue curve).

In fact, the oscillation of the tip-wall distance shown in Figure 20 (b) occurs for any strength of the defect anisotropy but becomes pronounced only for larger anisotropies. This statement has been confirmed by a Fourier analysis. The amplitude of the Fourier signal calculated on the basis of Figure 20 (b) shows two peaks. The peak positions do not change for $0 < K < 2.5\ K_0$ and lie at the wave vector of about $0.1\ \frac{1}{\Delta x_{\mathrm{tip}}}$. Hence, the Fourier analysis reveals a periodicity of about one lattice constant, which means that during a manipulation trial the external pressure reaches a maximum after every tip displacement of one lattice constant. As long as the depinning field is smaller than the maximal external pressure the domain wall follows the tip and is successfully manipulated.

As will be shown in the following section, it is the oscillation of the external pressure which allows to estimate the energy landscape through which the domain wall propagates. If a constant and homogenous external magnetic field would have been applied, a sweep of the field would have been necessary in order to determine the depinning field for different anisotropy values.

4.5 Determining the depinning field

4.5.1 Mapping the Peierls potential

The domain wall manipulation for anisotropies smaller than $K = 2.5\ K_0$ has taken place in the non-activated regime. In this regime, the external pressure reduces the pinning barrier and the domain wall propagates from one potential valley to the next without thermal assistance needed. As discussed in the previous section, the oscillation of the external pressure leads to a stepwise domain wall propagation. This stepwise propagation allows to map the different energy states the domain wall passes through. By plotting the total energy as a function of the domain wall position x_0, one obtains a one-dimensional estimate of the energy landscape through which the domain wall propagates: i.e., the Peierls potential.

Figure 21 (a) shows the total energy as a function of the domain wall position for a defect anisotropy of $K = 2.5\ K_0$. The energy obviously oscillates periodically during manipulation, as predicted by equation (38). The amplitude of the energy oscillation corresponds to the Peierls-Nabarro barrier E_{PN} of the perturbed potential in equation (38) and is shown in Figure 21 (b) as a function of the de-

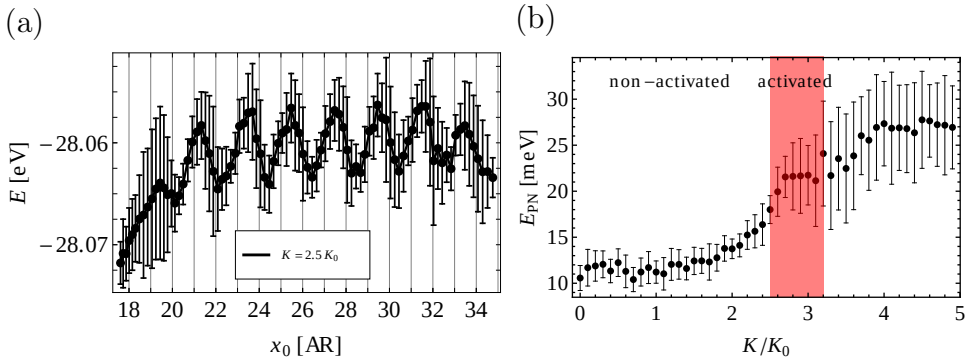

Figure 21: (a) shows the total energy as a function of the time during a manipulation trial for a defect anisotropy of $K = 2.5\ K_0$. During domain wall manipulation the energy increases and decreases according to the position of the domain wall. The vertical lines indicate the estimated positions of the atomic rows. (b) shows the estimates of the pinning barrier E_{PN} of the perturbed potential. E_{PN} has been determined via the maximum and minimum of the total energy during manipulation, hence, $E_{\mathrm{PN}} = E_{\mathrm{max}} - E_{\mathrm{min}}$. The red shaded area indicates the activated regime.

fect anisotropy. E_{PN} corresponds to the pinning barrier to be overcome by the external pressure. For defect anisotropies up to $K = K_0$ the energy curves found are flat resulting in a constant E_{PN} of about 11 meV. Hence, the external pressure has reduced the pinning barrier at all times. Additional analysis of simulations without current applied resulted in an E_{PN} of 11 ± 0.4 meV. Hence, the minimal determined Peierls-Nabarro barrier of 11 meV in Figure 21 (b) can be attributed to thermal fluctuations.

Above $K = K_0$ the Peierls-Nabarro barrier increases with increasing defect anisotropy until it reaches a maximum in the activated regime. Without the assistance of thermal energy but under the influence of an external pressure the domain wall can overcome a maximal pinning barrier of $E_{\mathrm{PN}} = 18 \pm 1.5$ meV at $K = 2.5\ K_0$. Even if locally (underneath the tip) much more energy is pumped into the system (about 100 meV as mentioned in section 3.1.5), it is only a maximal energy of about 18 meV that is transferred into the kinetic energy of the domain wall.

From Figure 21 (a) one would assume a Peierls potential of a simple sinusoidal periodicity with a period of one lattice constant. But the periodicity of the finite BCC lattice along [001] is rather described by a wave vector of $0.5\ \frac{1}{a}$, as clear from Figure 18. This discrepancy can be explained by the minimal energy pumped into the system. In combination with the thermal energy the external pressure always reduces the pinning barrier of the even rows, because they do not hold any defects. Thus, the domain wall can only get pinned at the odd rows and only if the defects

create a pinning barrier larger than 11 meV. As a result, the energy landscape can only be resolved if $E_{\mathrm{PN}} > 11$ meV, because the domain wall needs to get temporarily pinned in order to map the different energy states. That explains the periodicity of one lattice constant, as the domain wall propagates directly after the depinning to the next pinning site (the next odd row) jumping over the following even row. The difficulty of measuring the Peierls potential, especially in a sample with defects, has been mentioned by Novoselov in his Ph. D. thesis [72]. He writes that the Peierls potential

"[...] has never been directly observed before for ferromagnetic domain walls. One of the reasons is that the strength depends exponentially on the domain wall width, and the Peierls potential quickly becomes buried under thermal fluctuations as the thickness of the domain increases. Moreover, pinning on pinning centers is usually much stronger than intrinsic pinning, which makes the detection of the latter even harder".

If the external pressure is always larger than the depinning field ($K \lesssim K_0$), the domain wall reaches a spin configuration with the minimal energy at each tip-step. Hence, the total energy of the sample during manipulation stays constant and is defined by the thermal energy. Only when the depinning field exceeds the minimal external pressure (for larger defect anisotropies) the defect distribution can be observed.

4.5.2 Estimating the external pressure

By differentiating the total energy (Figure 21 (a)) as a function of the domain wall position one derives an estimate of the spatial dependence of the external pressure. Figure 22 (a) shows the first derivative of the averaged energy landscape during manipulation as a function of the domain wall position x_0, which corresponds to the effective internal field acting on the domain wall. For a successful domain wall manipulation the maximal steepness of the potential, hence, the depinning field f^* has to be overcome. The maximum external pressure acting on the domain wall during propagation corresponds to the depinning field for a certain K. Note, that Figure 22 (a) shows the external pressure averaged over all random seeds, while the depinning field f^* has been calculated from each single manipulation trial and then averaged. Figure 22 (b) shows f^* as a function of the defect anisotropy K. In

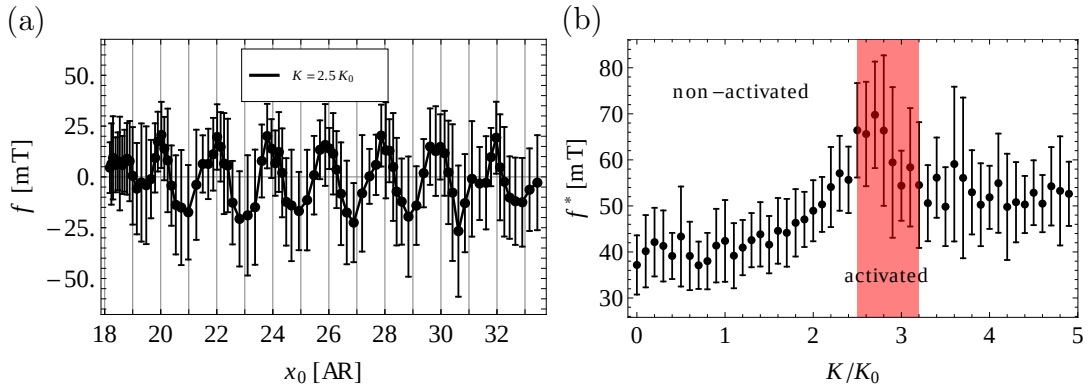

Figure 22: (a) shows the derivative of Figure 21 (a). The spatial dependence of the derivative of the total energy corresponds to the spatial dependence of the external pressure, hence, $f = -\partial\mathcal{H}/\partial x$. The vertical lines indicate the estimated positions of the atomic rows. (b) shows the averaged maximum external pressure f^* as a function of the defect anisotropy. The red shaded area indicates the activated regime.

the non-activated regime the maximum external pressure leading to a successful manipulation is $f^* = 66 \pm 10$ mT for a defect anisotropy of $K = 2.5\ K_0$. Hence, the overall maximal external pressure which has been created by the applied spin current is $f^* = 66$ mT. Again, the maximum of f^* lies in the activated regime, which is due to the thermal assistance. Unfortunately, a functional dependence cannot be determined from the numerical data.

The next section introduces an analysis which could allow the comparison between data from simulation and data from experiment.

4.6 Estimating the Peierls potential in experiment

In the previous section the Peierls potential and the depinning field has been estimated by analyzing the total energy of the system, which is unfortunately not directly accessible in experiments. The determination of the depinning field is for instance possible in Hall micromagnetometry [87] experiments, but this technique requires a sufficient stray field, which is not applicable for systems with small stray fields like the nanowires with in-plane anisotropy presented in this work. A different experimental technique, introduced by Nguyen *et al.* [88], allows to determine the depinning field of ferromagnetic domain walls in nanowires with in-plane magnetization by measuring the magnon contribution to the resistivity. However, to determine the Peierls potential in experiment one has to get access to the domain wall dynamics, hence, analyzing the domain wall position as a function of time, which is not possible by the experimental methods mentioned. The domain

wall position as a function of time can be determined, e.g., in magneto-optic Kerr effect (MOKE) or anisotropic magnetoresistance (AMR) measurements, but is usually used for much larger samples and may not be applicable for small domain walls as studied in this thesis. In the following, an analysis of the simulated data is presented, which might be applicable to experimental data.

4.6.1 Time resolved domain wall velocity

As the shape of the Peierls potential influences the domain wall propagation, the velocity of the propagating domain wall V_{DW} changes in dependence of the potential through which the domain wall passes during manipulation. The domain wall velocity can be extracted from the derivation $V_{\mathrm{DW}} = \frac{\mathrm{d}x_0}{\mathrm{d}t}$ of the manipulation curves (e.g., shown in Figure 19). Figure 23 shows the domain wall velocity

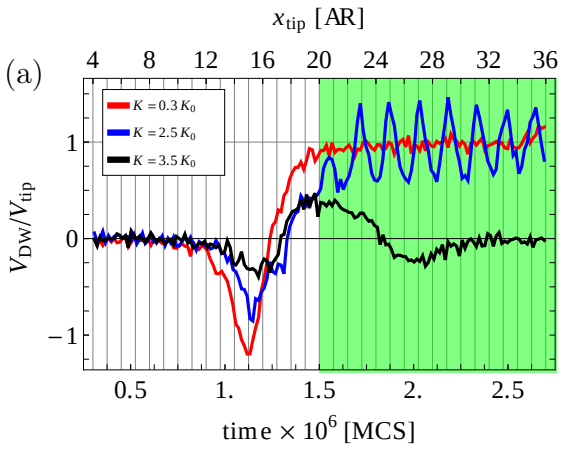

Figure 23: Domain wall velocity $V_{\mathrm{DW}}/V_{\mathrm{tip}}$ as a function of time and the tip position x_{tip} for three different anisotropy values. The vertical lines correspond to tip positions in distances of one atomic row. Note, that the error bars have been omitted in this plot for clarity.

for a reduced (red) and enhanced (blue and black) anisotropies compared to the anisotropy K_0 of the defect free system. A domain wall, in contact with the tip, can be manipulated only with the same velocity as the tip velocity V_{tip}, otherwise the tip-wall contact collapses. This statement becomes clear when looking at the time averaged mean domain wall velocity $\langle V_{\mathrm{DW}} \rangle$ shown in Figure 24 (a): it is close to V_{tip} until the domain wall cannot successfully be manipulated anymore above $K = 2.5\ K_0$.

The curve shown in Figure 24 (a) looks very similar to the final magnetization plotted in Figure 19 (b) and does not give more information about the properties

of the depinning field. Like in the analysis of the Peierls-Nabarro barrier, one can conclude that above a magnitude of the defect anisotropy of $K = 2.5\ K_0$ the pinning barrier cannot be overcome anymore, hence, the depinning field exceeds the external pressure for $K > K_0$. The mean domain wall velocity does not reflect any change of the depinning field as a function of the defect anisotropy K. However, as clear from Figure 23, the external pressure has a great impact on the fluctuation of the domain wall velocity around its mean value during a manipulation trial. After the tip-wall contact has been achieved (after about 20 atomic rows, green region in Figure 23) the velocity ratio $V_{\mathrm{DW}}/V_{\mathrm{tip}}$ fluctuates around the tip velocity. The domain wall gets bent and strained during the domain wall propagation due to the interaction with defects. A large variation of the domain wall velocity occurs in three cases: at the first tip-wall contact, when the tip-wall contact is lost, and if defects impede the domain wall propagation.

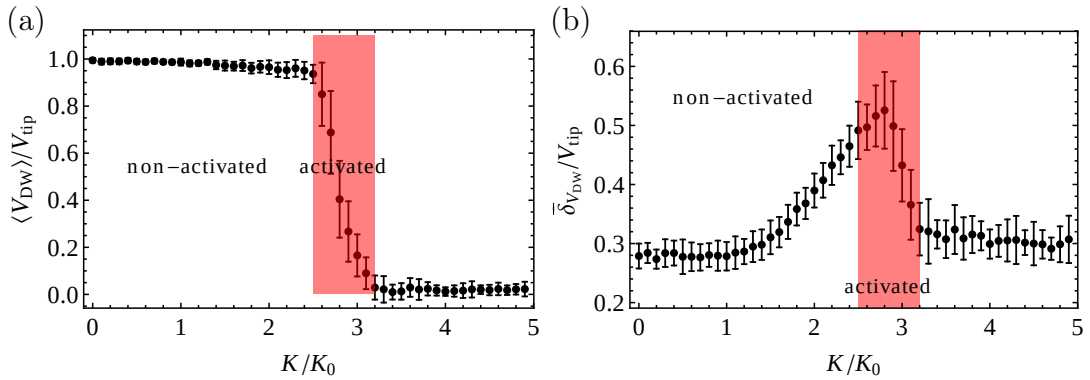

Figure 24: (a) shows the normalized averaged domain wall velocity $\langle V_{\mathrm{DW}}\rangle/V_{\mathrm{tip}}$. The velocity is normalized by the velocity of the tip V_{tip}. Each data point corresponds to the average of the time resolved domain wall velocity during manipulation, as shown in Figure 23. (b) gives the standard deviation of each time averaged value in (a). Hence, these data correspond to the fluctuation of the domain wall velocity during manipulation. The red shaded areas in (a) and (b) indicate the activated regime.

Hence, the variance of the time resolved domain wall velocity $\delta_{V_{\mathrm{DW}}}$ during manipulation is directly connected with the strength of the depinning field. Figure 24 (b) shows $\delta_{V_{\mathrm{DW}}}$ as a function of the defect anisotropy. Until $K \approx K_0$ the pinning barrier is reduced by the external pressure at all times, leading to a constant variance in the range of the thermal fluctuations. Above $K = K_0$ the variance increases linearly until a defect anisotropy of $K = 2.5\ K_0$ is reached. Above $K = 2.5\ K_0$ the increase slows down and reaches its maximum in the activated regime, which is caused by the assistance of the thermal energy. With further increasing depinning field the variance decreases again until it reaches its

minimum above $K = 3.2\ K_0$. The overall minimal variance of about $0.3\ V_{\text{tip}}$ is in accordance with the variance determined for a simulation without current applied. Hence, the offset before $K = K_0$ and above $K = 3.2\ K_0$ is attributed to thermal fluctuations.

Just as from the time resolved total energy shown in the previous section, one can resolve an estimate of the defect distribution from the time resolved domain wall velocity, as shown by Figure 23. Furthermore, the observed dependence of the domain wall velocity variance on the defect anisotropy is in agreement, both, with the dependence of the Peierls-Nabarro barrier (Figure 21 (b)) and the depinning field (Figure 22 (b)) on the defect anisotropy. Hence, the analysis of the domain wall velocity gives an easy way to determine the periodicity of the defect distribution and the Peierls potential, and to estimate at which defect anisotropy the depinning field cannot be overcome anymore. If one could measure the domain wall position as a function of time in experiments, one could compare theory with experiment.

4.7 Summary and Conclusion

The manipulation of a narrow domain wall in a ferromagnetic nanowire including point defects by means of a localized spin-current has been studied theoretically. The point defects have been described as sites with a deviating easy-axis anisotropy. The Monte Carlo simulation showed that the defects affect the domain wall propagation and that already a few defects can easily lead to the pinning of a domain wall. Two defects situated at the edges of the wire, with a magnitude of the easy-axis anisotropy 2.5 times larger compared to non-defect sites ($K \geq 2.5\ K_0$), made a successful domain wall manipulation impossible for the same current applied as in the study presented in the previous chapter. This result points out, why it may be difficult to manipulate a domain wall in STM experiments. Because it is known that for well studied systems, like monolayer Fe/W(110) nanoislands and nanowires, the magnetic anisotropy of atoms situated at the rim is much larger compared to the surface atoms [84] ($K \approx 10\ K_0$). In experiments one can also assume that the coupling of nanowires to step edges, or the occurrence of edge roughness or constrictions due to the preparation process, will further increase the depinning fields. These factors could make it a difficult task to realize the controlled domain wall manipulation using the spin-current of an STM.

Surprisingly, the simulation showed that in an STM experiment a measurement

at one single bias voltage would be sufficient to estimate the depinning fields for a range of different defect anisotropies. The reason for this finding is the oscillation of the external pressure, which is caused by a repeated pinning and depinning of the domain wall on defects. This process is very similar to the single-atom manipulation recently published in [89]. Hence, the external pressure induced by the moving STM tip has not been constant during manipulation, it varied between about 40 mT and 66 mT. Usually [90, 91] an external magnetic field or the spin-current must be varied in order to determine the depinning field of a domain wall.

Moreover, it is the oscillating external pressure, which permits to estimate the distribution of the defects in the nanowire. From the analysis of the time-resolved total energy and also from the analysis of the domain wall velocity the periodicity of the defect distribution has been revealed and agreed with the prepared defect distribution. But, due to the too large applied current and the BCC lattice structure the exact shape of the Peierls potential could not be resolved. Because of the BCC lattice structure and the presence of defects, the domain wall has been pinned only every second atomic row. Therefore, the estimated Peierls potential revealed a periodicity with a wave vector half of the wave vector expected for the discrete lattice, which corresponded to the defect distribution.

5 Superparamagnetic boundaries of ferromagnetic nanoparticles

The recent advances in controlling and measuring magnetic properties of nanoparticles [84] as well as applications for magnetic data storage technology [7] rely on the fact that information, i.e., the magnetic state of a finite, small area representing a single bit, is stable over a finite observation time. However, as real magnetic samples have a finite size, and magnetic properties are measured during a finite observation time, thermal excitations enhance the magnetization switching, and, therefore, decrease the lifetime of the ferromagnetic states. This so-called *superparamagnetic* behavior increases with decreasing system size [8–10]. The simulations presented in the previous chapter have been performed at temperatures far below the Curie temperature T_c of the system, thus, the magnetic sample has been in a thermally stable ferromagnetic state and in order to switch the magnetization of the sample a spin current has been applied. In the present chapter a study of the so-called *critical temperatures* of a finite system is presented, without any external forces applied. These critical temperatures assign the boundaries of the superparamagnetic region, hence, they define the temperatures at which the system turns from one magnetic state (i.e., the ferro-, superpara-, or paramagnetic state) into another. As the superparamagnetism becomes a limiting factor for magnetic storage devices with ever decreasing bit sizes it is important to know the exact superparamagnetic properties of potential materials of future storage devices.

The material presented in this chapter has been originally published in *European Physical Journal B*: E. Y. Vedmedenko, N. Mikuszeit, T. Stapelfeldt, R. Wieser, M. Potthoff, A. I. Lichtenstein and R. Wiesendanger, *Spin-spin correlations in ferromagnetic nanosystems*, Eur. Phys. J. B, 80, 331-336 (2011) [92]. With kind permission of The European Physical Journal (EPJ). Note, that my contribution to the simulated results are restricted to the Monte Carlo simulations.

In the following a study of the spin-spin correlation function for anisotropic classical spin models in different dimensions with a finite and, in a thermodynamic meaning, small number of microspins is presented. It starts with an introduction of the simulated system and the applied Monte Carlo simulation scheme, followed by the definition of the critical temperatures, which define the superparamagnetic

region. As the magnetic order of ensembles of spins can be defined by a correlation function, here, a new method of determination of the upper as well as the lower limit of the superparamagnetic region is introduced. This new method is briefly discussed in the context of well established theoretical methods, namely, exact-diagonalization and static mean-field theory, before results of the Monte Carlo simulations are presented.

5.1 The system properties and the simulation scheme

5.1.1 The system properties and its Hamiltonian

The Monte Carlo simulations have been performed for the Ising and the classical Heisenberg model with nearest neighbor exchange and an uni-axial magnetic anisotropy K:

$$\mathcal{H} = -J \sum_{\langle ij \rangle} \boldsymbol{S}_i \boldsymbol{S}_j - K \sum_i (S_i^\alpha)^2. \tag{43}$$

For the Ising model the anisotropy part of this Hamiltonian vanishes, as the magnetic moments $\boldsymbol{S}_i$ can align along the easy-axis ($\alpha = x, y,$ or z) only. The calculation of the Heisenberg system has been performed for an easy-axis anisotropy of $K = 0.6\ J$, as defined by the parameter set SET3 in Table 1. Figure 25 illustrates the lattice used and the exchange bonds considered.

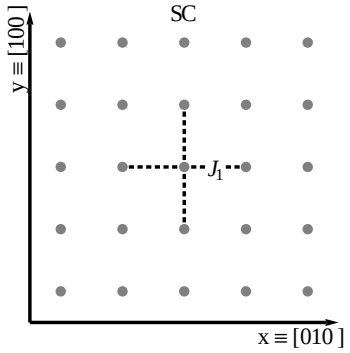

Figure 25: Sketch of the exchange bonds considered in the simulations for the two-dimensional square lattice.

5.1.2 The geometry of the nanoislands

Due to the long range character of the correlation function and the fact that the simulation has been carried out for a range of 200 different temperatures and

15 different system sizes, this study has been of great computational effort. To reduce the calculation times, the Monte Carlo simulations have been performed for a square lattice and for first nearest neighbors only. Figure 26 illustrates the shape of the simulated nanoislands. The dimension N of the squared islands has been varied from 5×5 AR up to 20×20 AR.

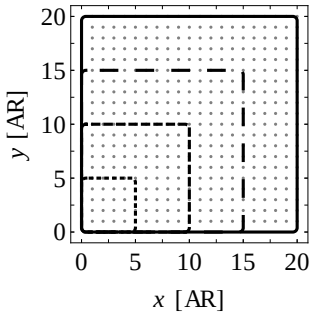

Figure 26: Sketch of the squared nanoislands used for simulations. The system size is increased successively, starting with a dimension of 5×5 AR up to a maximal island size of 20×20 AR.

5.1.3 The scheme of the Monte Carlo simulation

The system has been slowly annealed using the last spin-configuration of the previous temperature step as the initial spin-configuration for the next lower temperature. By choosing the temperature steps sufficiently small, it has been assured that the system is always in thermal equilibrium. For each temperature step and each system size, up to 10^7 MCSs have been performed and the specific heat C, the susceptibility χ, and the spin-spin correlation function $G(r)$ determined.

For this simulation neither a predefined configuration has been used nor an external pressure applied. To assure reliable statistics, the simulation of each temperature step has been repeated five times for different seeds of the random number generator.

The next section gives a general discussion of the critical temperatures in nanosized systems.

5.2 The reduced Curie temperature $T_c(L)$

The theory of collective magnetic order is usually concerned with infinite systems [26, 93–95]. For the sake of comparison with experimental data the present calculations are concentrated on magnetic islands of finite extensions. The Curie

temperature of a ferromagnetic sample is a well established concept that must be reconsidered for nanosized objects. From the experimental point of view, T_c is a well-defined quantity, which can be measured, e.g., as a function of the size L of the nanoparticle [8, 18]. The magnetic susceptibility and the specific heat stay finite but show enhancements at $T = T_c(L)$, which defines a Curie temperature up to some residual arbitrariness. From the theoretical point of view, there is no Curie temperature as there is no phase transition, and actually not even a concept of a thermodynamic phase, in a system with a finite number of degrees of freedom. Nevertheless, one would like to define $T_c(L)$ roughly to be the temperature where the ferromagnetic alignment of the spins within the nanoparticle becomes stable against thermal fluctuations. The temperature $T_c(L)$ will be denoted as the *reduced Curie temperature* in the following. In a simple mean-field picture, one finds $T_c(L) < T_c(\infty)$ where $T_c(\infty)$ is the precisely defined Curie temperature of the corresponding (infinite) bulk system. The transition, or smooth crossover, from a paramagnetic to an ordered state in the nanosystem must be described within models of interacting microscopic (atomic) spins [10, 96]. Below $T_c(L)$ the different *microspins* are tightly bound together and form a huge *macrospin* [18, 96]. For a finite-size and spin-isotropic system, the direction of the macrospin fluctuates strongly, i.e., the magnetic state of the system is not stable temporally. Anisotropies give rise to superparamagnetic behavior for temperatures above the so-called blocking temperature $T_b(L)$, i.e., for $T_b(L) < T < T_c(L)$. Both quantities are size-dependent. It is rather the blocking temperature $T_b(L)$ than $T_c(L)$ that is relevant for storage technology since it characterizes the crossover from the stable ferromagnetic state at low temperature T to the superparamagnetic state where the system switches between different energy minima determined by magnetic anisotropies. But $T_b(L)$ cannot be considered as a pure property of the system. It must be seen as a relative value, which depends on the observation time t. For $t \to \infty$, there is no blocking of the magnetization as eventually the anisotropy energy barrier is overcome by thermal fluctuations or even due to quantum tunneling, and hence $T_b(L) \to 0$. For $t \to 0$ (referring to, e.g., laser-probe methods), $T_b(L) \to T_c(L)$ while for intermediate t (like in SP-STM) $0 < T_b(L) < T_c(L)$.

For the infinite system, a magnetic phase transition is characterized by a divergence of the correlation length ξ, which characterizes the spatial decay of the spin-spin correlation function. For a nanosized system, on the other hand, it is by no means clear how the crossover at the reduced Curie temperature $T_c(L)$ manifests itself in the correlation function.

To close up on these questions, the next section examines the temperature dependency of the correlation function of nanosized systems in more detail.

5.3 Critical temperatures from the spin-spin correlation function

The correlation function between two spins $\boldsymbol{S}_i$ and $\boldsymbol{S}_j$ at positions $\boldsymbol{r}_i$ and $\boldsymbol{r}_j$ is given by

$$G(\boldsymbol{r}) = \langle \boldsymbol{S}_i \boldsymbol{S}_j \rangle \tag{44}$$

where $\langle ... \rangle$ is the canonical thermal average at temperature T. For a translationally invariant bulk system, the correlation function is homogeneous and depends on the translation vector $\boldsymbol{r} = \boldsymbol{r}_i - \boldsymbol{r}_j$ only, while in case of a finite system it depends on $\boldsymbol{r}$ and on the reference site in addition. For the following discussion an averaged correlation function is defined, which is independent of the direction and depends on the distance $r = |\boldsymbol{r}_j - \boldsymbol{r}_i|$ only:

$$G(r) = \frac{1}{n(r)} \sum_{\substack{i<j, \\ |\boldsymbol{r}_i - \boldsymbol{r}_j| = r}} \langle \boldsymbol{S}_i \boldsymbol{S}_j \rangle \tag{45}$$

Here, the sum in the first term runs over all $n(r)$ pairs separated by the distance r. $G(r)$ directly refers to X-ray or neutron-scattering experiments. Furthermore, a *connected correlation function* is defined

$$\tilde{G}(r) = G(r) - M^2, \tag{46}$$

where $M = |\sum_i \boldsymbol{S}_i|/L$ and L being the number of sites. Apart from a constant factor, $\boldsymbol{S}_i$ is the local magnetic moment at position $\boldsymbol{r}_i$, and thus M is the magnetization of the nanosystem. For temperatures above the blocking temperature, M averages to zero. But even below $T_\mathrm{b}(L)$ the magnetization vanishes, $M = 0$, in an exact calculation. The reason for the vanishing magnetization is the infinite time averaging in exact calculations. If the average $\langle ... \rangle$ is interpreted as a time average and if the time constant defining the average (life-time of a state) is large as compared to the observation time t, M is finite for temperatures below the blocking temperature corresponding to t. Hence, the function $\tilde{G}(r)$ will strongly differ from $G(r)$ or even vanish. All temperatures T at which $\tilde{G}(r)$ vanishes ($\tilde{G}(r) \to 0$) then lie at or below the blocking temperature T_b.

The following section presents results of the connected correlation function determined by means of exact-diagonalization in a simple Ising model.

5.3.1 Ising model

To start the discussion, a ferromagnetic ($J > 0$) Ising model is considered:

$$\mathcal{H} = -J \sum_{\langle ij \rangle} S_y^i S_y^j, \tag{47}$$

with Ising variables S_y^i on a one-dimensional chain of length L with open boundary conditions. The sum runs over all pairs of nearest neighbor sites. Results for $L = 10$ and different temperatures are displayed in Figure 27 (a). Note, that there is a simple exponential decay of the correlations, $\tilde{G}(r) \propto \exp(-r/\xi)$, on a length scale ξ, which at low temperatures exceeds the system size. Although in the low-temperature regime the microspins are perfectly aligned ferromagnetically and although they become uncorrelated on length scales much smaller than the system size in the high-temperature limit, there is no meaningful *Curie point* that could be extracted from $\tilde{G}(r)$. Qualitatively, not much happens as a function of T. The absence of a Curie point, $T_c(L) = 0$, is of course not unexpected. It corresponds to a featureless magnetic susceptibility $\chi(T)$ and to the fact that $T_c(\infty) = 0$ for the infinite Ising chain. Only at $T = 0$, the system *freezes* in one of the two ferromagnetic ground states, i.e., $M = 1$, and therefore, due to the definition (46), the correlation function discontinuously jumps to $\tilde{G}(r) = 0$. This might be expressed as a vanishing blocking temperature, $T_b(L) = 0$, reflecting the fact that an exact calculation corresponds to an infinite observation time t.

For a finite two-dimensional Ising array with $L = 5 \times 5$ sites, the situation changes completely. Calculations for $L = 25$ are easily done by numerical exact-diagonalization. Results obtained for the connected correlation function $\tilde{G}(r)$ are shown in Figure 27 (b). The result is surprising: one finds two or, including $T = 0$ (see below), three different crossover temperatures.

For high temperatures, the correlations decay exponentially, see $T = 2.8\ J$, for example. Below a temperature T_3, however, the trend can no longer be fitted by an exponential of the form $\exp(-r/\xi)$. One finds $T_3 \approx 2.2\ J$. This is close to the bulk Curie temperature of the two-dimensional Ising model $T_3 \approx T_c(\infty) = 2/\ln(1+\sqrt{2})J \approx 2.27\ J$. Upon lowering T one then finds another temperature $T_2 \approx 1.9\ J$ which is characterized by a change of the curvature of $\tilde{G}(r)$. Below

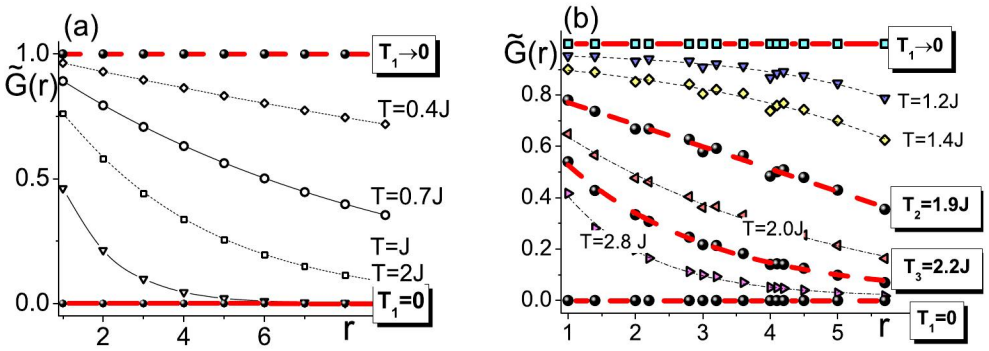

Figure 27: The connected correlation function $\tilde{G}(r)$ (see equation (46), symbols) calculated for an open Ising chain consisting of $L = 10$ sites (a) and for an open 5×5 Ising square lattice (b). The data are fitted with equation (48). The temperatures T_1 (a) and T_1, T_2, T_3 (b) are highlighted by thick red lines.

T_2, the trend of $\tilde{G}(r)$ is no longer convex but concave until r reaches the system boundary. As the exact-diagonalization data correspond to an infinite observation time, the third temperature scale T_1 is trivially given by the vanishing blocking temperature $T_1 = T_\mathrm{b}(L) = 0$.

To determine the different temperatures a fit function of the connected correlation function is introduced in the following section.

5.3.2 Model correlation function

To extract the different temperature scales T_1, T_2, and T_3, it is proposed to fit the correlation function to the following expression with three temperature-dependent parameters:

$$\tilde{G}(r) = \tilde{G}(r,T) \approx B(T)e^{-r/\varepsilon(T)} + y(T) \tag{48}$$

In this way T_3 is defined by the temperature where $y(T)$ becomes non-zero, i.e., where a deviation from a purely exponential decay of $\tilde{G}(r)$ is found. For the infinite system, $L \to \infty$, this happens right at $T_3 = T_\mathrm{c}(\infty)$ where a power-law decay is expected [94, 97]. Thereby, the simple fit formula, equation (48), will provide a rough estimate for $T_\mathrm{c}(\infty)$ based on a single calculation of $\tilde{G}(r)$ for a finite system. Monte Carlo calculations show that this estimate reliably gives $T_\mathrm{c}(\infty)$ within an error of the order of 1%. For example, using the fit for Monte Carlo data obtained for the 5×5 Ising array, one finds $T_3 = 2.20 \pm 0.02$ while for the 8×8 lattice $T_3 = 2.26 \pm 0.02$. This represents a cheap but rough way to get $T_\mathrm{c}(\infty)$ from a slow annealing of a single finite system. For temperatures below the blocking temperature, $\tilde{G}(r) = 0$ ($G(r) = 1$). Hence, $T_1 = T_\mathrm{b}(L)$ is indicated by $B(T) = 0$

and $y(T) = 1$ when fitting the data using equation (48). The main purpose of equation (48), however, is to get an estimate for T_2 where $\tilde{G}(r)$ is a linear function to a good approximation. A linear $\tilde{G}(r)$ requires $\varepsilon(T) \to \infty$ for $T \to T_2$. To get a finite slope, also $B(T) \to \infty$ for $T \to T_2$ is needed, and finally $y(T) \to \infty$ since $|G(r)| \leq 1$.

Equation (48) has been used to fit the unknowns $\varepsilon(T)$, $B(T)$, and $y(T)$ to numerically exact data for one-, two-, and three-dimensional Ising systems of different size L as well as for finite isotropic and anisotropic Heisenberg systems. It turns out that the quality of the fit is exceptionally good in the entire temperature range, see the lines in Figures 27 (a) and (b), for example. For temperatures $T_\mathrm{b}(L) < T < T_2$ the concave trend has been found with negative values for $B(T)$ and $\varepsilon(T)$ while $y(T) > 0$. For $T_2 < T < T_\mathrm{c}(\infty)$, both $B(T)$ and $\varepsilon(T)$ have been positive while $y(T) < 0$, and the trend of $G(r)$ is convex. Finally, for $T > T_3$ both $B(T)$ and $\varepsilon(T)$ remain positive while $y(T)$ vanishes leaving an exponential decay of $\tilde{G}(r)$.

5.3.3 Curie temperature

T_2 has been identified with the reduced Curie temperature of the system, $T_2 = T_\mathrm{c}(L)$. This provides a meaningful definition of $T_\mathrm{c}(L)$ for a finite system that is based on the spin correlation function. It is motivated by the physical idea that at $T_\mathrm{c}(L)$ the correlation length exceeds the system size but additionally takes into account that the nanosystem is bounded by surfaces. For an infinite system the spin correlation function is always convex, i.e., its slope is negative but increasing as a function of increasing distance r. The unusual concave trend of the correlation function at lower temperatures must therefore be a direct consequence of the presence of surfaces. This is demonstrated with Figure 28 for a larger system consisting of 20×20 Ising spins on a square array. Due to missing nearest neighbors at the nanoparticle surface, fluctuations of the local spins are stronger and result in a reduced average surface magnetization. This also implies a strongly decreasing correlation function $G(r)$ close to the surface and along any direction. For the averaged correlation function $\tilde{G}(r)$, this surface effect competes with the convex bulk trend of $\tilde{G}(r)$. The surface effect dominates for $T > T_\mathrm{c}(L)$ and drives the nanosystem to a paramagnetic state while for $T < T_\mathrm{c}(L)$ the bulk of the nanosystem causes an ordered superparamagnetic state, and the surface manifests itself in stronger fluctuations of the spins and a concave trend of $\tilde{G}(r)$ only. Note, that

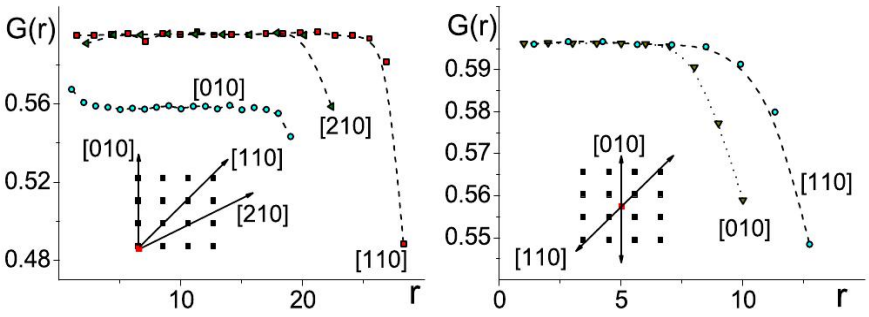

Figure 28: Spin correlation function $G(r)$ (see equation 44, symbols) calculated for a 20×20 Ising square lattice with open boundaries starting from an edge (left) and from the central site (right) as obtained by Monte Carlo simulations at $T = 0.5\ J \ll T_c(\infty)$. The lines are guides to the eyes only.

the fit with the model correlation function, equation (48), allows to characterize $T_c(L)$ by a divergence of the parameter $\varepsilon(T)$, which therefore might be called a *virtual correlation length*. On the other hand, the Curie temperature of the infinite system $T_c(\infty)$ is given by a divergence of $r_v \equiv -\varepsilon(T) \ln[-y(T)/B(T)]$ since $y(T)$ becomes finite at $T_c(\infty)$ in the fit. r_v is the distance at which $\tilde{G}(r)$ vanishes, $\tilde{G}(r_v) = 0$. The distance is virtual because it is always larger than the system size (see Figure 29 (a)).

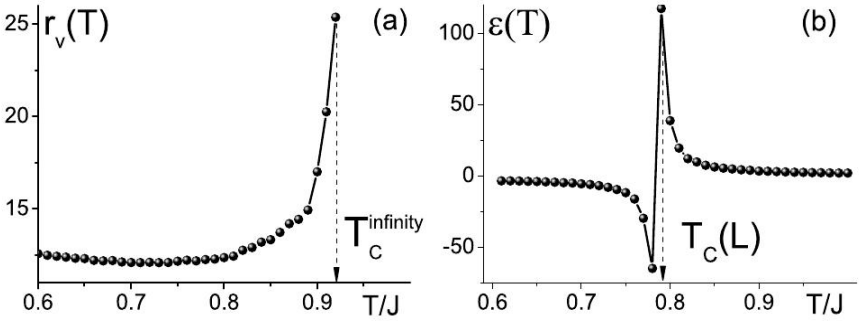

Figure 29: Model $\tilde{G}(r)$ (see equation (48)) as obtained by fitting the parameters to results of Monte Carlo simulations (10^6 sweeps per temperature) for an anisotropic Heisenberg model ($K = 0.6\ J$) on an 8×8 square lattice with open boundary conditions. (a) Temperature dependence of the virtual distance r_v (see text). (b) Virtual correlation length $\varepsilon(T)$.

5.3.4 Blocking temperature

The question of a finite blocking temperature T_b can be addressed by Monte Carlo simulations when interpreting MCSs as time steps [49]. A finite number of MCSs

corresponds to an incomplete statistical average and thus to a finite observation time t.

Calculations have been performed according to the classical Heisenberg model introduced in section 5.1.1. An example for $K = 0.6\ J$ is given in Figure 30. The

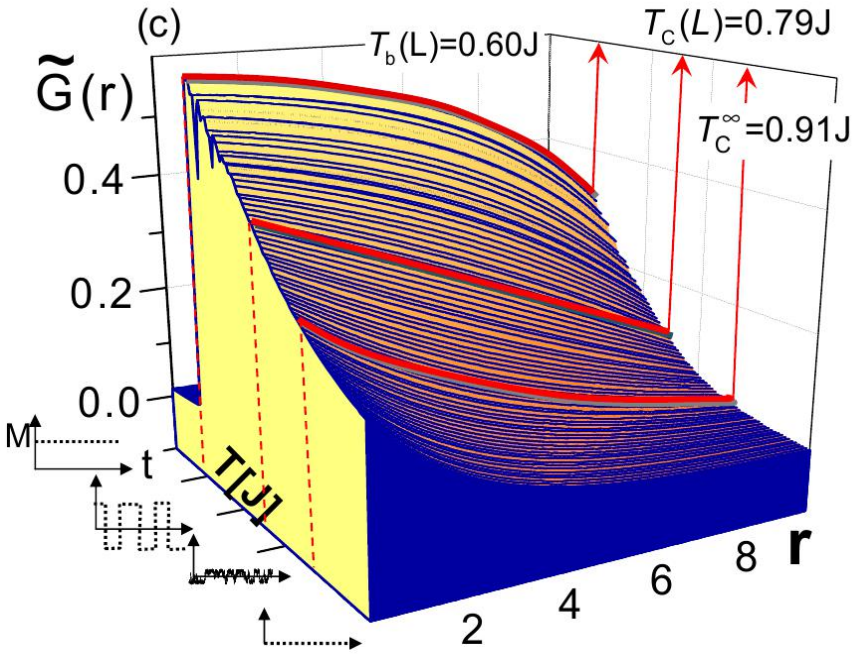

Figure 30: Model $\tilde{G}(r)$ (see equation (48)) as obtained by fitting the parameters to results of Monte Carlo simulations (10^6 MCSs per temperature) for an anisotropic Heisenberg model ($K = 0.6\ J$) on an 8×8 square lattice with open boundary conditions. $\tilde{G}(r)$ as a function of r and T. The temperatures $\infty > T_c(\infty) > T_c(L) > T_b(L) > 0$ are highlighted. In each of the four corresponding temperature ranges, the typical Monte Carlo time dependence of $M = M(t) \propto \langle \sum_i S_i^y \rangle$ is shown in insets (see text for discussion).

fit of the Monte Carlo results by equation (48) is accurate for all temperatures and all values of K such that the three different temperature scales, $T_b(L)$, $T_c(L)$, and $T_c(\infty)$ can be extracted easily. The finite blocking temperature manifests itself in the jump of $\tilde{G}(r)$ as a function of T which is due to the jump of M at $T \approx 0.6\ J$. The order of magnitude for T_b seems to be given by K. However, $T_b(L)$ decreases with increasing observation time t, i.e., with an increasing number of MCSs per temperature. At fixed L, $T_b(L) \to 0$ has been found to be logarithmically if $t \to \infty$.

Figure 30 nicely demonstrates that an astonishingly complex behavior of the spin correlation function is found for finite anisotropic nanosystems. The qualitatively different physics within the different temperature ranges, i.e., $0 < T_b(L) < T_c(L) < T_c(\infty) < \infty$, also shows up in the qualitatively different behavior of the

order parameter M as a function of (Monte Carlo) time during the simulation, see insets in Figure 30: below $T_{\rm b}(L)$, on the scale set by the observation time, the magnetization freezes in one of the values corresponding to the degenerate energy minima of the anisotropic model; for $T_{\rm b}(L) < T < T_{\rm c}(L)$ the magnetization switches between these values with a switching time which is much smaller than the lifetime of a state; for $T_{\rm c}(L) < T < T_{\rm c}(\infty)$ the system still switches but the lifetimes are comparable to the switching times; and finally above $T_{\rm c}(\infty)$ correlations decay exponentially and $M = 0$.

In the next section the size dependence of the three critical temperatures is presented.

5.4 Size dependence of the critical temperatures

Note, that this physics is characteristic of a finite system: for constant t but increasing system size $L \to \infty$ all three temperatures merge to the Curie temperature of the infinite system $T_{\rm c}(\infty)$. With increasing L, but fixed temperature, the curvature of $\tilde{G}(r)$ increases, i.e., it becomes less convex, changes from convex to concave, or becomes more concave. This is due to the less and less important effect of the nanoparticle's surfaces. At the same time $\tilde{G}(r)$ and its slope increases. This implies that $T_{\rm c}(L)$ is an increasing function of the system size. The same holds for the blocking temperature since with increasing L the energy of the anisotropy barrier increases and higher temperature is needed to induce a thermal switching of the magnetization.

The system-size dependence of the reduced Curie temperature, as obtained from the fit of the correlation function, is displayed in Figure 31. Comparing $T_{\rm c}(L) = T_2$ with the reduced Curie temperature defined by the maximum of the magnetic susceptibility and by the maximum of the specific heat, one finds that the asymptotic behavior is approached significantly faster when using the correlation-function fit. The latter also provides a reliable estimate for the bulk Curie temperature as it is also shown in Figure 31. In addition, Figure 32 shows the dependence of the blocking temperature on the system size. For fixed system size and with increasing Monte Carlo time, i.e., with increasing number of MCSs, the blocking temperature decreases logarithmically (see data for $L = 8 \times 8$ in Figure 32).

The analysis showed that $T_{\rm c}(L)$ satisfies the finite-size scaling law $(T_{\rm c}(\infty) - T_{\rm c}(L))/T_{\rm c}(\infty) = (L/L_0)^{-1/D\lambda_s}$ [98, 99]. $\sqrt{L_0}$ corresponds to a microscopic length scale, and its order of magnitude is one. The shift exponent λ_s is related to the

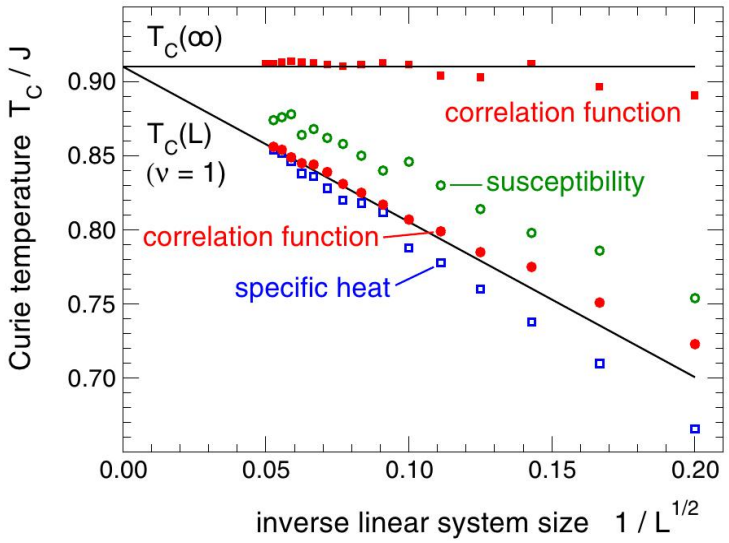

Figure 31: The reduced Curie temperature, as obtained from the maximum of the specific heat (open squares), from the maximum of the susceptibility (open circles), and from the correlation-function fit (filled circles), as functions of the (inverse) linear system size and the bulk Curie temperature (filled squares), as obtained from the fit of the correlation function at the respective system size. Solid line: $(T_c(\infty) - T_c(L)/T_c(\infty) = (L/L_0)^{1/2}$ corresponding to the exponent $\nu = 1$ and with $L_0^{1/2} = 1.15$. Calculations for the $D = 2$ anisotropic Heisenberg model with $K = 0.6\ J$.

exponent of the correlation function via $\lambda_s = 1/\nu$. In case of the anisotropic Heisenberg model, the data for $T_c(L)$ for system sizes up to $L = 19 \times 19 = 361$ are consistent with $\nu = 1.0$ (and $L_0 = 1.15$). This is different from the classical exponent ($\nu = 0.5$) and agrees with the exponent for the $D = 2$ Ising model ($\nu = 1$). Note, that the results for the size dependence of the blocking temperature are also consistent with the same scaling law that describes $T_c(L)$, see Figure 32. The exponent λ_s, however, is different and slightly larger than $1/\nu$ for $\nu = 1$. Actually, it is by no means clear that the blocking temperature should satisfy a scaling law since for the infinite system it has no meaning independent from the Curie temperature. But an investigation of this point is beyond the scope of the present study.

In the next section the results obtained from Monte Carlo simulations are compared with results from mean-field theory.

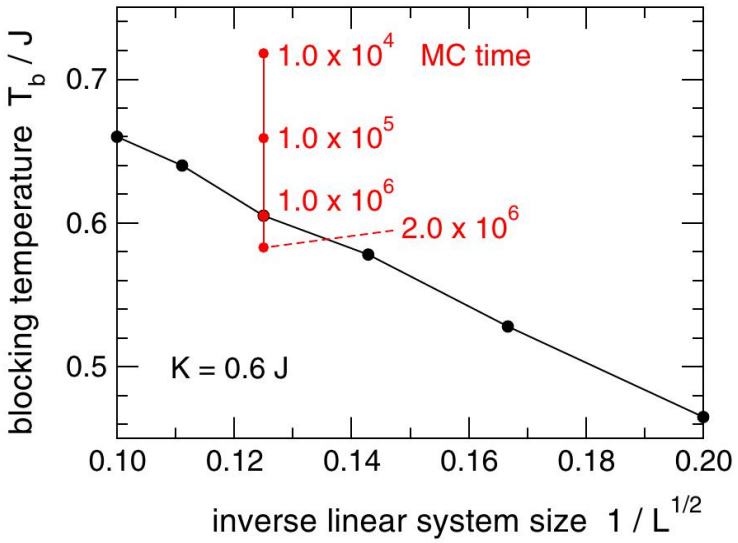

Figure 32: Blocking temperature, as obtained from the correlation-function fit, as a function of the (inverse) linear system size for the $D = 2$ anisotropic Heisenberg model with $K = 0.6\ J$ and using 10^6 MCSs. Lines connect the data points. For the $L = 8 \times 8$ system, the dependence of T_b on the Monte Carlo time is given by the red circles as indicated.

5.5 Static mean-field theory

The characteristic trends of the spin-correlation function in the different temperature regimes are strongly determined by the presence of surfaces, see Figure 28. It is tempting to simply explain the concave trend of the correlation function at temperatures below $T_c(L)$ by the reduced coordination numbers at the nanoparticle surfaces. This has been checked by E. Y. Vedmedenko and M. Potthoff [92] by performing calculations using periodic boundary conditions. In fact, a convex curvature of the correlation function is found in one and in two-dimensions and for all temperatures in agreement with previous work [10]. Since the surface-to-volume ratio is smaller in one- as compared to two-dimensions, the simple coordination-number argument is also consistent with the absence of a Curie temperature in one-dimension. The findings have been checked by performing corresponding calculations for three-dimensional finite lattices: in fact, the low-temperature concave trend has been found to be even more pronounced here.

Simple coordination-number arguments are included in the Landau theory of magnetic systems bounded by surfaces [100–103] where the usual Landau free-energy functional is considered but with an additional surface free-energy term. The resulting Landau mean-field theory is essentially equivalent to static mean-

field theory for a discrete spin model. For a finite system, this has been implemented numerically by E.Y. Vedmedenko [92], and $\tilde{G}(r)$ has been evaluated for different one- and two-dimensional lattices studied here. As expected, static mean-field theory gives a phase transition rather than a smooth crossover. The mean-field Curie temperature $T_{\mathrm{c}}^{\mathrm{MF}}$ of the finite system very much depends on the size and the geometry of the underlying lattice. If interpreted as $T_{\mathrm{c}}(L)$, the mean-field Curie temperature $T_{\mathrm{c}}^{\mathrm{MF}}$ yields a strong overestimation. Here, however, the question is whether besides $T_{\mathrm{c}}^{\mathrm{MF}}$ there is a crossover temperature at which the spin-correlation function changes qualitatively from convex to concave.

The spin-spin correlation function can be obtained in two ways, either directly by computation of the thermal average $\langle \boldsymbol{S}_i \boldsymbol{S}_j \rangle$ or as the response of the local magnetic moment at site i to a local magnetic field at site j, i.e., $\partial \langle \boldsymbol{S}_i \rangle / \partial B_j$. In principle, both ways are equivalent because of the fluctuation-dissipation theorem $\langle \boldsymbol{S}_i \boldsymbol{S}_j \rangle - \langle \boldsymbol{S}_i \rangle \langle \boldsymbol{S}_j \rangle = T \partial \langle \boldsymbol{S}_i \rangle / \partial B_j$. This is not respected by static mean-field theory, which just neglects non-local correlations. Therefore, within the mean-field theory the spin correlations can be addressed via the linear-response relation $G(r) = T \partial \langle \boldsymbol{S}_i \rangle / \partial B_j$ only. For an infinite translationally invariant lattice, this yields the Ornstein-Zernike form for the correlation function. Here, for finite systems, we determine $\langle \boldsymbol{S}_i \rangle$ numerically by solving the static mean-field equations and compute the derivative with respect to B_j numerically. Looking at the resulting averaged correlation function $\tilde{G}(r)$, a convex trend has always been found, for any system size and dimension. This shows that the results and the crossover temperature $T_{\mathrm{c}}(L)$ cannot be captured by a mean-field or Landau approach and, therefore, represent a correlation effect for which simple coordination-number arguments must be taken with care.

5.6 Summary and Conclusion

As compared to infinite bulk systems, the theoretical description of collective magnetic order is more complex for nanosized materials. Due to the finite system size there are no clear-cut regions in parameter space where ferromagnetic order is realized. Furthermore, the magnetic state is not stable temporally and consequently the order parameter, i.e., the magnetization of the nanoparticle, fluctuates with a time constant that has to be compared with the (experimental) observation time. These facts give rise to uncertainties in the definition of the Curie temperature and imply the existence of a second temperature scale, the blocking temperature,

which again cannot be defined precisely.

The studies presented, based on different analytical and numerical techniques, have demonstrated, that a meaningful definition of the reduced Curie temperature of a finite spin system can be given that relies on the analysis of a suitably defined average spin correlation function, denoted as connected correlation function. Upon lowering the temperature, the correlation function changes its curvature at $T_c(L)$. This definition is consistent with the common concepts and comes closest to the expectation that the Curie point is the temperature at which the correlation length exceeds the particle size. In particular, it accounts for the delicate interplay between the (bulk) tendency to ordering and the (surface) tendency to enhance fluctuations. It has been shown that the concept can be applied to different one-, two-, and three-dimensional classical spin models and that $T_c(L)$ can be extracted with an accuracy that even allows to determine a shift exponent.

Further, it has been demonstrated that the blocking temperature scale is accessible with a Monte Carlo approach by performing an incomplete statistical average. A sharp jump is visible in the average spin-correlation function at $T_b(L)$. However, the blocking temperature is only defined with respect to an observation time (a finite number of MCSs) and, therefore, represents a relative quantity.

Concluding, the combined application of exact-diagonalization, Monte Carlo, and mean-field techniques has uncovered a strikingly complex behavior of the spin correlations in nanoparticles with qualitatively different temperature scales. Since simple coordination-number arguments are unable to give a quantitatively correct picture of the physics, the temperature trends must be seen as effects of strong spin correlations.

6 Superparamagnetic magnetization switching of elongated Fe/W(110) nanoislands

The previous section gave a detailed theoretical description of the collective magnetic order in systems of finite size. The critical temperatures, at which the nanosized systems turn from the paramagnetic state to the superparamagnetic state and from the superparamagnetic state to the stable ferromagnetic state have been defined. The present chapter focuses on the magnetization reversal of nanoislands in the superparamagnetic temperature region. Motivated by the experimental work of Stefan Krause *et al.* [9, 84] in the group of Professor Roland Wiesendanger [104] the size, shape, and temperature dependencies of the superparamagnetic magnetization switching of nanoislands consisting of $50 - 150$ atoms have been studied by means of Monte Carlo simulations. The presented study focuses on elongated nanoislands like Fe/W(110), expanding one of the two crystalline lattice directions of the nanoisland ([001] or $[1\bar{1}0]$) and keeping the other constant.

Parts of the material presented in this chapter has been originally published in *Physical Review Letters*: "S. Krause, G. Herzog, T. Stapelfeldt, L. Berbil-Bautista, M. Bode, E. Y. Vedmedenko and R. Wiesendanger, *Magnetization Reversal of Nanoscale Islands: How Size and Shape Affect the Arrhenius Prefactor*, Phys. Rev. Lett., 103, 12, 127202 (2009)" [84] in a common publication of theory and experiment, in which my contribution is restricted to the simulated results.

The chapter starts with an introduction of the simulated system and the applied Monte Carlo simulation scheme. It follows a brief introduction to superparamagnetic switching and the experimental and theoretical method of observing a switching event. Then a discussion of the nature of the domain wall nucleation and propagation process in Fe/W(110) nanoislands is presented. After that, the size and shape dependency of the energy barrier and the Arrhenius pre-factor is presented giving insights which are, until now, not accessible by experiments. At the end, the influence of a spin-current on the superparamagnetic magnetization switching is briefly discussed.

6.1 The system properties and the simulation scheme

6.1.1 The system properties and its Hamiltonian

In section 3.1 the anisotropic exchange interaction of the monolayer Fe/W(110) has been introduced, defining the exchange energy constants up to third nearest neighbors. Because the nearest neighboring exchange interactions are weaker than the other contributions, it could be neglected and at the same time the general properties of an Fe/W(110) nanoisland, such as the orientation of the domain walls, preserved. As the following study of thermally induced magnetization switching of nanoislands like Fe/W(110) has been extremely expensive in terms of the computational effort, the first nearest neighbor interaction and the hard-axis anisotropy have been neglected in the simulations. Figure 33 shows a sketch of the used Fe/W(110) exchange bonds, indicated by the thick black lines.

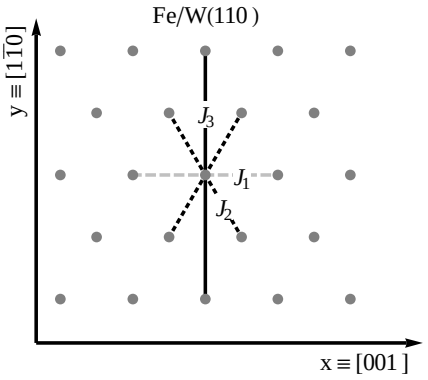

Figure 33: Sketch of the Fe/W(110) exchange bonds. Only second nearest neighbor ($J_2 = J_{[1\bar{1}1]}$) and third nearest neighbor ($J_3 = J_{[1\bar{1}0]}$) exchange interactions have been taken into account for the simulation, indicated by the thick black lines. The neglected first nearest neighbor exchange bonds ($J_1 = J_{[001]}$) are faintly shown (gray lines).

The magnetic properties of the system have been described by the following Hamiltonian:

$$\mathcal{H} = -J_{[1\bar{1}1]} \sum_{\langle ij \rangle_2} \boldsymbol{S}_i \boldsymbol{S}_j - J_{[1\bar{1}0]} \sum_{\langle ij \rangle_3} \boldsymbol{S}_i \boldsymbol{S}_j - K^{\text{surf}}_{[1\bar{1}0]} \sum_i (S^i_{[1\bar{1}0]})^2 - K^{\text{rim}}_{[1\bar{1}0]} \sum_i (S^i_{[1\bar{1}0]})^2 \quad (49)$$

where $J_{[1\bar{1}1]}$ is the ferromagnetic exchange coupling between the second nearest neighbors and is set equal to one. $J_{[1\bar{1}0]}$ is the exchange coupling between the third nearest neighbors and is twice as large as $J_{[1\bar{1}1]}$ [46–48]. As mentioned in section 4.1.1 it is known from experiments that the atoms situated at the rim of a monolayer nanoisland exhibit a much higher anisotropy than the surface atoms

[84, 85]. Therefore, two easy-axis anisotropy constants have been used, which have been determined by experimental investigations of Stefan Krause *et al.* [9, 84]. Both anisotropies are pointing in-plane along $[1\bar{1}0]$: $K^{\mathrm{surf}}_{[1\bar{1}0]} = 0.043\ J_{[1\bar{1}1]}$ is the anisotropy constant for the spins situated on the surface of the island and $K^{\mathrm{rim}}_{[1\bar{1}0]} = 0.44\ J_{[1\bar{1}1]}$ the anisotropy constant of the spins situated at the rim of the island. The first two sums run over the nth nearest neighbor pairs $\langle ij \rangle_n$ and the last two sums run over all lattice sites i. An overview of the energy constants used is given by SET4 of Table 1.

6.1.2 The geometries of the nanoislands

The simulations have been performed for a range of different elongations of a nanoisland. The number of atomic rows along [001] or $[1\bar{1}0]$ has been increased, while the other side has been kept fixed, see Figure 34. The length of the fixed side reached about 10 AR and the length of the elongated side has been varied from about 10 AR up to 30 AR.

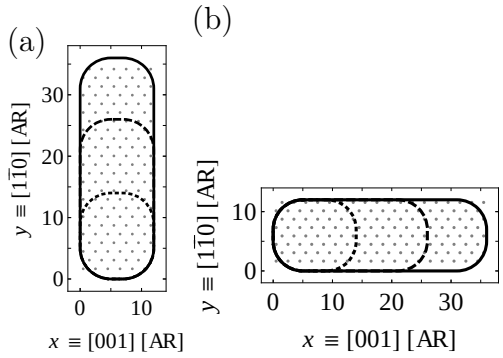

Figure 34: Sketch of the elongated Fe/W(110) nanoislands. The system size is varied by keeping either the number of atomic rows along [001] (a) or along $[1\bar{1}0]$ (b) fixed and then successively increasing the elongation along the other direction. The dashed lines shall indicate the rim of islands with different sizes, while the solid lines correspond to the rim of the largest island simulated.

6.1.3 The scheme of the Monte Carlo simulation

The samples have been slowly annealed for temperatures in the superparamagnetic temperature region. For each temperature step and island size, the nanoisland has been relaxed for $t = 10^7$ MCS and the magnetization determined. To assure reliable statistics the simulation of each temperature step has been repeated ten times with different seeds of the random number generator. The switching rates

have then been calculated from the time evolution of the easy-axis magnetization (see next section), which switches between two states back and forth and the results averaged over the simulations with different seeds.

Note, that no predefined configuration has been used and in contrast to previous investigations [105–107] no external magnetic field has been applied. Hence, the system was free to evolve statistically without any directional influence of an external pressure. The next section introduces the time evolution of the magnetization switching and how the switching rates have been determined.

6.2 Superparamagnetic magnetization switching

6.2.1 Arrhenius like switching

Néel and Brown developed a theoretical description of the magnetization switching of a monodomain particle with uni-axial anisotropy, which switches its magnetization due to ambient heat only [5, 6]. In this so called Néel-Brown law the mean lifetime $\bar{\tau}$ between consecutive switching events of a particle as a function of the temperature T is characterized by its activation energy E_B and attempt frequency ν_0:

$$\bar{\tau} = \nu_0^{-1} \exp(E_\mathrm{B}\beta), \tag{50}$$

with $\beta = 1/k_\mathrm{B}T$ the inverse temperature. The activation energy will be denoted as energy barrier in the following, as it corresponds to the energy to be overcome in order to switch between the two degenerated states, spin-up and spin-down. In the Néel-Brown law the magnetization reversal is assumed to take place via coherent rotation of all magnetic moments inside the particle. The energy barrier E_B is then given by the total magnetic anisotropy energy of the particle and the attempt frequency is commonly compared to the Larmor precession [6]. Analytical calculations and Monte Carlo simulations of ferromagnetic nanoparticles, by Nowak and Hinzke [106], showed that in a system with strong easy-axis anisotropy the energy barrier is proportional to the cross section of the system and is not proportional to the total magnetic anisotropy energy of the particle. They showed, that the magnetization reversal then takes place via domain wall nucleation and propagation and not by coherent rotation. Later it has been confirmed by SP-STM experiments that Fe/W(110) nanoislands switch their magnetization by domain wall nucleation and propagation [9, 19, 108]. Like in the Néel-Brown model an Arrhenius-like switching behavior is expected, with an energy barrier E_B repre-

senting the energy needed to successfully nucleate a domain wall.

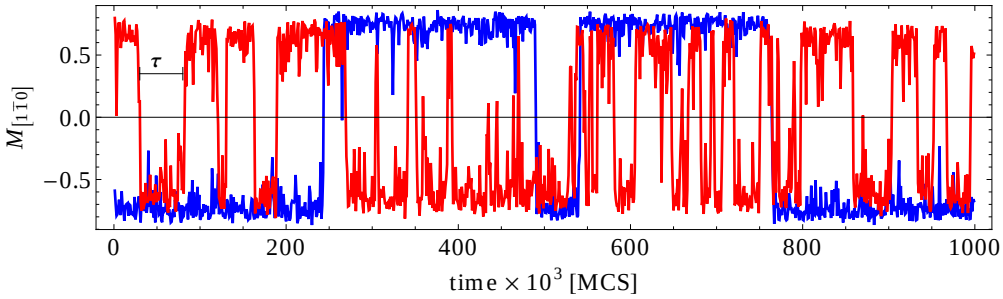

Figure 35: Time dependence of the normalized easy-axis magnetization $M_{[1\bar{1}0]}$ of a nanoisland consisting of about 100 atoms at $T = 0.7\ J/k_B$ (blue) and $T = 0.9\ J/k_B$ (red). Only the easy-axis component of the magnetization is shown, as the other components are close to zero.

For sufficiently large observation times t the magnetization of the Fe/W(110) nanoisland switches between the two states, spin-up and spin-down. In an SP-STM experiment, the magnetization switching is observed by changes in the $\frac{dI}{dU}$ signal, which is reflecting the respective orientation of the tip and the sample magnetization [9]. In the simulations, the magnetization switching is observed by calculating the easy-axis magnetization for each time step, as shown by Figure 35. A detailed description how the switching events are defined and counted is given for experiments in [108] and for the simulations in [19]. The data points in Figure 35 show the magnetization component of the island along its easy-axis as a function of the time at two different temperatures inside the superparamagnetic regime: blue for a lower temperature at $T = 0.7\ J/k_B$ and red for a higher temperature at $T = 0.9\ J/k_B$. It shows the magnetization switching between the two states, with a clearly enhanced switching frequency for the higher temperature. When observing the magnetization switching over a longer time period ($t = 10^7$ MCS in this simulation) one can determine the mean lifetimes $\bar{\tau}$, where $\bar{\tau} = \frac{\sum_i^n \tau_i}{n}$ and n is the number of switching events for the island at a given temperature. The switching rates ν are then given by the inverse mean lifetime: $\nu = 1/\bar{\tau}$.

In the following section the nucleation and propagation process of a domain wall in an Fe/W(110) nanoisland is discussed.

6.2.2 Nucleation and propagation of a domain wall in Fe/W(110) nanoislands

Before starting the discussion of the switching behavior of the investigated islands the nucleation and propagation process is examined in some detail. Figure 36

shows the fluctuation amplitude of the magnetization at each lattice site for two islands of different elongation at the same temperature, denoted as fluctuation map in the following. The fluctuations have been characterized using the root-mean-square deviation of the magnetization. The color scale corresponds to minimal fluctuation amplitude of the magnetization in blue and maximal fluctuation amplitude in red. One can clearly identify two regions with enhanced fluctuations

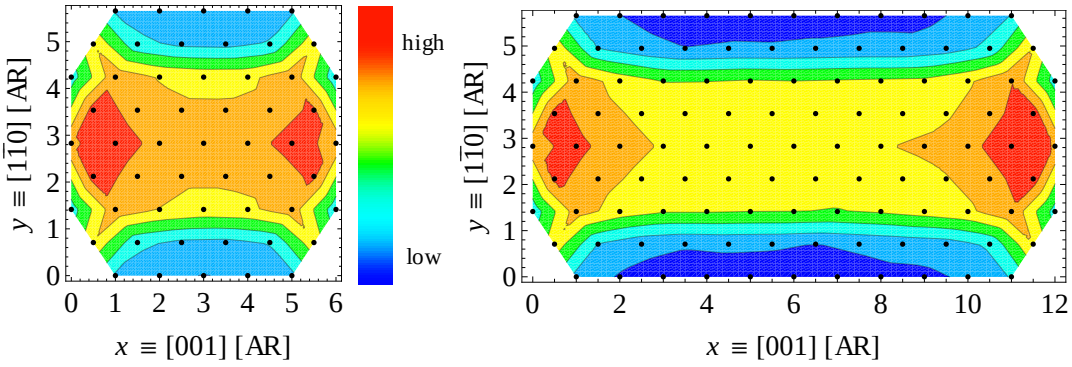

Figure 36: Contour plots of the fluctuation amplitude of the easy-axis magnetization for two islands of different elongation. The fluctuations have been determined for 10^7 MCS. The color scale reaches from low fluctuations in blue to high fluctuations in red.

lying at the [001] ends of the islands (dark red areas at the left and right-hand side of the two fluctuation maps). At these two ends the thermal assistance to nucleate a domain wall is maximal and leads to an enhanced domain wall nucleation probability. Furthermore, it shows the fluctuations at the $[1\bar{1}0]$ ends (blue) being smaller compared to the [001] ends. The reason for the stability of the system's $[1\bar{1}0]$ ends is on the one hand the weak exchange coupling along [001], and on the other hand, the larger anisotropy of the atoms situated at the rim of the islands.

If one defines a nucleation attempt as successful if the domain wall nucleation leads to a magnetization reversal of the island, then the enhanced fluctuations at the two [001] ends can be attributed to the unsuccessful nucleation attempts. The fluctuations arising from successful switching events are not visible in the fluctuations maps, because they are statistically uniformly distributed. Although the orientation and the propagation direction of a domain wall is determined by the Hamiltonian used and its energy constants, the exact location of nucleation spots could not be predicted a priori. The knowledge of their position, however, will play an important role in the later discussion, because the size and the location of the nucleation spots define the number of domain wall nucleation attempts.

In the next section the temperature dependency of the switching rates for the

different island elongations are shown.

6.2.3 The energy barrier

A logarithmic plot of the switching rates ν inside the superparamagnetic region for varying island dimensions is shown in Figure 37. The switching rates are plotted as a function of the inverse temperature β fitted by the Arrhenius function given by equation 50 (solid lines). The color scale corresponds to the size of the islands, from blue for small islands to red for large islands. The exact geometries of the islands are given in the inset. Already the color scale gives a direct hint that not only the system size defines the magnitude of the switching rates, otherwise the switching rates of equally sized (equal color) islands should overlap in Figure 37. $\nu(\beta)$ is linear in the superparamagnetic region reflecting an Arrhenius like switching behavior. In order to successfully nucleate a domain wall, an energy proportional to the

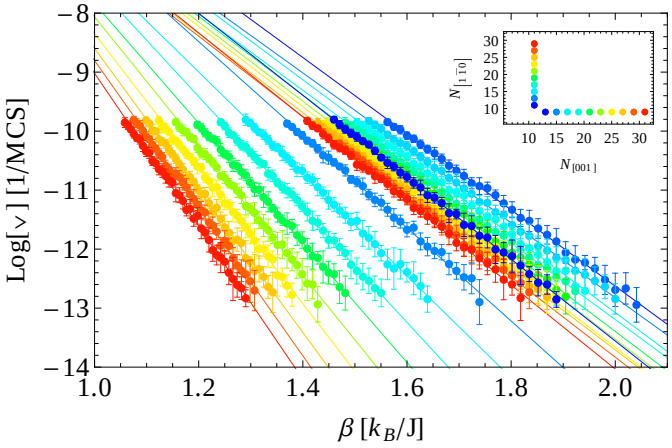

Figure 37: Logarithmic plot of the simulated switching rates ν as a function of the inverse temperature β for different system sizes with the corresponding Arrhenius fits (solid lines). From the Arrhenius fits one can directly determine the energy barrier E_{B} and the Arrhenius pre-factor ν_0. E_{B} is proportional to the slope of the fitted Arrhenius function and ν_0 is the interception with the ordinate. The inset displays the dimensions of all simulated islands. The color scale corresponds to the islands' size $L = N_{[1\bar{1}0]} \times N_{[001]}$ and is blue for small islands and red for large islands.

domain wall area S_0, and proportional to the square root of the exchange integral and the easy-axis anisotropy is needed. This domain wall energy corresponds to the energy barrier E_{B} and is given by:

$$E_{\mathrm{B}} \propto S_0 \sqrt{\frac{2J_{[hkl]}}{a} K_{[1\bar{1}0]}}, \tag{51}$$

with $J_{[hkl]} > 0$ the effective nearest neighbor exchange coupling constant, $K_{[1\bar{1}0]}$ the on-site easy-axis anisotropy and a the lattice constant. The energy barrier E_B is proportional to the area of the domain wall, which in turn is proportional to the width of the island. As a domain wall in Fe/W(110) orients along the $[1\bar{1}0]$ direction, the energy barrier should increase linearly with increasing length of the islands along $[1\bar{1}0]$ and stay constant for an increasing elongation along [001]. The energy barrier E_B corresponds to the slope of the fitted Arrhenius function and is shown in Figure 38. (a) shows the energy barrier as a function of the elongation along $[1\bar{1}0]$ and (b) the energy barriers for elongations along [001], both with a linear fit to the data points.

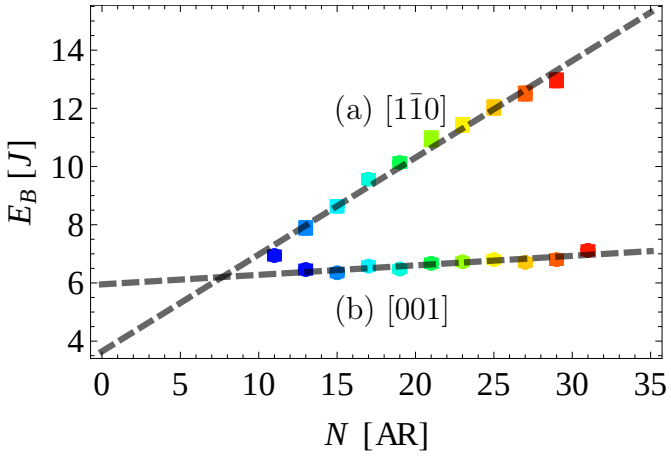

Figure 38: The energy barrier E_B as a function of the island elongation N. (a) corresponds to E_B as a function of the elongation along $[1\bar{1}0]$ and (b) to the elongation along [001]. The color scale corresponds to the system sizes $L = N_{[1\bar{1}0]} \times N_{[001]}$ and varies from small in blue to large in red. The gray dashed lines are linear fits to the data points.

The shape dependency of the energy barrier found for increasing elongations along $[1\bar{1}0]$, shown in Figure 38 (a), is in agreement with the expectations mentioned above: with increasing number of atomic rows along $[1\bar{1}0]$ the energy barrier for a domain wall nucleation increases, because the length of the domain wall is proportional to $N_{[1\bar{1}0]}$. Since the energy barrier depends strongly on the islands' dimension along $[1\bar{1}0]$, one can deduce, that the domain wall that moves through the islands during the switching process is oriented along the $[1\bar{1}0]$ direction and, therefore, propagates along the [001] direction. These results are in agreement with the experimental [9] findings and have also been confirmed by analyzing the spin configuration in the simulation for various switching events.

Unexpectedly, one finds the energy barrier increase for increasing elongation along [001], as shown by Figure 38 (b). Obviously the increase of the energy

barriers is much smaller compared to the islands with increasing elongation along $[1\bar{1}0]$ (factor of ten). However, since the length of the domain wall is kept constant in this case, one would expect the energy barrier to be constant as well. The energy barrier increasing with $N_{[001]}$ can be explained by a significant correlation between the magnetic moments of the island. The enhanced thermal fluctuations at the [001] ends lead to an enhanced fluctuation inside the wire, as indicated by the fluctuation maps in Figure 36, which consequently leads to a reduction of the domain wall energy. Figure 36 shows that this effect is larger for shorter islands compared to the longer islands. With increasing elongations of the islands along [001] the correlations between the [001] ends and the center of the wire decrease, which results in the increase of the energy barrier. For sufficiently large elongations the [001] ends of the island and it's center become uncorrelated and the energy barrier should become constant.

6.2.4 The Arrhenius pre-factor

Looking at the pre-factor of the Arrhenius function in equation (50) one finds it strongly depending on the system's geometry, shown by Figure 39. The pre-factor

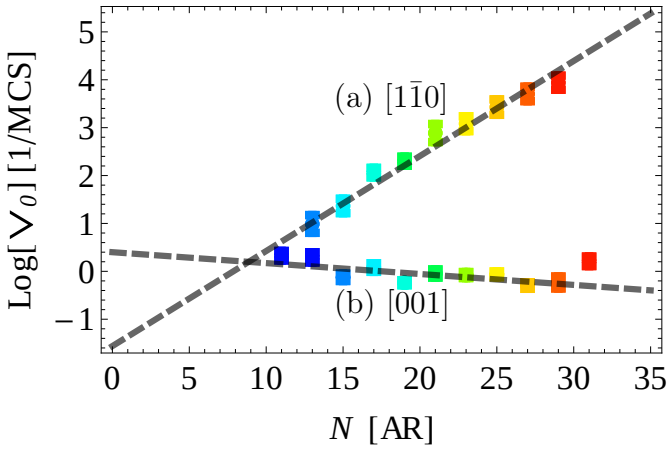

Figure 39: The Arrhenius pre-factor ν_0 as a function of the elongation of the islands: In (a) shown for the islands elongated along $[1\bar{1}0]$ and in (b) for the islands elongated along [001]. The color scale corresponds to the system sizes $L = N_{[1\bar{1}0]} \times N_{[001]}$ and varies from small in blue to large in red. The gray dashed lines are linear fits to the data points.

can be interpreted as the number of attempts to switch the magnetization and is, therefore, often referred to as *attempt frequency* in literature. The geometry dependency of the pre-factor arises due to the anisotropic orientation of the domain walls in Fe/W(110) nanoislands. ν_0 must be crucially depending on $N_{[1\bar{1}0]}$, as

with increasing $N_{[1\bar{1}0]}$ the number of nucleation sites and, therefore, the number of nucleation attempts increases. This assumption is confirmed by the simulated attempt frequency ν_0, shown in Figure 39 (a): ν_0 increases with increasing elongation along $[1\bar{1}0]$.

For the islands elongated along [001] the attempt frequency slightly decreases with increasing $N_{[001]}$, shown in Figure 39 (b). In this case, the number of nucleation sites is constant for all elongations along [001], hence, one would rather expect a constant pre-factor. Again, this finding is due to the correlations of the magnetic moments inside the wire with the moments at the [001] ends. Because the energy barrier increases for increasing $N_{[001]}$, the total number of switching attempts must decrease. Note, that the influence of the elongation along [001] on the attempt frequency is rather small in comparison to the elongation along $[1\bar{1}0]$, as clear from Figure 39.

The next section gives additional insights into the temperature and size dependency of the switching rates.

6.3 Additional analysis of the superparamagnetic switching

6.3.1 Switching rates at a constant temperature

To get additional insights into the superparamagnetic switching behavior of the simulated islands, Figure 40 shows a logarithmic plot of the switching rates as a function of the number of atomic rows along $[1\bar{1}0]$ and [001] at a constant temperature in the superparamagnetic temperature regime. This plot corresponds to a vertical cut at $\beta = 1.6\ k_\mathrm{B}/J$ of Figure 37. The plot shows the switching rates ν decreasing for increasing $N_{[1\bar{1}0]}$ as well as for increasing $N_{[001]}$. The switching rates are naturally directly correlated with the energy barrier of the magnetization reversal, hence, the switching rates in the superparamagnetic temperature regime decrease with increasing energy barrier. For an increasing elongation along [001] (the direction of the domain wall propagation) an additional decrease of the switching rates can be expected, which is due to the stochastic nature of the domain wall propagation in a system without external pressure. A decrease of the switching rates for increasing elongation along [001] can be described by the random walk theory, as presented in [9, 84]. If one considers a domain wall propagating through the nanoisland as a quasiparticle, moving forward and backward is energetically degenerate, as no external pressure exists. Following the random walk theory for a particle moving along a line with absorbing ends [69], the mean distance covered

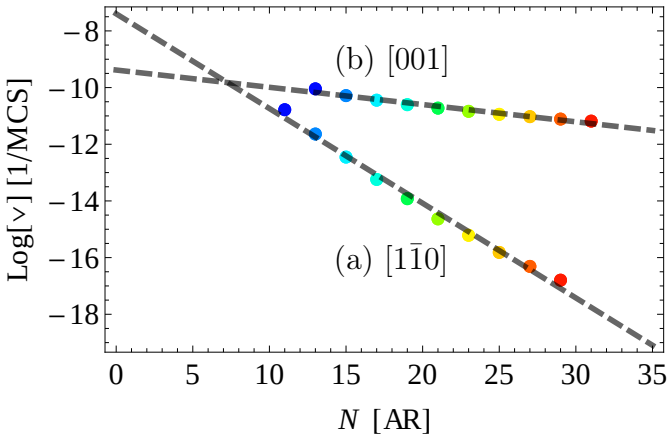

Figure 40: Logarithmic plot of the switching rates at a constant inverse temperature of $\beta = 1.6\ k_B/J$, as a function of the elongation of the islands. The color scale corresponds to the system sizes $L = N_{[1\bar{1}0]} \times N_{[001]}$ and varies from small in blue to large in red. The gray dashed lines are linear fits to the data points.

after n steps scales with $\sqrt{n}$. Thus, the probability of a domain wall successfully propagating from one end of the island to the other decreases with increasing $N_{[001]}$, as depicted in Figure 41. With increasing elongation of the islands the probabil-

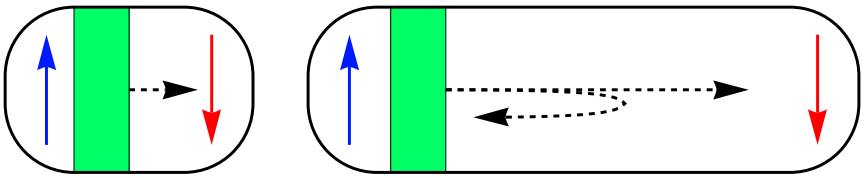

Figure 41: Sketch of the propagation of a domain wall in elongated nanoislands.

ity that the domain wall returns to its nucleation site and annihilates there, with no net magnetization reversal, increases. This behavior additionally reduces the switching rates ν when increasing $N_{[001]}$ and keeping $N_{[1\bar{1}0]}$ constant. Hence, for larger elongations, above which the energy barrier stays constant, the switching rates will still decrease with increasing elongation along [001].

6.3.2 Defining a characteristic switching rate and temperature?

When looking at the logarithmic switching rates as a function of the inverse temperature extrapolated up to $\beta \to 0$, a crossing point at $\beta \approx 0.6\ k_B/J$ (vertical solid gray line) is striking, see Figure 42. At that temperature all islands of different size and shape switch their magnetization at a constant rate of about 0.02 1/MCS (lifetime $\tau \approx 50$ MCS, horizontal solid gray line). Note, that for elongated is-

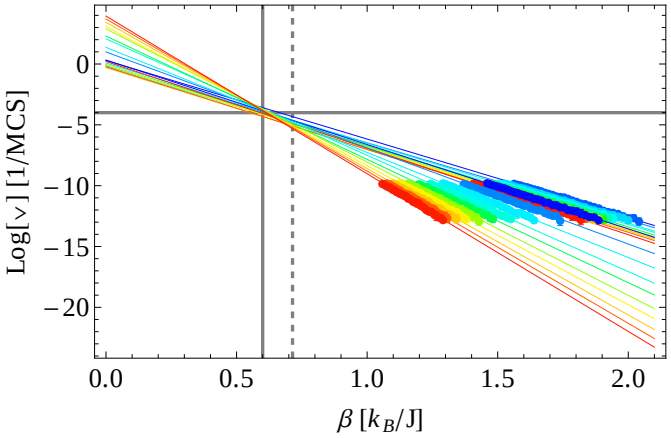

Figure 42: Logarithmic plot of the switching frequencies ν as a function of the inverse temperature β for different system sizes. The color scale corresponds to the island's size $L = N_{[1\bar{1}0]} \times N_{[001]}$ and is blue for small islands and red for large islands.

lands along [001] with a constant $N_{[1\bar{1}0]}$ this crossing point cannot be observed that clearly, as here all the Arrhenius fits for the different island elongations have a similar slope and the fits run very close to each other and in parallel.

From the simulations of islands with different energy barriers, the crossing point can be determined. Simulations of various systems revealed such a crossing point, namely: simulations for an isotropic square lattice with Ising spins, for an isotropic Heisenberg system with sc or bcc lattice, and the simulation of anisotropic as well as isotropic Heisenberg moments with different easy-axis anisotropies. For each of the different systems, the crossing point lies at a different temperature, which seems to be characteristic for the system properties. At this temperature, which will be denoted as *characteristic temperature* T^c in the following, islands of different sizes and shape (but with the same magnetic properties) switch at a constant frequency, which will be denoted as the *characteristic frequency* ν_c in the following. Note, that the characteristic temperature must be seen as a parameter which is a consequence of the physical properties of the system in the analyzed temperature region. It does not give any insights or properties of the system at the characteristic temperature, which becomes clear when looking at the inverse Curie temperature of the infinite system which lies below T^c (vertical dashed gray line).

It might be possible to classify a system of certain magnetic properties by the characteristic temperature and frequency. The simulations show that the characteristic parameters depend on the energy constants and the lattice used. Furthermore, one can expect the dimensionality and the geometries to determine the

characteristic parameters. In addition, the temperature region used for the analysis of the magnetization switching might influence the parameters, especially if the switching mechanism changes, for instance, from domain wall nucleation and propagation to multi-droplet nucleation [107, 109, 110]. An extensive study would be necessary to categorize the systems. However, such a study would not necessarily reveal additional benefits over existing classifications like the *finite size scaling* theory [94, 111]. As such a study is behind the scope of this work, only the discovery of such characteristics shall be noted here.

The following section presents a simulation of the influence of a spin-polarized current, induced by an STM tip, on the superparamagnetic switching of ferromagnetic nanoislands consisting of about 100 atoms.

6.3.3 Current-induced magnetization switching

In section 3 the influence of a spin-current on the magnetization switching in a nanowire has been investigated theoretically. Since in that study the applied current has been too small to directly switch the magnetization of the magnetic bit, a domain wall has been utilized in order to switch the magnetization of the bit. However, when decreasing the system size until the nanoislands start switching superparamagnetically (like in the present chapter) such an island can be switched directly by an SP-STM tip, as shown experimentally by Stefan Krause *et al.* [112]. Depending on the polarization of the SP-STM tip and the applied current, a nanoisland has been forced to switch its magnetization. The transferred torque of a spin-current discussed in section 3.1.4 on a superparamagnetically switching island leads to a favored magnetization direction, hence, to a higher population of one of the two states, spin-up or spin-down.

Figure 43 shows Monte Carlo simulations of the magnetization switching inside the superparamagnetic temperature regime with a spin-current applied. The asymmetry in the population probability is in very good agreement with experiment [112]. In experiment as well as in the simulation, the SP-STM tip has been placed in the center of one nanoisland measuring the magnetization switching with different applied currents. The polarization of the spin-current obviously leads to a higher population of the spin-up state. Applying this method to a thermally stable magnetic bit, it allows to control the orientation of that magnetic bit.

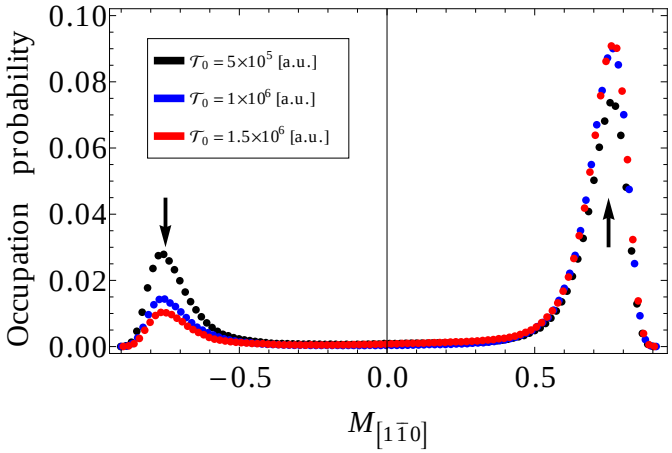

Figure 43: Monte Carlo simulation of the probability to find the nanoisland in a state with a certain easy-axis magnetization $M_{[1\bar{1}0]}$ for three different spin-currents applied. The x axis shows the normalized easy-axis magnetization. The peaks for negative magnetization correspond to the spin-down states and the peaks for positive values to the spin-up states.

6.4 Summary and Conclusion

The presented study on the thermally induced magnetization reversal of atomic-scale monolayer iron nanoislands provided insights into the microscopic processes of magnetization reversal via domain wall nucleation and propagation. The switching rates and also the Arrhenius pre-factor and energy barrier have been found to be strongly dependent on the morphology of the simulated systems. The studies help to systematically tailor future magnetic nano-objects that hinder or favor magnetization reversal, which is important for the development of new types of data storage media or magnetic sensors at the nanoscale.

It has been suggested, that from the simulation of the superparamagnetic switching behavior a temperature can be defined, which is characteristic for the magnetic properties of the island inside the analyzed temperature region. In order to prove this finding experimentally, one needs to create nanoislands with exact geometries, which is a very time-consuming task. A promising method to create such precisely defined samples is single-atom manipulation [113–115].

Eventually, the influence of a spin-polarized tunneling current (induced by an SP-STM tip) on the superparamagnetic switching of the nanoislands has been presented. The application of such a spin-current allows to control the magnetization of a single nanoisland.

7 Conclusions and Perspectives

The present thesis investigates by means of classical Monte Carlo simulations the magnetic properties of monolayer ferromagnetic nanoparticles. The properties of the systems studied are comparable to Fe/W(110) and could be employed in future storage or logic devices.

The manipulation of a narrow domain wall in a ferromagnetic nanowire utilizing a localized spin-current of an STM has been studied theoretically. The results suggest that it is possible to manipulate a single domain wall in a hard magnetic nanowire, like Fe/W(110), using an SP-STM. The total magnetization of a nanowire has been exactly controlled in the simulation by the manipulation of a single domain wall. Such a nanowire could be used to build a logic device, whose operation depends on the exact position of the domain wall. The simulations reveal that a tip with a magnetization parallel to the domain wall magnetization is best to control a domain wall, because such a tip-wall alignment allows to move the domain wall in both directions along the wire.

Additional simulations including magnetic defects showed that defects can lead to the pinning of the domain wall and, thereby, prevent a successful domain wall manipulation. The domain wall pinning at such defects could be the reason why an experimental realization of the controlled domain wall manipulation by means of an SP-STM tip has not been possible so far. Surprisingly, the simulations including defects allowed to resolve the Peierls potential, which was not possible for the defect free wire. The reason why it has been possible to map the Peierls potential in the simulation was the repeated pinning and depinning of the domain wall at the defects, which led to an oscillation of the external pressure. Hence, it has been found that the external pressure induced by the moving SP-STM tip is not constant during manipulation, it varied between 40 mT and 66 mT and allowed to map several energy states of the domain wall during a single manipulation trial. In order to build and optimize the cost-of-ownership of a real storage application based upon the controlled manipulation of a single domain wall a lot of factors have to be weighted up. Therefore, a theoretical investigation would be helpful which studies the interplay between the depinning field, the applied current or field, and the temperature in a realistic setup. These three parameters could be systematically varied in a simulation, hopefully revealing an applicable set of these parameters.

Before the superparamagnetic switching of ferromagnetic nanoislands could

be investigated, first the critical temperatures of the superparamagnetic regime had been defined. It was demonstrated that a meaningful definition of the Curie temperature of a finite spin system can be given that relies on the analysis of a suitably defined average spin correlation function, denoted as connected correlation function. It has been shown that the concept can be applied to different one-, two-, and three-dimensional classical spin models and that the reduced Curie temperature $T_c(L)$ can be extracted with an accuracy that even allows to determine a shift exponent. Further, it has been demonstrated that the blocking temperature scale is accessible with a Monte Carlo approach by performing an incomplete statistical average. A sharp jump is visible in the average spin-correlation function at $T_b(L)$. However, the blocking temperature is only defined with respect to an observation time (a finite number of MCSs) and therefore represents only a relative quantity.

After the critical temperatures have been defined the magnetization dynamics of such nanoislands have been studied in the superparamagnetic temperature regime for different temperatures and for varying sizes and shapes. The stability against thermal excitations for Fe/W(110) nanoislands has been found to depend not only on the size of the island but also on its shape. The reason for that is the switching mechanism involved: domain wall nucleation and propagation. The thermal stability depends on the energy needed for a successful domain wall nucleation and this nucleation energy in turn depends on the shape of the island, which is due to the anisotropic domain wall orientation in monolayer Fe/W(110) nanoislands. The studies help to systematically tailor future magnetic nano-objects that hinder or favor magnetization reversal, which is useful for the development of new types of data storage media or magnetic sensors at the nanoscale. The direct control of the magnetization of hard-magnetic nanoislands has been realized experimentally [112, 115] and could be used to replace the layer of granulated material of commodity HDDs with pre-patterned magnetic islands, which then could be addressed by a locally induced spin-current.

Finally, it is worth to mention - as shown in this thesis - that a Monte Carlo simulation is a powerful tool to investigate not only the magnetization dynamics of single domain nanoislands but also to get insights into the dynamics of domain wall propagation, which is usually studied by means of spin-dynamic simulations.

Bibliography

[1] C. Walter. Kryder's Law. *Scientific American*, 293:32–33, 2005.

[2] R. E. Fontana, S. R. Hetzler, and G. Decad. Technology Roadmap Comparisons for TAPE, HDD, and NAND Flash: Implications for Data Storage Applications. *Magnetics, IEEE Transactions on*, 48(5):1692–1696, 2012.

[3] T. Coughlin. When Will We See Higher Capacity Hard Disk Drives? `http://www.forbes.com/sites/tomcoughlin/2013/09/07/when-will-we-see-higher-capacity-hard-disk-drives/`, Sep 2013.

[4] HGST. 6TB 3.5-inch Helium Platform Enterprise Hard Drive. `http://www.hgst.com/hard-drives/enterprise-hard-drives/enterprise-sas-drives/ultrastar-he6`, 2013.

[5] M. L. Néel. *Ann. Géophys.*, 5:99, 1949.

[6] W. F. Brown. Thermal Fluctuations of a Single-Domain Particle. *Physical Review*, 130(5):1677–1686, 1963.

[7] R. F. Service. Is the Terabit Within Reach. *Science*, 314:1868, Dec 2006.

[8] S. A. Nepijko and R. Wiesendanger. Size Dependence of the Curie Temperature of Separate Nickel Particles Studied by Interference Electron Microscopy. *Europhys. Lett.*, 31:567, Sep 1995.

[9] Stefan Krause. *Thermal and Current-Induced Magnetization Switching of Fe/W(110) Nanoislands Investigated by Spin-Polarized Scanning Tunneling Microscopy.* dissertation, University of Hamburg, 2008.

[10] D. P. Landau. Finite-size behavior of the Ising square lattice. *Phys. Rev. B*, 13:2997–3011, Apr 1976.

[11] S. S. P. Parkin, M. Hayashi, and L. Thomas. Magnetic Domain-Wall Racetrack Memory. *Science*, 320:190–4, 04 2008.

[12] M. Kläui, D. Ilgaz, L. Heyne, J.-S. Kim, O. Boulle, C. Schieback, F. Zinser, S. Krzyk, M. Fonin, U. Rüdiger, D. Backes, L. J. Heyderman, T. O. Mentes, and A. Locatelli. Concepts for Domain Wall Motion in Nanoscale Ferromagnetic Elements due to Spin Torque and in Particular Oersted Fields. *J. Magn.*, 14:53–61, 2009.

[13] S. Allende, D. Altbir, E. Salcedo, M. Bahiana, and J. P. Sinnecker. Propagation of transverse domain walls in homogeneous magnetic nanowires. *J. Appl. Phys.*, 104:013907, Jan 2008.

[14] A. Imre, G. Csaba, V. Metlushko, G. H. Bernstein, and W. Porod. Controlled domain wall motion in micron-scale permalloy square rings. *Physica E*, 19:240, 2003.

[15] T. Yamaoka, K. Watanabe, Y. Shirakawabe, K. Chinone, E. Saitoh, and H. Miyajima. Observations of Single Magnetic Domain Wall in Nanomagnet by Magnetic Force Microscopy. *Jpn. J. Appl. Phys.*, 45:2230, 2006.

[16] J. C. Slonczewski. Current-driven excitation of magnetic multilayers. *J. Magn. Magn. Mat.*, 159:L1–L7, Jun 1996.

[17] L. Berger. Emission of spin waves by a magnetic multilayer traversed by a current. *Phys. Rev. B*, 54:9353–9358, Oct 1996.

[18] J. Kötzler, D. Görlitz, M. Kurfiß, L. von Sawilski, and E. Y. Vedmedenko. Vortex fluctuations and freezing of dipolar-coupled granular moments in thin ferromagnetic films. *Phys. Rev. B*, 73:224425, Jun 2006.

[19] Thim Stapelfeldt. Superparamagnetic Switching of Two-dimensional Magnetic Islands Studied by Monte Carlo Simulation. Diploma thesis, University of Hamburg, 2008.

[20] W. Nolting. *Grundkurs Theoretische Physik 6, Statistische Physik*. Springer, 2007.

[21] M. E. J. Newmann. *Monte Carlo Methods in Statistical Physics*. Clarendon Press, 1999.

[22] F. Schwabl. *Statistische Mechanik*. Springer, 2004.

[23] F. Reif. *Fundamentals of statistical and thermal physics*. McGraw-Hill Book Company, 1965.

[24] K. Huang. *Statistical Mechanics*. Wiley, 1987.

[25] M. E. Fischer and A. E. Ferdinand. INTERFACIAL, BOUNDARY, AND SIZE EFFECTS AT CRITICAL POINTS. *Physical Review Letters*, 19(4):169, 1967.

[26] M. E. Fisher and M. N. Barber. Scaling Theory for Finite-Size Effects in the Critical Region. *Phys. Rev. Lett.*, 28:1516–1519, Jun 1972.

[27] D. P. Landau. Finite-size behavior of the simple-cubic Ising lattice. *Physical Review B*, 14(1):255, 1976.

[28] N. Metropolis, A. W. Rosenbluth, M. N. Rosenbluth, A. H. Teller, and E. Teller. Equation of State Calculations by Fast Computing Machines. *Journal of Chemical Physics*, 21(6):1087, 1953.

[29] W. H. Press, S. A. Teukolsky, W. T. Vetteling, and B. B. Flannery. *Numerical Recipes - The Art of Scientific Computing*. Cambridge University Press, 2007.

[30] T. Stapelfeldt, R. Wieser, E. Y. Vedmedenko, and R. Wiesendanger. Domain Wall Manipulation with a Magnetic Tip. *Phys. Rev. Lett.*, 107:027203, Jul 2011.

[31] N. Weber, K. Wagner, H. J. Elmers, J. Hauschild, and U. Gradmann. Nanoscale spatial switching of magnetic anisotropy in pseudomorphic Fe(110) on W(110). *Phys. Rev. B*, 55:14121–14124, Jun 1997.

[32] P. J. Jensen, S. Knappmann, W. Wulfhekel, and H. P. Oepen. Anisotropic susceptibility of ferromagnetic ultrathin co films on vicinal cu. *Phys. Rev. B*, 67:184417, May 2003.

[33] J. Hauschild, U. Gradmann, and H. J. Elmers. Perpendicular magnetization and dipolar antiferromagnetism in double layer nanostripe arrays of Fe(110) on W(110). *J. Appl. Phys.*, 72:3211, Jan 1998.

[34] O. Pietzsch, A. Kubetzka, M. Bode, and R. Wiesendanger. Real-Space Observation of Dipolar Antiferromagnetism in Magnetic Nanowires by Spin-Polarized Scanning Tunneling Spectroscopy. *Phys. Rev. Lett.*, 84:5212–5215, May 2000.

[35] M. Pratzer, H. J. Elmers, M. Bode, O. Pietzsch, A. Kubetzka, and R. Wiesendanger. Atomic-Scale Magnetic Domain Walls in Quasi-One-Dimensional Fe Nanostripes. *Phys. Rev. Lett.*, 87:127201, Aug 2001.

[36] M. Pratzer and H. J. Elmers. Domain wall energy in quasi-one-dimensional Fe/W(110) nanostripes. *Phys. Rev. B*, 67:094416, Mar 2003.

[37] O. Pietzsch, A. Kubetzka, M. Bode, and R. Wiesendanger. Observation of Magnetic Hysteresis at the Nanometer Scale by Spin-Polarized Scanning Tunneling Spectroscopy. *Science*, 292:2053, Oct 2001.

[38] A. Kubetzka, M. Bode, O. Pietzsch, and R. Wiesendanger. Spin-Polarized Scanning Tunneling Microscopy with Antiferromagnetic Probe Tips. *Phys. Rev. Lett.*, 88:057201, Jan 2002.

[39] M. Bode, S. Heinze, A. Kubetzka, O. Pietzsch, X. Nie, G. Bihlmayer, S. Blügel, and R. Wiesendanger. Magnetization-Direction-Dependent Local Electronic Structure Probed by Scanning Tunneling Spectroscopy. *Phys. Rev. Lett.*, 89:237205, Nov 2002.

[40] M. Bode, A. Kubetzka, S. Heinze, O. Pietzsch, R. Wiesendanger, M. Heide, X. Nie, G. Bihlmayer, and S. Blügel. Spin–orbit induced local band structure variations revealed by scanning tunnelling spectroscopy. *J. Phys.: Cond. Matter*, 24:679–692, Oct 2002.

[41] A. Kubetzka, O. Pietzsch, M. Bode, and R. Wiesendanger. Spin-polarized scanning tunneling microscopy study of 360° walls in an external magnetic field. *Phys. Rev. B*, 67:020401, Jan 2003.

[42] A. Lehnert, S. Dennler, P. Błoński, S. Rusponi, M. Etzkorn, G. Moulas, P. Bencok, P. Gambardella, H. Brune, and J. Hafner. Magnetic anisotropy of Fe and Co ultrathin films deposited on Rh(111) and Pt(111) substrates: An experimental and first-principles investigation. *Phys. Rev. B*, 82:094409, Sep 2010.

[43] H. J. Elmers, J. Hauschild, and U. Gradmann. Morphology and magnetism of Fe on vicinal W(110) surfaces with different step orientation. *Journal of Magnetism and Magnetic Materials*, 221(1-2):219 – 223, 2000. Proceedings of the 3rd Euroconference on Magnetic Properties of Fine Particles and their Relevance to Materials Science.

[44] M. Bode, A. Wachowiak, J. Wiebe, A. Kubetzka, M. Morgenstern, and R. Wiesendanger. Thickness dependent magnetization states of Fe islands on W(110): From single domain to vortex and diamond patterns. *Appl. Phys. Lett.*, 84(6):948, 2004.

[45] A. T. Costa, R. B. Muniz, J. X. Cao, R. Q. Wu, and D. L. Mills. Magnetism of an fe monolayer on w(110). *Phys. Rev. B*, 78:054439, Aug 2008.

[46] R. B. Muniz and D. L. Mills. Theory of spin excitations in Fe(110) monolayers. *Phys. Rev. B*, 66:174417, Nov 2002.

[47] X. Qian and W. Hübner. First-principles calculation of structural and magnetic properties for Fe monolayers and bilayers on W(110). *Phys. Rev. B*, 60:16192–16197, Dec 1999.

[48] E. Y. Vedmedenko, A. Kubetzka, K. von Bergmann, O. Pietzsch, M. Bode, J. Kirschner, H. P. Oepen, and R. Wiesendanger. Domain Wall Orientation in Magnetic Nanowires. *Phys. Rev. Lett.*, 92:077207, Feb 2004.

[49] E. Y. Vedmedenko. Influence of the lattice discreteness on magnetic ordering in nanostructures and nanoarrays. *phys. stat. sol. (b)*, 255:1133–1165, 2007.

[50] H. R. Hilzinger and H. Kronmüller. Spin Configuration and Intrinsic Coercive Field of Narrow Domain Walls in Co5R-Compounds. *phys. status sol (b)*, 54:593–604, Dec 1972.

[51] R. Wiesendanger. Spin mapping at the nanoscale and atomic scale. *Rev. Mod. Phys.*, 81:1495, 2009.

[52] J. Tersoff and D. R. Hamann. Theory and Application for the Scanning Tunneling Microscope. *Phys. Rev. Lett.*, 50:1998–2001, Jun 1983.

[53] D. Wortmann, S. Heinze, Ph. Kurz, G. Bihlmayer, and S. Blügel. Resolving Complex Atomic-Scale Spin Structures by Spin-Polarized Scanning Tunneling Microscopy. *Phys. Rev. Lett.*, 86:4132–4135, Apr 2001.

[54] S. Zhang and Z. Li. Roles of Nonequilibrium Conduction Electrons on the Magnetization Dynamics of Ferromagnets. *Phys. Rev. Lett.*, 93:127204, Sep 2004.

[55] M. Kläui. Head-to-head domain walls in magnetic nanostructures. *J. Phys.: Cond. Matter*, 20:313001, 2008.

[56] A. Thiaville and Y. Nakatani. *Domain-Wall Dynamics in Nanowires and Nanostrips*. Springer New York, 2006.

[57] R. Wieser, E. Y. Vedmedenko, P. Weinberger, and R. Wiesendanger. Current-driven domain wall motion in cylindrical nanowires. *Phys. Rev. B*, 82:144430, Oct 2010.

[58] L. D. Landau and E. Lifshitz. . *Phys. Z. Sowjetunion*, 8:153, 1935.

[59] A. Thiaville, Y. Nakatani, J. Miltat, and Y. Suzuki. Micromagnetic understanding of current-driven domain wall motion in patterned nanowires. *Europhys. Lett*, 69:990–996, Mar 2005.

[60] R. Wieser, E. Y. Vedmedenko, and R. Wiesendanger. Domain wall motion damped by the emission of spin waves. *Phys. Rev. B*, 81:024405, Jan 2010.

[61] T. Egami and C. D. Graham. Domain Walls in Ferromagnetic Dy and Tb. *J. Appl. Phys*, 42:1299, Mar 1971.

[62] R. Herz and H. Kronmüller. MAGNETIC AFTER-EFFECT IN RARE-EARTH METALS WITH NARROW DOMAIN WALLS. *J. Magn. Magn. Mat.*, 4:36–39, 1977.

[63] H. Kronmüller and M Fähnle. *Micromagnetism and the microstucture of ferromagnetic solids*. Cambridge University Press, 2003.

[64] R. E. Peierls. The size of a dislocation. *Proc. Phys. Soc.*, 52:34–37, 1940.

[65] F. R. N. Nabarro. Dislocations in a simple cubic lattice. *Proc. Phys. Soc.*, 59:256, 1947.

[66] H. R. Kolar, J. C. H. Spence, and H. Alexander. Observation of Moving Dislocation Kinks and Unpinning. *Phys. Rev. Lett.*, 77:4031–4034, Nov 1996.

[67] B. I. Ivlev and N. B. Kopnin. Flux creep and flux pinning in layered high-temperature superconductors. *Phys. Rev. Lett.*, 64:1828–1830, Apr 1990.

[68] K. S. Novoselov, A. K. Geim, S. V. Dubonos, E. W. Hill, and I. V. Grigorieva. Subatomic movements of a domain wall in the Peierls potential. *Letters to Nature*, 426:812–816, 2003.

[69] E. Gert. Atomic Displacements in One and TwoDimensional Diffusion. *J. Chem. Phys.*, 44:1050, 1966.

[70] A. K Tagantsev, E. L. Cross, and J. Fousek. *Domains in Ferroic Crystal and Thin Films*. Springer New York, 2010.

[71] M. Jullière. TUNNELING BETWEEN FERROMAGNETIC FILMS. *Phys. Lett.*, 54:225, 1975.

[72] K. S. Novoselov. *Development and applications of mesoscopic hall microprobes*. dissertation, Radboud University Nijmegen, Nov 2004.

[73] H. Kronmüller. Microstructure and Micromagnetism. *AIP Conf. Proc.*, 10:1006, 1973.

[74] H. R. Hilzinger. Applied Physics 9. 260:253–260, 1977.

[75] S. Krause, L. Berbil-Bautista, T. Hänke, F. Vonau, M. Bode, and R. Wiesendanger. Consequences of line defects on the magnetic structure of high anisotropy films: Pinning centers on Dy/W(110). *Europhys. Lett.*, 76:637–643, Nov 2006.

[76] E. Martinez. The stochastic nature of the domain wall motion along high perpendicular anisotropy strips with surface roughness. *J. Phys.: Cond. Matter*, 24:024206, Dec 2012.

[77] C. Burrowes, A. P. Mihai, D. Ravelosona, J. V. Kim, C. Chappert, L. Vila, A. Marty, Y. Samson, F. Garcia-Sanchez, L. D. Buda-Prejbeanu, I. Tudosa, E. E. Fullerton, and J. P. Attané. Non-adiabatic spin-torques in narrow magnetic domain walls. *Nature Phys.*, 6:17, Nov 2009.

[78] J. M. Shaw, M. Olsen, J. W. Lau, M. L. Schneider, T. J. Silva, O. Hellwig, E. Dobisz, and B. D. Terris. Intrinsic defects in perpendicularly magnetized multilayer thin films and nanostructures. *Phys. Rev. B*, 82:144437, Oct 2010.

[79] T. Thomson, G. Hu, and B. D. Terris. Intrinsic Distribution of Magnetic Anisotropy in Thin Films Probed by Patterned Nanostructures. *Phys. Rev. Lett.*, 96:257204, Jun 2006.

[80] P. Krone, D. Makarov, T. Schrefl, and M. Albrecht. Effect of the anisotropy distribution on the coercive field and switching field distribution of bit patterned media. *J. Appl. Phys.*, 106:103913, Aug 2009.

[81] T. Gerhardth, A. Drews, and G. Meier. Controlled pinning and depinning of domain walls in nanowires with perpendicular magnetic anisotropy. *J. Phys.: Cond. Matter*, 24:024208, Dec 2011.

[82] D. A. Huse and C. L. Henley. Pinning and Roughening of Domain Walls in Ising Systems Due to Random Impurities. *Phys. Rev. Lett.*, 54:2708–2711, Jun 1985.

[83] H. Hauser. Energetic model of ferromagnetic hysteresis. *Journal of Applied Physics*, 75(5):2584, 1994.

[84] S. Krause, G. Herzog, T. Stapelfeldt, L. Berbil-Bautista, M. Bode, E. Y. Vedmedenko, and R. Wiesendanger. Magnetization Reversal of Nanoscale Islands: How Size and Shape Affect the Arrhenius Prefactor. *Phys. Rev. Lett.*, 103:127202, Sep 2009.

[85] S. Rusponi, T. Cren, N. Weiss, M. Epple, P. Buluschek, L. Claude, and H. Brune. The remarkable difference between surface and step atoms in the magnetic anisotropy of two-dimensional nanostructures. *Nature Mat.*, 2:546–551, Aug 2003.

[86] P. Ferriani, C. Lazo, and S. Heinze. Origin of the spin polarization of magnetic scanning tunneling microscopy tips. *Phys. Rev. B*, 82:054411, Aug 2010.

[87] A. K. Geim, S. V. Dubonos, J. G. S. Lok, I. V. Grigorieva, J. C. Maan, L. T. Hansen, and P. E. Lindelof. Ballistic Hall micromagnetometry. *Appl. Phys. Lett.*, 71:2379, Aug 1997.

[88] V. D. Nguyen, L. Vila, P. Laczkowski, A. Marty, T. Faivre, and J. P. Attané. Detection of Domain-Wall Position and Magnetization Reversal in Nanostructures Using the Magnon Contribution to the Resistivity. *Phys. Rev. Lett.*, 107:136605, Sep 2011.

[89] Boris Wolter, Yasuo Yoshida, André Kubetzka, Saw-Wai Hla, Kirsten von Bergmann, and Roland Wiesendanger. Spin Friction Observed on the Atomic Scale. *Phys. Rev. Lett.*, 109:116102, Sep 2012.

[90] M. Hayashi, L. Thomas, C. Rettner, R. Moriya, X. Jiang, and S. S. P. Parkin. Dependence of Current and Field Driven Depinning of Domain Walls on Their Structure and Chirality in Permalloy Nanowires. *Phys. Rev. Lett.*, 97:207205, Nov 2006.

[91] O. Boulle, J. Kimling, P. Warnicke, M. Kläui, U. Rüdiger, G. Malinowski, H. J. M. Swagten, B. Koopmans, C. Ulysse, and G. Faini. Nonadiabatic Spin Transfer Torque in High Anisotropy Magnetic Nanowires with Narrow Domain Walls. *Phys. Rev. Lett.*, 101:216601, Nov 2008.

[92] E. Y. Vedmedenko, N. Mikuszeit, T. Stapelfeldt, R. Wieser, M. Potthoff, Lichtenstein A. I., and R. Wiesendanger. Spin-spin correlations in ferromagnetic nanosystems. *Eur. Phys. J. B*, 80:331–336, Mar 2011.

[93] K. Binder. Application of Monte Carlo methods to statistical physics. *Rep. Prog. Phys.*, 60:487, 1997.

[94] M. E. Fisher. The renormalization group in the theory of critical behavior. *Rev. Mod. Phys.*, 46:597–616, Oct 1974.

[95] T. T. Wu, B. M. McCoy, C. A. Tracy, and E. Barouch. Spin-spin correlation functions for the two-dimensional Ising model: Exact theory in the scaling region. *Phys. Rev. B*, 13:316–374, Jan 1976.

[96] D. A. Dimitrov and G. M. Wysin. Magnetic properties of superparamagnetic particles by a Monte Carlo method. *Phys. Rev. B*, 54:9237–9241, Oct 1996.

[97] M. Campanino, D. Ioffe, and Y. Velenik. Rigorous nonperturbative Ornstein-Zernike theory for Ising ferromagnets. *Europhys. Lett.*, 62:182–188, Apr 2003.

[98] M. N. Barber. *Phase Transitions and Critical Phenomena.* Springer New York, 2006.

[99] Ò. Iglesias and A. Labarta. Finite-size and surface effects in maghemite nanoparticles: Monte Carlo simulations. *Phys. Rev. B*, 63:184416, Apr 2001.

[100] D. L. Mills. Surface Effects in Magnetic Crystals near the Ordering Temperature. *Phys. Rev. B*, 3:3887–3895, Jun 1971.

[101] K. Binder and P. C. Hohenberg. Phase Transitions and Static Spin Correlations in Ising Models with Free Surfaces. *Phys. Rev. B*, 6:3461–3487, Nov 1972.

[102] P. Kumar. Magnetic phase transition at a surface: Mean-field theory. *Phys. Rev. B*, 10:2928–2933, Oct 1974.

[103] T. C. Lubensky and M. H. Rubin. Critical phenomena in semi-infinite systems. I. ϵ expansion for positive extrapolation length. *Phys. Rev. B*, 11:4533–4546, Jun 1975.

[104] R. Wiesendanger. http://www.nanoscience.de/nanojoom/index.php/en/. `http://www.nanoscience.de/nanojoom/index.php/en/`.

[105] D. Hinzke and U. Nowak. Magnetization switching in a Heisenberg model for small ferromagnetic particles. *Phys. Rev. B*, 58:265–272, Jul 1998.

[106] U. Nowak and D. Hinzke. Magnetization switching in small ferromagnetic particles: Nucleation and coherent rotation. *J. Appl. Phys.*, 85:4337, Apr 1999.

[107] D. Hinzke and U. Nowak. Magnetic relaxation in a classical spin chain. *Phys. Rev. B*, 61:6734–6740, Mar 2000.

[108] Gabriela Herzog. Strominduziertes Schalten magnetischer Nanoinseln auf W(110) mittels spinpolarisierter Rastertunnelmikroskopie. Diploma thesis, University of Hamburg, 2007.

[109] H.-B. Braun. Thermally Activated Magnetization Reversal in Elongated Ferromagnetic Particles. *Phys. Rev. Lett.*, 71:3557–3560, Nov 1993.

[110] H.-B. Braun. Statistical mechanics of nonuniform magnetization reversal. *Phys. Rev. B*, 50:16501–16521, Dec 1994.

[111] A. Aharony and M. E. Fisher. Nonlinear scaling fields and corrections to scaling near criticality. *Phys. Rev. B*, 27:4394–4400, Apr 1983.

[112] S. Krause, L. Berbil-Bautista, G. Herzog, M. Bode, and R. Wiesendanger. Current-Induced Magnetization Switching with a Spin-Polarized Scanning Tunneling Microscope. *Science*, 317:1537, Sep 2007.

[113] D. Serrate, P. Ferriani, Y. Yoshida, S.-W. Hla, M. Menzel, K. von Bergmann, S. Heinze, A. Kubetzka, and R. Wiesendanger. Imaging and manipulating the spin direction of individual atoms. *Nature Nanotechnology*, 5:350, May 2010.

[114] D. M. Eigler and E. K. Schweizer. Positioning single atoms with a scanning tunnelling microscope. *Nature*, 344:524–526, Apr 1990.

[115] A. A. Khajetoorians, B. Baxevanis, C. Hübner, T. Schlenk, S. Krause, T. O. Wehling, S. Lounis, A. Lichtenstein, D. Pfannkuche, J. Wiebe, and R. Wiesendanger. Current-Driven Spin Dynamics of Artificially Constructed Quantum Magnets. *Science*, 339:55–59, Jan 2013.

Publications

- K. Them, T. Stapelfeldt, E.Y. Vedmedenko, and R. Wiesendanger,*Non-equilibrium finite temperature dynamics of magnetic quantum systems: applications to spin-polarized scanning tunneling microscopy*, New Journ. Phys., **15**, 013009 (2013)
- R. Wieser, T. Stapelfeldt, E.Y. Vedmedenko, and R. Wiesendanger, *Manipulation of domain walls using a spin-polarized STM*, Europhys. Lett., **97**, 17009 (2012)
- T. Stapelfeldt, R. Wieser, E.Y. Vedmedenko, and R. Wiesendanger, *Domain Wall Manipulation with a Magnetic Tip*, Phys. Rev. Lett., **107**, 027203 (2011)
- E.Y. Vedmedenko, N. Mikuszeit, T. Stapelfeldt, R. Wieser, M. Potthoff, A.I. Lichtenstein and R. Wiesendanger, *Spin-spin correlations in ferromagnetic nanosystems*, Eur. Phys. J. B, **80**, 331 (2011)
- S. Krause, G. Herzog, T. Stapelfeldt, L. Berbil-Bautista, M. Bode, E.Y. Vedmedenko, and R. Wiesendanger, *Magnetization Reversal of Nanoscale Islands: How Size and Shape Affect the Arrhenius Prefactor*, Phys. Rev. Lett., **103**, 127202 (2009)

Talks and Posters

- 10.09.2012
  T. Stapelfeldt, R. Wieser, E.Y. Vedmedenko, and R. Wiesendanger, *Domain Wall Manipulation with a Magnetic Tip*, 6th International Conference on SPS and 4th International Workshop on SP-STM, Timmendorfer Strand (Germany)
- 30.03.2012
  T. Stapelfeldt, R. Wieser, E.Y. Vedmedenko, and R. Wiesendanger, *Domain Wall Manipulation with a Magnetic Tip*, 76th Spring Conference, Deutsche Physikalische Gesellschaft, Berlin (Germany)
- 23.08.2011
  T. Stapelfeldt, R. Wieser, E.Y. Vedmedenko, and R. Wiesendanger, *Domain Wall Manipulation with a Magnetic Tip*, European School on Magnetism, Targoviste (Romania)
- 25.01.2011
  T. Stapelfeldt, R. Wieser, E.Y. Vedmedenko, and R. Wiesendanger, *Manipulation of Magnetic Domain Walls with an STM Tip*, SFB 668 - Kolloquium, Hamburg (Germany)

- 16.03.2011
  T. Stapelfeldt, R. Wieser, E.Y. Vedmedenko, and R. Wiesendanger, *Domain Wall Manipulation with a Magnetic Tip*, 75th Spring Conference, Deutsche Physikalische Gesellschaft, Dresden (Germany)

- 27.03.2009
  T. Stapelfeldt, E.Y. Vedmedenko, S. Krause, G. Herzog, and R. Wiesendanger, *Superparamagnetic Switching of Two-dimensional Magnetic Islands Studied by Monte Carlo Simulation*, 73th Spring Conference, Deutsche Physikalische Gesellschaft, Dresden (Germany)

Acknowledgements

There are so many people I like to thank for their help and support or for walking along side with me, be it for short or long time periods.

- I thank my wife Anna, for her never ending love, advice and encouragement, I will always be in need of it.
- I thank Elena for her continuous advice, encouragement and, of course, for reviewing the manuscript over and over again.
- I thank Professor Roland Wiesendanger for giving me the opportunity to work in such an excellent research environment, with so many great people.
- I thank my flatmate Elif for her steady support and for all the cooking, which allowed me again and again to stay one more hour in front of my computer.
- I thank Robert, Bo, Kolja, David and Julian for making me feel good in our subgroup and beyond.
- I thank Stefan, Andi, Gaby, Annika und Johannes from Lab018 for all the nice experiments and discussion not only concerning superparamagnetism.
- I thank Alex and André for all the nice discussions and the good advices, even long before my diploma thesis.
- I thank Nikolai, in particular for introducing me into the infinite world of Mathematica. Even though, I still have the feeling I only scratched the surface of the Mathematica world, it tremendously helped me analyzing, visualizing, presenting and writing down my results.
- I thank the entire group R for the support and joy in countless occasions and, of course, to share the faith in nanoscience.
- I thank my parents and my siblings, who did not understand what I was doing, but who were always trusting that it will be good!

Symbols

A | **B** | **C** | **D** | **E** | **F** | **G** | **H** | **J** | **K** | **L** | **M** | **N** | **O** | **P** | **Q** | **R** | **S** | **T** | **V** | **W** | **X** | **Y**

A

$\langle ij \rangle_n$ all nth nearest neighbor pairs 22, 53

$\langle ... \rangle$ canonical average or time average 73

α the Gilbert damping 28

a the lattice constant 29

AMR anisotropic magnetoresistance 64

AR atomic rows 21

A the autocorrelation function 11

B

B a temperature dependent fit parameter; a local magnetic field 76, 84

BCC the body center cubic crystal lattice 23

β inverse temperature $1/k_{\mathrm{B}}T$ 7–10, 17

C

$\mathcal{C}$ a constant 28

C the specific heat 9

D

$\mathcal{D}$ a constant 28

Δ absolute difference of two values of the quantity Q: $\Delta Q = |Q_\mu - Q_\nu|$ 17

δ_{DW} the domain wall width 24

$\delta_{V_{\mathrm{DW}}}$ mean square deviation, hence, the variance of the domain wall velocity 66

$\mathrm{d}I/\mathrm{d}U$ $\mathrm{d}I/\mathrm{d}U$ signal of an STM 20

d the inter-atomic distance along x 31

E

$E_{\mathrm{P}}(x)$ the Peierls energy 31

ε a temperature dependent fit parameter 76

J

J an exchange constant 22

$J_{[001]}$ exchange constant along [001] 93

$J_{[1\bar{1}0]}$ exchange constant along $[1\bar{1}0]$ 88

$J_{[1\bar{1}1]}$ exchange constant along $[1\bar{1}1]$ 88

J_n exchange constant of the nth nearest neighbors 22, 53

J_{sd} the coupling constant between itinerant s electrons and localized d electrons 27

K

K_y the easy-axis anisotropy along y 22

K anisotropy constant of the defects 22

κ the decay constant 26

k_{B} the Boltzmann constant 28

K_0 the easy-axis anisotropy of non-defect sites 52

$K^{\mathrm{rim}}_{[1\bar{1}0]}$ the easy-axis anisotropy of rim atoms of Fe/W(110) 88

$K^{\mathrm{surf}}_{[1\bar{1}0]}$ the easy-axis anisotropy of surface atoms of Fe/W(110) 88

K_z the hard-axis anisotropy along z 22, 53

L

LLG Landau-Lifshitz-Gilbert equation 27

L number of particles of the system 8

λ just another state 16

L_0 a microscopic length scale of the order of one 81

l_{ex} the exchange length 41

λ_s the shift exponent $\lambda_s = 1/\nu$ 81

M

MCS a Monte Carlo step 11

MFM magnetic force microscope 4

MOKE magneto-optic Kerr effect 64

M the magnetization of the ensemble $M = \sum_i^L \sqrt{m_x^i + m_y^i + m_z^i}$ 10

r_c the critical distance between tip and domain wall at which the current induced by the STM tip causes a domain wall propagation 35

$\boldsymbol{r}_\mathrm{tip}$ position vector of the tip 25

r_tw the distance between the tip and the domain wall position 58, 59

r_v the virtual distance at which $\tilde{G}$ vanishes 78

r_y distance between two atomic rows along y 40

S

S_0 area of the domain wall 24

SP-STM spin-polarized scanning tunneling microscopy 25

STM scanning tunneling microscope 1, 20

$\boldsymbol{S}$ spin vector $\boldsymbol{S} = (S_x, S_y, S_z)$ 10

σ_sp conductivity of the tunnel junction 45

$S^i_{[1\bar{1}0]}$ $[1\bar{1}0]$ magnetization component of spin i 88

SC the simple cubic crystal lattice 23

$\boldsymbol{S}_\mathrm{D}$ magnetization vector of a domain 42

$\boldsymbol{S}_\mathrm{DW}$ magnetization vector of the domain wall 42

T

δ_{T_c} shift of the Curie temperature of a finite system 14

τ_{eq} autocorrelation time of a Monte Carlo simulation 11

θ angle between two vectors 26

$\boldsymbol{\mathcal{T}}$ the tunneling current 25

T the temperature 10

t the observation time 73

$\mathcal{T}_0$ the spin-polarized current averaged over the surface unit cell 26

T_1 $T_1 = T_\mathrm{b}$ 76

T_2 $T_2 = T_\mathrm{c}(L)$ 76

T_3 $T_3 = T_\mathrm{c}(\infty)$ 76

τ the escape time 57

τ_0 a pre-factor 57

$\bar{\tau}$ the mean lifetime 89

T_b the blocking temperature 73

T_c the Curie temperature 10, 69

T^c a characteristic temperature 99

T_c^MF the mean-field Curie temperature 83

V

ν a certain state of the system; a critical exponent; the switching rate 10

$V_\mathrm{P}(x)$ the Peierls potential 31

V_tip velocity of the tip ($V_\mathrm{tip} = 1.5 \times 10^{-5}$) 29

ν_0 the Arrhenius pre-factor 89

ν_c a characteristic frequency 99

V_DW the domain wall velocity 33, 65

W

w_μ occupation probability of state μ 14

X

χ the magnetic susceptibility 10

x_0 the domain wall position 29

ξ the correlation length 10

Δx_tip a tip-step, hence, the displacement of the tip into x direction 29

x_tip x component of the tip position 35

Y

y a temperature dependent fit parameter 76